FROM THE INSTITUTE FOR SIGNAL PROCESSING
OF THE UNIVERSITY OF LÜBECK
DIRECTOR: PROF. DR. ALFRED MERTINS

Robust Breath-held Abdominal Magnetic Resonance Imaging based on Compressed Sensing

DISSERTATION

for Fulfillment of
Requirements
for the Doctoral Degree
of the University of Lübeck

from the Department of Computer Sciences

Submitted by

Nadine Gdaniec
from Hamburg

Lübeck 2014

First referee: Prof. Dr.-Ing. Alfred Mertins

Second referee: Prof. Dr. rer. nat. Thorsten M. Buzug

Date of oral examination: July 9th, 2014

Approved for printing. Lübeck, July 10th, 2014

Abstract

Respiratory motion is a common source of artifacts in abdominal magnetic resonance imaging because of long scan durations. These are induced by the large covered imaging volume and the high spatial resolution required for diagnosis. The achievable breath-hold duration of a particular patient is difficult to predict and varies over multiple breath-holds. This is especially relevant in dynamic contrast-enhanced examinations because multiple breath-holds with short time to recovery need to be performed. This variation in breath-hold duration renders scan adaptation before the scan challenging.

Compressed sensing is used in this thesis to address the issue of unpredictable breath-hold durations with an optimal usage of the data. First, a fast implementation for general compressed sensing sampling patterns is proposed with fixed scan durations. This implementation enables generation of sampling patterns directly and automatically on the scanner after scan planning. Theoretical background is presented for optimizing the sampling density for a given application and the required reduction factor.

This thesis aims to imaging of the abdomen that is more robust against premature onset of breathing by using compressed sensing for flexible scan termination at breathing onset. The spatial resolution is increased with time to achieve a continuous compromise between spatial resolution and signal-to-noise ratio. Independent of the achieved breath-hold duration, the sampling patterns enable reconstruction from consistent data that were acquired during the breath-hold. Feasibility is shown for 3D dual-gradient-echo sequences for water/fat imaging without contrast agent and for dynamic contrast-enhanced imaging. Furthermore, the combination with a fast sequence-switching approach is shown that enables dual-contrast imaging within a single breath-hold to obtain spatial and temporal correspondence of the images. As an alternative application, the adaptive samling patterns are used for the assessment of the liver fat fraction. This application requires high accuracy due low relative fat content of the liver even for fatty liver disease.

In dynamic contrast-enhanced imaging of the liver a series of 3D data with the same experimental parameters is acquired before and after contrast injection. The data exhibit similarity that is exploited in this thesis to improve image quality with a joint reconstruction of the temporal phases.

The robust sampling approach ensures imaging without motion artifacts in case of premature breathing onset in abdominal examinations. By preventing repeated scanning, the proposed method improves patient comfort, image quality, and the work-flow.

Zusammenfassung

Atembewegungen sind eine häufig auftretende Ursache für Artefakte in abdominaler Magnetresonanztomographie aufgrund langer Aufnahmezeiten. Diese werden durch das große Bildgebungsvolumen und die hohe Auflösung, die für die Diagnostik benötigt werden, verursacht. Die Dauer für die ein Patient die Luft anhalten kann ist schwer vorauszusagen und variiert zudem bei mehrfachem Atemanhalten. Besonders bei kontrastmittelverstärkter Bildgebung ist dies relevant, weil mehrfach der Atem angehalten werden muss und dabei kaum Zeit zum Erholen bleibt. Diese Variation der Luftanhaltedauer macht die Anpassung einer Aufnahme vor der Ausführung zu einer Herausforderung.

Um das Problem unvorhersagbarer Dauer des Atmeanhaltens zu adressieren, wird in dieser Arbeit die komprimierte Abtastung verwendet um die Daten optimal zu nutzen. Als erstes wird die schnelle Implementierung eines allgemeinen Abtastmusters mit fester Aufnahmedauer für die komprimierte Abtastung vorgestellt. Diese Implentierung erlaubt die automatische Erzeugung des Abtastmusters direkt auf dem Tomographen. Es wird theoretisches Hintergrundwissen für die Optimierung der Abtastdichte für eine gegebene Applikation bei gegebenem Unterabtastungsfaktor präsentiert.

Das Ziel dieser Arbeit ist es mit Hilfe von komprimierter Abtastung die abdominale Bildgebung robuster gegenüber vorzeitig einsetzendem Atem zu machen, indem die Aufnahme beim Einsetzen von Atmung abgebrochen wird. Die örtliche Auflösung wird mit der Zeit vergrößert, um einen kontinuierlichen Kompromiss zwischen der örtlichen Auflösung und des Signal-zu-Rausch-Verhältnisses zu erreichen. Unabhängig von der erreichten Dauer des Atemanhaltens ermöglichen diese Abtastmuster die Rekonstruktion von konsistenten Daten, die bei angehaltenem Atem aufegnommen wurden. Die Machbarkeit dieser Methode wird anhand von 3D dual-Gradientenecho-sequenzen für Wasser/Fett Bildgebung ohne Kontrastmittel und anhand von dynamimschen kontrastmittelverstärkten Anwendungen gezeigt. Desweiteren wird die Kombination mit einem schnellen Sequenzwechsel gezeigt, wodurch eine Aufnahme zweier Kontraste während eines Atemanhalte Vorgangs ermöglicht wird, die örtliche und zeitliche Korrespondenz aufweisen. Als weitere Anwendung werden die adaptiven Abtastmuster für die Bestimmung des Leberfettgehalts verwendet. Diese Anwendung benötigt hohe Genauigkeit auf Grund des niedrigen relativen Fettgehaltes der Leber, auch bei krankhafter Fettleber.

In dynamischer kontrastmittelverstärkter 3D Bildgebung der Leber werden Daten mit konstanten experimentellen Parametern vor und nach Kontrastmittelinjektion aufgenommen. Die Daten weisen eine große Ähnlichkeit auf, die in dieser Arbeit ausgenutzt wird

um mittels einer gemeinsamen Rekonstruktion der temporären Phasen die Bildqualität zu verbessern.
Die robuste Abtastmethode stellt Bildgebung ohne Bewegungsartefakte bei vorzeitig einsetzendem Atem in abdominalen Untersuchungen sicher. Durch das Verhindern erneuter Aufnahmen wird der Komfort für den Patienten, die Bildqualität und der Arbeitsablaufes verbessert.

Acknowledgements

I would like to express my gratitude to Prof. Dr. Alfred Mertins for accepting me as Ph.D. student and for supervising this dissertation.
I am indebted to Prof. Dr. Peter Börnert and Dr. Holger Eggers for answering my questions with patience, numerous discussions, proof-reading, spending hours at the scanner to find the source of artifacts, and for the co-examination of this work. The same holds for Dr. Mariya Doneva, thank you also for nice coffee-breaks.
I would like to thank Dr. Dye Jensen for giving me the opportunity to write the Ph.D. thesis as part of the Tomographic Imaging group in Hamburg. From this group, I thank all colleagues for creating a friendly working atmosphere and for spontaneous assistance. I am especially grateful to Peter Koken for repeated assistance with the PPE and the repository, Dr. Tim Nielsen for useful ideas in debugging, Dr. Christian Stehning for helping in different situations, and Dr. Michael Helle for shopping trips and coffee-breaks. Thanks also to the volunteers for holding the breath several times.
The past three years would also not have been the same without the other students, especially Dr. Hanno Homann for sharing the office with me for a year, Hannes Wendland, Christian Haase, Dominik Kutra, and Ingrun Schönberg.
Thanks to Dr. Andrea Wiethoff I spent some time at the UTSW Dallas. I want to express my gratitude to you for housing me during the stay, introducing me to several people, spending time at the scanner, and also spending free time, for example, at the swimming pool with me. I would like to thank Dr. Ivan Pedrosa for giving me the opportunity to acquire clinical data at the UTSW, and also Dr. Qing Yuan for her cheerfulness and assistance at the scanner.
Last, but not least, I would like to thank my friends for support in different situations, especially Christiane Ripperda, and for nice evenings also Sebastian Ripperda, Kai and Stephanie Wellner. I am grateful to Lena and Katharina Dittrich for looking after Flashi during my visits of various conferences, and Nadine Heidrich and Kristin Goebel for relaxed evenings with delicious food. My family, particularly my parents Albert and Renate Weißfahl, supported me the whole time, thank you for that. I want to express my gratitude to my husband, Przemyslaw, for being there for me, for example, with a last-minute photo-shooting.

Contents

Abbreviations

1D	One-dimensional
2D	Two-dimensional
3D	Three-dimensional
ACS	Auto-Calibration Signal
CS	Compressed Sensing
DCE	Dynamic Contrast Enhanced
FFE	Fast Field Echo
FFT	Fast Fourier Transform
FOV	Field of View
MRI	Magnetic Resonance Imaging
NAFLD	Non-alcoholic fatty liver disease
NMR	Nuclear Magnetic Resonance
PI	Parallel Imaging
pmf	Probability mass function
PSF	Point Spread Function
RF	Radio Frequency
RMSE	Root Mean Squared Error
sdf	Sampling density function
SNR	Signal to Noise Ratio
SVD	Singular Value Decomposition
TE	Echo Time
TFE	Turbo Field Echo
TR	Repetition Time

Chapter 1

Introduction

Magnetic resonance imaging (MRI) is a non-invasive imaging technique that provides images from inside the human body without ionizing radiation. The signal that is used in MRI originates from the imaged subject. MRI supports a huge variety of contrast mechanisms and a better soft-tissue contrast than imaging modalities based on ionizing radiation, like computed tomography. This is the primary motivation to use MRI for different applications. However, MRI suffers from problems in some applications mainly due to long scan times. The long scan times are not only uncomfortable for the patient, but also increase the risk of artifacts in the images in case of motion. The artifacts can range from slightly visible to very severe, depending on the motion pattern and the sensitivity of the experiment to motion. Motion can be involuntary motion of e.g. the hands, knees, or the head, or vital motion, like respiration, pulsation of the blood flow, peristaltic, or heart beating. While the first kind of motion can be controlled to some extent, this becomes much more complicated for the second source of motion. For increased patient comfort, reduced motion artifacts, and better workflow, techniques were investigated in the past to accelerate the MRI acquisition substantially. These improvements rely on advances in hardware, in pulse sequence design, and in algorithms, to reconstruct from less data. Parallel imaging or methods based on data redundancy are nice examples of that. The progress in these areas enabled new clinical possibilities, like 3D imaging of, for example, the abdomen, which otherwise would be inconceivable. MRI is frequently used for imaging of the brain providing high resolution images, because motion can be restricted successfully. Despite the progress that has been made in the last decades, imaging of the abdomen is still a challenging task with frequently occurring respiratory motion artifacts hampering reliable clinical diagnosis.

In this thesis, a method to obtain diagnostic images of the abdomen with significantly reduced motion artifacts is presented that uses compressed sensing. To ease the understanding of the thesis, the background of MRI and on compressed sensing (CS) is introduced in Chapter 2. Typically, acquiring less data is expected from CS, a rapidly emerging research area, based on the idea that natural images, and most of MR images, are compressible. This knowledge can be exploited during data acquisition to decrease the amount of acquired data. While excellent theoretical work has been performed on this topic in the past, the application of CS to MRI still requires research to pave the way towards its clinical use. The application of CS affects the acquisition as well as the reconstruction process that both need to be optimized to obtain high quality images. During acquisition the sampling has to lead to incoherent aliasing in the sparsity domain to be able to reconstruct images without artifacts. The fast generation of such a sampling pattern with a fixed number of samples and a given variable density is described in Chapter 3 enabling generation directly on the scanner. For an efficient calculation of the intended sampling patterns, the location-dependent sampling density is crucial. While the sampling density for a fixed reduction factor and uniform sampling is obvious, this is not so for variable density sampling. The estimation of the sampling density function dependent on the reduction factor without time-consuming simulation is included in Chapter 3 as well.

While the basic feasibility of CS has already been shown for various applications in the past, the technique is not used in clinical practice yet. The reduced image acquisition time is paid for by higher computational cost of the reconstruction, and thus, it is not useful for all applications. This thesis aims at using CS to achieve more robust imaging to ensure diagnostic images. In Chapter 4, a sampling pattern is proposed that automatically increases the spatial resolution during the scan combined with flexible scan termination. This concept can be applied to breath-held abdominal imaging to exploit the total breath-hold duration or handle premature breathing onset in patients and immediately terminating the acquisition at the onset of breathing. The scan automatically adapts to the breath-hold duration a particular patient is able to achieve and reconstructs an image from the acquired data without motion artifacts. The sampling pattern performs a compromise between spatial resolution and signal-to-noise ratio for every breath-hold duration. The breathing onset can be detected with navigators. Two different navigators are used in this thesis in more detail. Due to the scan termination, and due to the proposed sampling pattern, only consistent data that satisfy CS

constraints are used for reconstruction, and images with reduced respiratory motion artifacts are obtained. This method is introduced and evaluated on a variety of abdominal imaging procedures on volunteers and patients with and without contrast agents, also presented in Chapter 4. The application of the motion-robust adaptive sampling pattern to dynamic contrast-enhanced imaging is especially relevant because of the time constraints of the imaging series. The patients have hardly any time to recover between subsequent scans, and achieving the same breath-hold duration becomes difficult. The adaptive sampling pattern is furthermore combined with dual-contrast imaging within one breath-hold by using a fast sequence-switching approach. This enables perfect spatial correspondence of the data, because they are acquired in the same breath-hold.

One particularly challenging application of the proposed sampling scheme is the determination of the fat fraction of the liver and is presented separately in Chapter 5. The estimation of the fat-fraction of the liver is a promising biomarker for fatty liver disease. MRI is a non-invasive alternative for biopsy in this application. The fat fraction of the liver is less than ten percent of the total tissue and thus requires exact and reliable quantitatively estimated values. Motion artifacts need to be prevented, because they sophisticate the quantitative values. Due to various issues, among others induced by the prospective undersampling, the acquisition is modified. It is combined with the adaptive sampling pattern and the sequence switching approach that enables switching between scans with hardly any delay, and thus, enables fat-fraction maps without motion artifacts.

In Chapter 6, a joint reconstruction of multiple temporal phases from a dynamic contrast-enhanced examination is presented. The images from different temporal phases of the same patient contain redundant information that can be exploited with this reconstruction. The redundancy is related to the fixed geometry of the imaged object, apart from motion due to distinct breath-holds, but also to the knowledge that the contrast agent does not induce changes in the fat signal. A weighting of the distinct temporal phases is proposed in order to be able to influence their mutual impact.

The conclusion in Chapter 7 gives an outlook of possible future research activities.

Chapter 2

Background on Magnetic Resonance Imaging

The following chapter about the background of magnetic resonance imaging (MRI) is supposed to ensure a better understanding of the thesis, but raises no claim of completeness. For a complete introduction to the field of MRI, see existing literature [1, 2].

2.1 Signal generation

Magnetic resonance imaging (MRI) is a noninvasive medical imaging technique that is based on nuclear magnetic resonance (NMR) effects. A signal is therefore only expected for NMR active nuclei. The most frequently used nucleus is hydrogen, consisting of one proton with a spin quantum number of $\frac{1}{2}$ that results in two degenerate energy states, called spin up and down with a small magnetic moment. However, the human body contains a large number of nuclei and can be described by a net magnetization M, the volume average over the magnetic moments. In a field-free environment, the spins of the nuclei are randomly distributed and thus result in a vanishing net magnetization M. An external homogeneous magnetic field that abrogates the degeneration of the energy states is applied, and thus, results in unequal occupancy of the energy states. The energy states can be described in a classical model with a magnetic moment precessing at Larmor frequency

$$\omega = \gamma B_0 \tag{2.1}$$

around the external magnetic field. The gyromagnetic constant γ is specific to the type of examined nuclei. The resulting equilibrium net magnetization M that results from the occupancy difference depends on the temperature and the applied field strength. A transition between these discrete quantum energy states can be achieved by the application of a radio frequency (RF) pulse of adequate frequency/energy that moves the net magnetization away from its thermal equilibrium value. Those RF pulses are termed excitation pulses. After turning off the RF pulse, the system relaxes to the thermal equilibrium state and is thus emitting radiation, called free induction decay. The excitation as well as the relaxation process can be described by the Bloch equations.

If a receive coil is properly placed next to the object, the emitted radiation changes the magnetic flux through the coil. A change in magnetic flux results in an induced current in the receive coil generating an MR signal. The MR steady state signal f from each small volume element, called voxel, depends on the proton density as well as on the relaxation time T_1 of the tissue and the repetition time TR of subsequent excitations

$$f \propto \rho(x, y, z)(1 - e^{-\frac{\mathrm{TR}}{T_1}}). \tag{2.2}$$

A further fundamental element of MR imaging is the use of magnetic field gradients G. They represent linearly changing magnetic field components that can be applied to the main magnetic field B_0 in the three directions (x, y, z) with appropriate waveforms as a function of time. A signal is created from the set of protons in a voxel if the protons precess in phase. Due to different reasons, if a gradient is switched on, the local magnetic moments dephase with time. An adequate choice of the magnetic field gradients G or additional RF pulses can be used to rephase the protons and thus regenerate signal, called echoes.

The relaxation times of distinct tissue types in the body are different and thus generate contrast in the image [1, 2]. By variation of the excitation pulse, dephasing, rephasing mechanisms, or the timing, various MR signal levels can be generated for different tissue types that have varying magnetization properties and thus induce contrast in MR images. This high flexibility in generating contrast in the images is one of the assets of MR imaging.

2.2 Spatial encoding

The described signal is the superposition of the emitted radiation from the entire excited volume. In traditional MRI, the spatial encoding of the signal is performed by applying a magnetic field gradient to the object [3]. This choice of encoding is referred to as Fourier encoding of the imaging object that ensures fast reconstruction by using an FFT in Cartesian imaging and is described in Section 2.2.2 and Section 2.2.3. Furthermore, it enables imaging of details that are far smaller than the wavelength of the applied excitation radiation. Basically, these techniques render the Larmor frequency or phase of the magnetic moments location dependent.

Three different gradient-encoding techniques are frequently used, namely slice selection, phase encoding, and frequency encoding that differ by the timing of the applied magnetic field gradients G, see Figure 2.1. The magnetic field gradients can be applied during signal excitation, signal evolution, or signal sampling, having different impact on the acquired signal. The encoding methods are described in more detail in the following sections.

In the last decades, the spatial sensitivity of a plurality of receive coils was found to allow an alternative way of spatial signal encoding [4, 5], because coils placed at different locations receive signal from the same source differently well. Fourier encoding and multiple receive coils can be combined to speed up the image acquisition. Various methods exist that are summed up as parallel imaging techniques and their underlying principle is described in Section 2.2.4.

2.2.1 Encoding during signal excitation: Slice selection

One encoding method is slice selection. For slice selection, a magnetic field gradient $G_z(t)$ in 1D is applied during RF excitation resulting in a spatially linearly changing magnetic field. The Larmor frequency depends on the magnetic field strength, see (2.1) and is thus spatially linearly changing as well. Due to the spatially dependent resonance frequency, the applied RF pulse with finite bandwidth is only resonant in a spatially restricted region. Only the corresponding protons in this region, therefore, are influenced by the excitation pulse and contribute to the detectable MR signal.

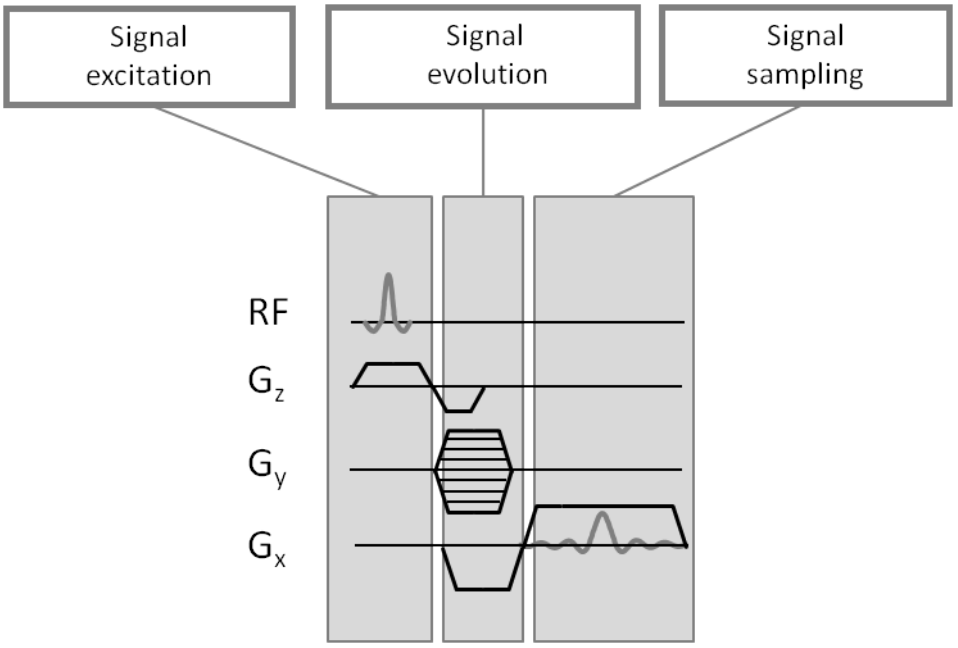

Figure 2.1: Temporal scheme of encoding methods. The imaging process can be divided into three sections: signal excitation, signal evolution, and signal sampling. Slice selection is performed during excitation indicated by the gradient G_z in the figure. Signal evolution is used to incorporate phase encoding with the gradient of varying strength per profile G_y. Frequency encoding is performed in the last stage, during signal sampling by applying the gradient G_x.

2.2.2 Encoding during signal sampling: Frequency encoding

A very time efficient encoding technique is frequency encoding that is performed directly during signal sampling. To understand the underlying principle, a further description of the MR signal in a selected slice is required.

In a homogeneous magnetic field the protons with density $\rho(x, y, z)$ emit radiation at the Larmor frequency ω_0. The proton density $\rho(x, y, z)$ is assumed to be constant in time here. In general, it can be temporally varying due to any kind of motion (e.g. cardiac motion, blood flow, respiratory motion, contrast agents). The signal $f(t)$ induced in a receive loop by the radiation can be described as a temporally changing superposition of radiation from all locations of the excited volume V

$$f(t) = \int_V \rho(x, y, z) e^{-i\omega_0 t} \, \mathrm{d}x \, \mathrm{d}y \, \mathrm{d}z. \tag{2.3}$$

The signal phase for this case can be defined as

$$\phi(t) = \omega_0 t. \tag{2.4}$$

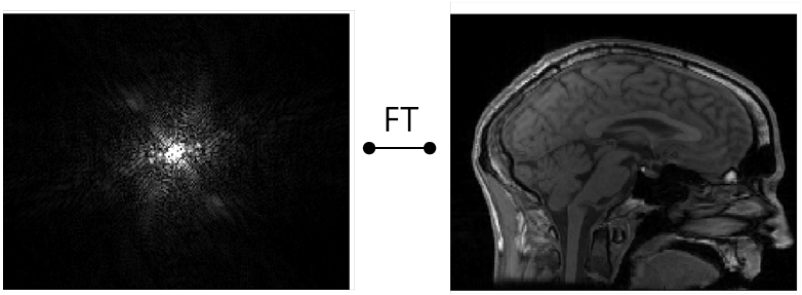

Figure 2.2: Connection of measurement space and image space. The acquisition of data is normally performed in k-space, shown in the left part of the figure with corresponding data. The image is obtained by a Fourier transform and is shown here in the right part of the figure.

An additional magnetic field gradient $G_x(t)$, applied during read-out leads to a spatially dependent phase

$$\phi(x,t) = \omega_0 t + x \int_0^t \gamma G_x(\tau)\,\mathrm{d}\tau = \omega_0 t + x k_x(t), \tag{2.5}$$

that can be inserted in (2.3) and gives

$$f(t) = \int_V \rho(x,y,z) e^{-ik_x(t)x}\,\mathrm{d}x\,\mathrm{d}y\,\mathrm{d}z, \tag{2.6}$$

if the signal is demodulated at Larmor frequency $\omega_0 t$. In the latter two equations, the variable

$$k_x(t) = \gamma \int_0^t G_x(\tau)\,\mathrm{d}\tau \tag{2.7}$$

is used. It is defined as the coordinate in the measurement space [6, 7] that is called k-space. If the gradient is a constant $G_x(t) = G_x$, then $k_x = \gamma G_x t$. This means that the resonance frequency is changing linearly with the spatial position, which allows directly mapping them onto each other. This procedure is called frequency encoding and can be used to encode one spatial direction. For the remaining directions, other encoding methods need to be used to obtain 2D or 3D images.

2.2.3 Encoding between signal excitation and signal sampling: Phase encoding

A far more time-consuming encoding technique compared with frequency encoding is phase encoding that can be used to encode the remaining spatial directions. An additional magnetic field gradient, called phase encoding gradient G_y, is applied during signal evolution, i.e. between RF excitation and sampling. The strength of the magnetic field is increasing in the phase encoding direction and leads to differing resonance frequency along this direction and hence differing rate of precession of the spins. After the application of this gradient for a fixed time T, and turning off the gradient afterwards, the spins along this direction precess at the same rate again, but their phase differs

$$\phi(y,t) = \omega_0 t + y\gamma G_y T = \omega_0 t + y k_y. \tag{2.8}$$

Because only one k_y can be encoded for one read-out, several repetitions have to be performed that differ in the strength of the magnetic field gradient G_y. These repetitions are the reason for the long scan times in MRI. This encoding technique is explained here for one direction, but can be applied in both remaining directions (k_y,k_z) for 3D imaging. The signal modulation can be formulated similar to (2.6) as

$$f(t) = \int_V \rho(x,y,z) e^{-i(k_x(t)x + k_y(t)y + k_z(t)z)} \,\mathrm{d}x\,\mathrm{d}y\,\mathrm{d}z. \tag{2.9}$$

This equation contains the k-space coordinates $k_x(t)$, $k_y(t)$, and $k_z(t)$. The spin density and the k-space signal are related by a Fourier transform, see Figure 2.2. If the sampling is performed on a uniform Cartesian grid in k-space, the transformation can be performed efficiently with an inverse fast Fourier transform (iFFT). Due to the discrete sampling in the measurement space (k-space), periodicity of the object in image space is enforced. The periodicity constant is related to the distance of neighboring profiles in k-space Δk by the Shannon-Nyquist sampling theorem:

$$r_{\text{max}} \propto \frac{1}{\Delta k} \tag{2.10}$$

with r representing any of the three spatial directions. The value r_{max} sets the size of the imaged area, called field of view (FOV). This is illustrated in Figure 2.3 for an appropriate choice of Δk for the size of the object in image (a). For illustrative purposes, every second k-space profile was removed resulting in doubled Δk, shown in

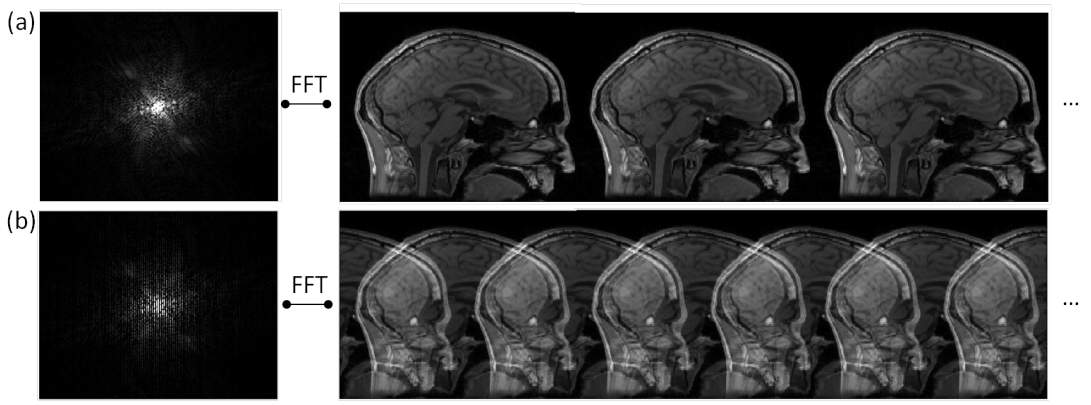

Figure 2.3: Implication of discrete sampling. Sampling in k-space is frequently performed on a uniform Cartesian grid to be able to perform reconstruction via FFT that has low computational cost. The discrete sampling assumes periodicity of the object in image space and thus requires an appropriate choice of the distance of neighboring k-space profiles, shown in the upper part of the image. The lower part shows the consequences of a Δk chosen too high, the images overlap.

Figure 2.3(b). This distance of neighboring k-space profiles is oversized for the object, and the images are overlapping due to undersampling. The corresponding effect in image space is called aliasing. Furthermore, the finite number of samples is the cause of the finite resolution of the image. The maximum extent of profiles in k-space sets the spatial resolution of the image:

$$\Delta r \propto \frac{1}{2k_{\text{max}}}. \tag{2.11}$$

2.2.4 Accelerate the acquisition: Parallel imaging

Fourier encoding has one disadvantage, it is time-consuming because the individual k-space profiles have to be acquired sequentially. A completely different idea for spatial encoding is based on the fact that the spatial receiver sensitivity strongly depends on the location of the receiver. The signal from every individual voxel a_{il} for a coil l is thus the weighted spin density ρ_i with the corresponding sensitivity s_{il} at location i

$$a_{il} = s_{il}\rho_i. \tag{2.12}$$

Using a receiver array instead of a single receiver thus enables acquisition of multiple profiles of the same object with the same encoding, but with distinct sensitivities in parallel. A rather extreme variant of pure sensitivity encoding is proposed in [4], where an encoding without magnetic field gradients, but with a large number of receivers, is proposed.

Later, a method was proposed [5, 8, 9, 10, 11] that keeps Fourier encoding, but reduces the number of phase encoding steps by using multiple receivers. This concept is frequently used today and is called parallel imaging (PI). Because of the difference in spatial sensitivity of the coils of the array, the combination of both types of encoding can reduce the scan time. This becomes obvious for an unrealistic, but intuitive example with an array consisting of two coils with each coil receiving signal from disjoint halves of the object. Due to the halved FOV of each coil, the distance in k-space can be doubled, which results in only half the scan time. The images from both coils can be combined to one image. This is described in more detail for realistic sensitivity profiles and for more than two coils in [12]. The required parallel imaging reconstruction procedures can be divided into two types. One type, in which image reconstruction is performed in image space and the other, in which image reconstruction is performed in k-space.

2.2.4.1 SENSE: SENSitivity Encoding

SENSE is an example of an image-space based method and is presented in [8] together with two different reconstruction methods using linear algebra and an SNR analysis for multiple receivers. It combines sensitivity with phase encoding and is, in principle, applicable to any kind of sampling pattern in k-space.

If the number of phase encoding steps is reduced while maintaining the resolution, uniform k-space sampling is performed at a lower rate than the Nyquist sampling rate. This results in aliasing in image space, because the FOV is reduced, while the object size remains the same. Within this reduced FOV, each pixel is a superposition of pixel values from different locations out of the larger FOV, as is illustrated in Figure 2.3. This can also be understood in terms of the point spread function (PSF). The PSF is the response of an imaging system to a point-wise input. It is calculated by choosing a single pixel in image space to have an assigned value of one, while the rest is zero. Applying an FFT to this input, followed by the application of the sampling pattern, and subsequently followed by an iFFT gives the PSF. For regular sub-sampling by a factor of two, this results in two pixels with values unequal to zero separated by half the FOV. This repetition of the pixel is induced by the discrete sampling in k-space and is called aliasing.

In a SENSE reconstruction, for each element of the array, an aliased image is reconstructed in the first step. In a second step, unfolding of the coil images is performed.

The number of aliased pixels and their location is determined by the degree of undersampling, described by the PSF. Because of the spatial sensitivity of the coil array, the weighting of the aliased pixels for the superposition is different for every coil element of the array and denoted by the matrix S.

For convenience, the pixel-wise unfolding process is described here for a reduction factor of two with two coils. The aliased pixel value at location i from coil u is denoted by a_{iu}, the sensitivity by s_{iu} and the unfolded pixel by ρ_i. The pixel-values for the overlapping pixels are a superposition of multiple pixels, in this case two

$$a_{i1} = s_{i1}\rho_i + s_{j1}\rho_j \tag{2.13a}$$

$$a_{i2} = s_{i2}\rho_i + s_{j2}\rho_j. \tag{2.13b}$$

The coil sensitivities need to be known to be able to solve this system of equations. It becomes clear from this system of equations that the number of folded pixels for every location must not exceed the number of coils and that it can only be solved if the coil sensitivities are linearly independent of each other. If the independence is not given, then the reduction factor needs to be reduced or additional coils need to be introduced. (2.13a) and (2.13b) can be written in matrix form as

$$\boldsymbol{a} = \boldsymbol{S}\boldsymbol{\rho}. \tag{2.14}$$

Multiplying (2.14) with S^H from the left yields

$$\boldsymbol{S}^H\boldsymbol{a} = \boldsymbol{S}^H\boldsymbol{S}\boldsymbol{\rho}. \tag{2.15}$$

The product S^HS is square, enabling inversion

$$\boldsymbol{\rho} = (\boldsymbol{S}^H\boldsymbol{S})^{-1}\boldsymbol{S}^H\boldsymbol{a} = \boldsymbol{U}\boldsymbol{a}. \tag{2.16}$$

The product $(\boldsymbol{S}^H\boldsymbol{S})^{-1}\boldsymbol{S}^H$ is the Moore-Penrose pseudo-inverse, which yields the least squares estimator to (2.14). If the noise level and correlation between coils from the coil array, described by the noise covariance matrix $\boldsymbol{\Phi}$ in [8, 13], are taken into account, the unfolding matrix becomes slighty more complicated:

$$\boldsymbol{U} = (\boldsymbol{S}^H\boldsymbol{\Phi}^{-1}\boldsymbol{S})^{-1}\boldsymbol{S}^H\boldsymbol{\Phi}^{-1}. \tag{2.17}$$

This is the best linear unbiased estimator (BLUE) to the solution of (2.14). Hence, the unfolded pixel values $\boldsymbol{\rho}$ from the full FOV are calculated according to

$$\boldsymbol{\rho} = \boldsymbol{U}\boldsymbol{a} \tag{2.18}$$

from the aliased images $\boldsymbol{a}$. The system of equations is fully determined if the number of channels N equals the sub-sampling factor R and the coils are independent. Due to imperfections in the acquisition, like noise, and redundant information of the array elements, the sub-sampling factor needs to be chosen smaller than the number of channels. This overdetermined system of equations can be solved by calculating the Moore-Penrose pseudoinverse [14], done in (2.16).

2.2.4.2 GRAPPA: Generalized Autocalibrated Partially Parallel Acquisitions

Instead of performing the unfolding in image space, the unfolding can be performed in k-space instead. The most frequently used algorithm of this kind of reconstruction methods is called GRAPPA [9], which is described in the following.

In image space, the signal from the coil element m for each voxel a_{im} can be estimated from the signal a_{il} of the coil element l at the same spatial position i

$$a_{im} = a_{il}\frac{s_{im}}{s_{il}} \tag{2.19}$$

with the help of the coil sensitivity maps. Noise is ignored in this illustrative consideration. This multiplication in image space corresponds to a convolution in k-space with a convolution kernel of restricted size due to the smooth variation of the coil sensitivity maps. This is the underlying assumption for the basic idea of GRAPPA [9]. Unacquired profiles of a single coil can be estimated from a weighted sum of neighboring profiles, indicated by the weighting factors $n(j, b, l, m)$ (taken together in a block with the unacquired profiles), from the same coil and the other coils by a block-wise reconstruction

$$f_j(k_y - m\Delta k_y) = \sum_{l=1}^{L}\sum_{b=0}^{N_b-1} n(j, b, l, m) f_l(k_y - bR\Delta k_y). \tag{2.20}$$

In this equation, $f_j(k_y - m\Delta k_y)$ is the k-space signal at the position $k_y - m\Delta k_y$, N_b is the number of blocks, R is the reduction factor, l counts through coils, while b counts

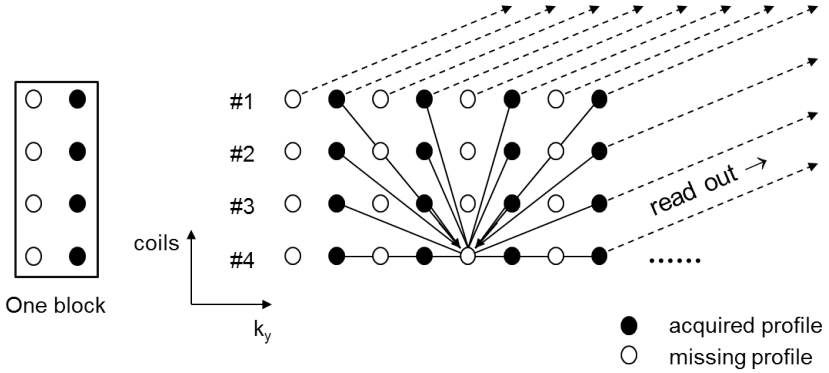

Figure 2.4: Illustration of a block for a reduction factor of two in one direction. Every row is the data from one coil, while every column is the data for a fixed location in k-space k_y. Every second profile is acquired, indicated by a black filled circle. Every other profile is not acquired indicated by an empty circle and an additional ACS line that is used to learn the weightings n from neighboring blocks. A block is the affiliation of an acquired column of profiles with a column of unacquired profiles. The weightings are used to calculate the values of unacquired profiles from acquired profiles.

through reconstruction blocks. Figure 2.4 illustrates the sampling pattern for a reduction factor of two and the definition of a block in this approach. Each circle corresponds to one read-out profile. Every second profile is acquired (black filled circles), while every other is left unacquired (unfilled circles). The arrows indicate estimation of an unacquired profile from acquired profiles of neighboring blocks by convolution with a convolution kernel. The convolution kernel, respectively the weighting factors $n(j, b, l, m)$, are learned from the additional autocalibration signal (ACS) profiles (grey filled circles in Figure 2.5). The ACS is a fully sampled region typically placed at the center of k-space due to the better SNR compared with the periphery. The ACS can be included in the actual reconstruction to improve image quality. One block is the affiliation of data from all coils at a specific location in k-space k_y and the neighboring unacquired k-space profiles from all coils. The reconstruction procedure described in (2.20) is repeated for every single element of the coil array and results in unaliased single coil images that are combined in a further step.

The number of contributing blocks to one unacquired profile has an influence on the quality of the reconstructed image. It is stated in [9] that inclusion of all acquired blocks in the reconstruction leads to an exact reconstruction, but only profiles close to the missing profile contribute significantly. The restriction to neighboring profiles in k-space results in a more stable reconstruction for noisy data and is computationally clearly more efficient.

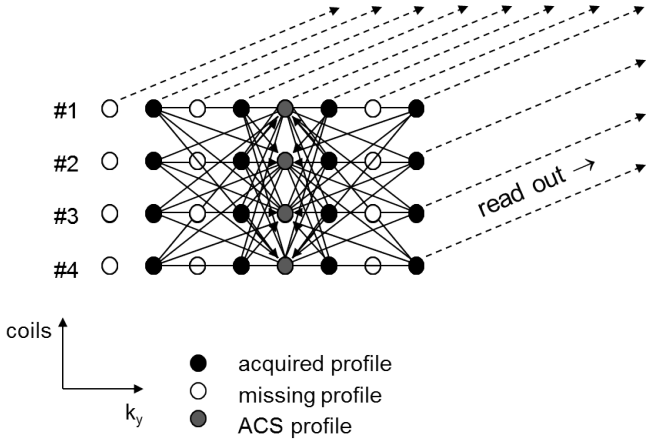

Figure 2.5: Illustration of ACS profiles. The weightings of neighboring profiles that contribute to the calculation of an estimation of an unacquired profile are calculated with the help of additionally acquired ACS profiles (gray). These weighting factors form the convolution kernel that is used to fill k-space by calculating unacquired profiles. The number of contributing blocks for each profile is restricted due to the smooth variation of the coil sensitivity maps.

2.2.4.3 Coil sensitivity maps calibration

For both parallel imaging techniques, knowledge of the coil sensitivities is crucial. For SENSE, they are explicitly needed in image space, while their representation in k-space is required for GRAPPA. In principal, there are two possibilities to obtain the coil sensitivity maps, either during the actual scan by acquiring a fully sampled central k-space region, called autocalibration area, or during a separate low resolution scan, called reference scan.

Additionally acquired central k-space profiles can be used directly to calculate weightings for neighboring k-space profiles as described in Section 2.2.4.2 or can be Fourier transformed and smoothened to be used as coil sensitivity maps in image based reconstruction. The autocalibration method has temporal correspondence to the actual scan that can be advantageous in case of motion or dynamic imaging. However, it lengthens the scan time of the actual scan and is acquired during every scan to exploit the advantage described before.

The additional reference scan can be used for image-based, as well as k-space-based parallel-imaging reconstruction techniques. It is only acquired once, or if significant changes have occurred. This shortens the actual scan duration, but is prone to misalignment due to motion.

2.2.4.4 Coil compression

With an increasing number of coil elements, the amount of data increases as does the reconstruction time. This is especially relevant for 3D imaging or dynamic studies. A way to handle this problem is coil compression [15, 16, 17], which reduces the number of physical coils to a smaller number of virtual coils by linearly combining the data from the physical coils. This becomes possible due to the redundant information of the physical coils that is reduced in the virtual coils.

The first compression techniques were hardware implementations [17, 18] that used the noise covariance between channel elements. These lead to compression with loss of information, because the sensitivity profiles are not used. Several software implementations of coil compression were proposed [15, 16, 19, 20, 21] for 2D Cartesian data and applied to 3D by using the same compression for each 2D slice out of the 3D data.

The extension of the compression to 3D imaging was made spatially dependent in [22], by using a different compression for each slice out of the 3D data. This coil compression technique was implemented and used in this work and is, therefore, further described in the following.

The direction of frequency encoding points along the x direction and is fully sampled. The 2D slices are perpendicular to this axis and are obtained by a 1D Fourier transform along this direction of the k-space data f. The compression procedure can be performed in this hybrid space or in image space by applying an additional Fourier transform in the other two directions. These two approaches give equivalent results, and the procedure is described here in image space for convenience. The compression procedure can be described by

$$\boldsymbol{\rho}'_x(y,z) = \boldsymbol{A}_x \boldsymbol{\rho}_x(y,z), \tag{2.21}$$

with the data vector $\boldsymbol{\rho}_x(y,z) = [\rho_{x,1}(y,z), \rho_{x,2}(y,z), ..., \rho_{x,N}(y,z)]^T$ at position x and 2D image space coordinate (y,z) from N physical coils, the compressed data $\boldsymbol{\rho}'_x(y,z) = [\rho'_{x,1}(y,z), \rho'_{x,2}(y,z), ..., \rho'_{x,M}(y,z)]^T$ from M virtual coils, and the compression matrix $\boldsymbol{A}_x \in \mathbb{C}^{M\times N}$ with $N > M$. The index x indicates that for each position in the frequency encoding direction x a different compression matrix $\boldsymbol{A}_x$ is used.

This problem can be reformulated as a minimization problem

$$\begin{aligned} &\underset{\boldsymbol{A}_x}{\text{minimize}} \quad \sum_{x,y,z} ||(\boldsymbol{A}_x^H \boldsymbol{A}_x - \boldsymbol{I}) \\ bmrho_x(y,z)||^2 \\ &\text{subject to} \quad \boldsymbol{A}_x \boldsymbol{A}_x^H = \boldsymbol{I}, \end{aligned} \tag{2.22}$$

that can be solved independently for every position x. This is done by performing an inverse FFT of the 3D k-space data. For every position in image space x, a data matrix $\boldsymbol{R}_x$ is defined, where every column contains the 2D image data from one coil of spatial position x. The SVD of $\boldsymbol{R}_x$ needs to be calculated

$$\boldsymbol{R}_x = \boldsymbol{U}_x \boldsymbol{\Sigma}_x (\boldsymbol{V}_x)^H. \tag{2.23}$$

$\boldsymbol{U}_x$ is a unitary matrix containing the eigenvectors of $\boldsymbol{R}_x \boldsymbol{R}_x^H$ as columns. $\boldsymbol{\Sigma}_x$ is a rectangular matrix with non-zero singular values of $\boldsymbol{R}_x$ found on the diagonal of $\boldsymbol{\Sigma}_x$. $\boldsymbol{V}_x$ is a unitary matrix containing the eigenvectors of $\boldsymbol{R}_x^H \boldsymbol{R}_x$ as columns.

The first M rows from $\boldsymbol{U}_x$ are used as initial guess for the compression matrix $\boldsymbol{A}_x$. This procedure leads to a non-smooth variation of the compression matrix along x and thus to serious problems in kernel-based reconstructions, because the weightings are not consistent anymore. Therefore, the procedure is further extended [22]. The compression matrix can be multiplied with a unitary matrix $\boldsymbol{P}$ and remains a solution of (2.22). This suggests to find a unitary matrix that renders the behavior of $\boldsymbol{A}$ smooth along x to enable a kernel-based reconstruction. This can be formulated as a minimization problem

$$\begin{aligned} &\underset{\boldsymbol{A}x, \boldsymbol{P}x}{\text{minimize}} \quad \sum_x ||(\boldsymbol{A}_x - \boldsymbol{A}_{x-1})||_F^2 \\ &\text{subject to} \quad \boldsymbol{A}_x = \boldsymbol{P}_x \boldsymbol{A}_x^0, \\ &\qquad\qquad \boldsymbol{P}_x (\boldsymbol{P}_x)^H = (\boldsymbol{P}_x)^H \boldsymbol{P}_x = \boldsymbol{I}, \end{aligned} \tag{2.24}$$

which becomes unique for a fixed $\boldsymbol{P}_x = \boldsymbol{I}$ at some location x. $\boldsymbol{A}_x^0$ is the initial guess and is obtained by solving (2.22). This equation can be solved for each location x via an iterative procedure. Calculate the SVD of $\boldsymbol{C}_x = \boldsymbol{A}_x^0 (\boldsymbol{A}_{x-1})^H$ and use the results to calculate $\boldsymbol{A}_x = \boldsymbol{P}_x \boldsymbol{A}_x^0 = \boldsymbol{V}_x^C (\boldsymbol{U}_x^C)^H \boldsymbol{A}_x^0$ that is used for the location $x + 1$. This results in a smooth behavior of the compression matrix along the frequency encoding direction. Thus, a kernel-based parallel imaging remains possible with this compression technique.

2.3 Accelerate the acquisition: compressed sensing

A different acceleration method, called compressed sensing (CS), has gained a lot of interest recently [23, 24, 25, 26, 27, 28, 29, 30]. The main idea of this approach is that compressibility in a defined transform domain can be utilized for efficient sampling. The compressibility is known from image compression techniques like JPEG and JPEG2000 for natural images or acoustic signals. Traditionally, the signal $\boldsymbol{\rho} \in \mathbb{C}^M$ is sampled at a uniform rate and thus results in a fixed number of N samples. Afterwards, the signal is transformed to the sparsity domain, and only S coefficients are needed to represent the signal in an adequate manner. The rest of the $N - S$ coefficients are discarded. This raises the question, whether it is sufficient to acquire fewer samples if the signal obviously contains less information. In CS it is stated that signals can be recovered from incomplete data with an adequate reconstruction if the signal is sparse, and the measurement and sparsity domain are incoherent [23]. The signal is described here as 1D signal, but any data (2D or 3D) can be reformatted and represented as a 1D signal as well.

2.3.1 Sampling

Linear measurements f_k of the signal $\boldsymbol{\rho}$ are performed. This process can be described with the set of encoding functions $\boldsymbol{\varphi}_k$ and the inner product

$$f_k = \langle \boldsymbol{\rho}, \boldsymbol{\varphi}_k^H \rangle. \tag{2.25}$$

The measurement vector $\boldsymbol{f}$ can be described with the help of the measurement matrix $\boldsymbol{\Phi}$, where the encoding functions $\boldsymbol{\varphi}_k$ are the rows of $\boldsymbol{\Phi}$

$$\boldsymbol{f} = \boldsymbol{\Phi}\boldsymbol{\rho}. \tag{2.26}$$

This is a system of N linear equations. It depends on the measurement matrix, how the inversion of this equation and thus the reconstruction can be performed. If $\boldsymbol{\Phi}$ is an orthonormal matrix, than the recovering process is given by

$$\boldsymbol{\rho} = \boldsymbol{\Phi}^H \boldsymbol{f}. \tag{2.27}$$

If the number of measurements M is larger than the number of unknowns N, (2.27) is an overdetermined system of equations. The pseudo-inverse is calculated to recover a

least squares estimate to the signal $\boldsymbol{\rho}$

$$\boldsymbol{\rho} = (\boldsymbol{\Phi}^H \boldsymbol{\Phi})^{-1} \boldsymbol{\Phi}^H \boldsymbol{f}. \tag{2.28}$$

In CS, the number of measurements M is smaller than the number of unknowns N. In general, an infinite number of solutions to (2.26) exist, but if the signal is sparse, the sparsest solution is unique. Sparsity means that the support of $\boldsymbol{\rho}$ is smaller than N, only S of the N coefficients of the signal $\boldsymbol{\rho}$ are nonzero. In reality, this conditions needs to be relaxed slightly. The signal is called compressible if S coefficients are large and the rest of the coefficients are small.

If the support of $\boldsymbol{\rho}$ is known and thus the location of the S largest coefficients, then the inversion can be performed directly because $N - S$ columns of the measurement matrix can be removed, which corresponds to a reduced number of unknowns. Otherwise, the sparsest solution needs to be found.

2.3.2 Sparsity of signal, compression

Many natural signals have a concise or sparse representation in a specific transform domain. This means that only a few coefficients are significantly larger than zero, and the majority of coefficients are negligible. In a mathematical description, the signal can be expanded e.g. in an orthonormal basis $\boldsymbol{\Psi}$

$$\boldsymbol{\rho} = \sum_{i=1}^{N} \langle \boldsymbol{\rho}, \Psi_i \rangle \Psi_i = \sum_{i=1}^{N} b_i \Psi_i \tag{2.29}$$

with only few large coefficients $b_i = \langle \rho, \Psi_i \rangle$ that are represented by a vector b_S. The rest of the coefficients can be discarded without severe loss of information. The error that is made by discarding coefficients is set by

$$||\boldsymbol{\rho} - \boldsymbol{\rho}_S||_2 = ||\boldsymbol{\Psi b} - \boldsymbol{\Psi b}_S||_2 = ||\boldsymbol{b} - \boldsymbol{b}_S||_2 \tag{2.30}$$

if $\boldsymbol{\Psi}$ is an orthonormal basis. This error is small if the discarded coefficients are small.

The choice of $\boldsymbol{\Psi}$ for MR imaging is described further in the following. The image quality and the visible loss of information caused by discarding coefficients depends on the transform domain and its influence on the visual perception. It is possible to

choose the image domain as the sparsifying transform domain $\mathbf{\Psi}$. Most images have lots of large coefficients, though. Keeping only the largest coefficients results in loss of low signal content. This is a good choice for angiography, because these images are already sparse in the image domain. If $\mathbf{\Psi}$ is chosen to be the Fourier basis, the smallest coefficients are in the periphery of k-space. Discarding these coefficients results in a low resolution image. A different result is obtained if $\mathbf{\Psi}$ is chosen to be the pixel-wise finite difference of the image. Discarding small coefficients in this transform domain results in loss of small differences. Only large differences of neighboring pixels are kept that result in a cartoon-like image. Choosing $\mathbf{\Psi}$ to be the wavelet transform and keeping only large wavelet coefficients is not visible to the human eye for a huge range of compression factors. Thus, wavelets are an obvious transform domain for a wide range of applications.

2.3.3 Incoherence

Compressed sensing requires low coherence between the measurement domain and the sparsity domain. The aliasing in the sparsity domain thus appears incoherent as well and enables reconstruction to distinguish between real and backfolded image content.

The influence of coherence can be understood by assuming the following worst case scenario. The coherence reaches its maximum if the measurement and sparsity domain coincide. This requires knowledge about the support, because otherwise it is likely that only small coefficients are measured due to the sparsity of the signal. Recovery is thus impossible if the small coefficients are known, but not the large ones.

A pair that has minimum coherence is for example the canonical basis with the Fourier basis. Furthermore, a random transform is largely incoherent with any kind of sparsity transform.

In MRI, the measurement basis $\mathbf{\Phi}$ is typically the Fourier basis, and undersampling is usually performed by skipping k-space profiles. It is known that a random choice of the coefficients of $\mathbf{\Phi}$ in all dimensions leads to successful reconstruction with high probability, but this acquisition is impractical due to physical constraints. The frequency encoding direction is always fully sampled and undersampling is performed in the phase encoding directions. During acquisition, there is some freedom in the choice of k-space profiles that can be used to achieve incoherence with the sparsity domain. The set

of measured k-space profiles is called sampling pattern. The sparsifying transform is usually the wavelet or finite differences transform as described in Chapter 2.3.2. It has been shown [23] that a suitable sampling pattern for combined compressed sensing and parallel imaging is Poisson disk sampling [31, 32].

2.3.4 Sparsity enforcing reconstruction

Successful recovery of a sparse signal $\boldsymbol{b}$ from incomplete measurements $\boldsymbol{f} = \boldsymbol{Ab}$ is only possible with an adequate reconstruction. The problem is usually formulated as a constrained minimization problem

$$\min_{\boldsymbol{b}} ||\boldsymbol{b}||_0 \quad s.t. \quad \boldsymbol{f} = \boldsymbol{Ab}. \tag{2.31}$$

There are a couple of existing reconstructions that render distinct undersampling factors possible. Iterative greedy algorithms try to find the optimal solution to the reconstruction problem with ℓ_0 norm step by step. In each iteration, the support of the signal is updated by adding the column of the measurement matrix with highest correlation to the residual. Some examples for such algorithms are matching pursuit [33], Orthogonal Matching Pursuit (OMP) [34], and Compressive Sampling matching pursuit (CoSaMP) [35].

Convex relaxation algortihms represent a different class of reconstruction solving convex optimization problems through linear programming to recover the original signal. The minimization problem is formulated as

$$\min_{\boldsymbol{b}} ||\boldsymbol{b}||_1 \quad s.t. \quad \boldsymbol{f} = \boldsymbol{Ab}. \tag{2.32}$$

with the convex relaxation ℓ_1 of the non-convex ℓ_0 norm. Examples for this kind of reconstruction are Basis Pursuit (BP) [36], Basis Pursuit De-Noising (BPDN) [36], and Least Absolute Shrinkage and Selection Operator (LASSO) [37].

Iterative thresholding algorithms constitute to the third group of algorithms that impress with easy implementation and fast computation. These algorithms are two-step algorithms that perform in each iteration hard- [38] or soft-thresholding [39] in the domain, where the signal is supposed to be compressible, and enforce data consistency in measurement space. Extensions were already proposed, like for example Message Passing (MP) [40], Belief Propagation [41], Expander Matching Pursuit [42], Sparse

Matching Pursuit [43], Sequential Matching Pursuits [44], and Fast Iterative Shrinkage-Thresholding Algorithm (FISTA) [45].

Non-convex optimization algorithms using the l_p norm

$$||\boldsymbol{b}||_p = \left(\sum_i |b_i|^p \right)^{1/p} \tag{2.33}$$

exist to reconstruct the signal, like FOCal Underdetermined System Solution (FOCUSS) [46] ($1 \leq p \leq 2$), Iterative Re-weighted Least Squares [47], Sparse Bayesian Learning Algorithms [48], and algorithms based on Monte-Carlo [49].

The last type of reconstructions mentioned here are called Bregman iterative algorithms [50] that find solutions to the Basis Pursuit problem by solving an unconstrained problem with a small number of instances. The number of iterations ranges from 2 to 6 with this algorithm and is thus computationally efficient.

The aforementioned algorithms are not specific to any kind of application, but there are a number of algorithms that are specifically designed for medical imaging, especially for MRI [23, 51, 52, 53, 54]. Further examples are given in Section 2.4.

2.4 CS in MRI

The application of CS to MRI is obvious, because the data acquisition is performed in k-space that can be interpreted as a linear combination of data from image space. The incoherence of the measurement domain and the sparsity domain can be achieved with the choice of an adequate sampling pattern. Furthermore, in some applications, like angiography for example, the images are already sparse in image space [55], and no further transformation is needed, while the total variation or the ℓ_1 norm of the wavelet transformed image are adequate measures for the sparsity in other applications.

An existing and frequently used technique to accelerate the acquisition in MRI is parallel imaging, described in 2.2.4. Several acquisition and reconstruction techniques aim at combining parallel imaging and compressed sensing [51, 52, 56] to achieve even higher acceleration factors. As described in Section 2.2.4, the parallel imaging techniques can be divided into image space and k-space related methods that can both be

combined with CS. Furthermore, the reconstructions can be performed sequentially, i.e. CS-SENSE [56] or k-t Sparse GROWL [57], or combined into one problem to be solved [51, 52, 58, 59].

Because an optimal reconstruction is obtained with SENSE for known and exact coil sensitivity maps [8], several approaches were presented to combine CS and SENSE [56, 59, 60, 61, 62]. A recently proposed algorithm, called Sparse BLIP [58], simultaneously estimates the coil sensitivities and reconstructs the image in an iterative manner. To avoid artifacts due to incorrect coil sensitivities, an additional total variation (TV) constraint is included in the minimization problem. This minimization problem is divided into two sub-problems, each minimized in individual steps for every iteration. The initial coil sensitivities are estimated from the fully sampled central k-space. The problem of incorrect coil sensitivities is also addressed in [52] by using not only one set of coil sensitivities, but two. The sets of coil sensitivities are estimated from the fully sampled central region by solving an eigenvalue problem that is further described in Chapter 6. A combination of CS with kernel-based parallel imaging is presented in [51, 57].

In dynamic MRI, the sensitivity information provided by a pre-scan is not accurate for all temporal phases. TSENSE [63] improves the sensitivity information by enabling temporal change. This can also be used in CS techniques, but leads to significantly increased reconstruction times.

Furthermore, CS was applied to higher-dimensional signals including the additional temporal dimension for cardiac cine imaging [64] or dynamic contrast-enhanced imaging in general [65, 66, 67]. These imaging procedures aim at increasing the spatial or temporal resolution of the imaging series by exploiting redundancy in the temporal domain. The redundancy was already exploited without using compressed sensing in k-space sharing techniques like keyhole imaging [68, 69] or TRICKS [70]. Furthermore, existing parallel imaging techniques were extended to exploit temporal correlation like k-t BLAST/k-t SENSE [71], k-t GRAPPA [72] and SPEAR [73].

The adequate CS reconstruction technique is dependent on the application. For example, the motion of the heart is expected to be periodic, thus it is obvious to modulate each voxel by a linear combination of Fourier exponentials that can be learned from previously acquired training data [71, 74, 75, 76]. This can be extended to exploit CS as

well and was described in several publications [53, 64, 77]. Because of the lack of periodicity in cardiac cine MRI and naturally for dynamic contrast enhanced imaging, the reconstruction results often suffer from artifacts or require a large set of basis functions. Therefore, based on the assumption that the signal has low rank, the interest in learned orthogonal dictionaries from the undersampled data itself increases [78, 79, 80, 81].

An approach called blind compressed sensing (BCS) is proposed in [82]. A dictionary is learned from the data itself and is thus comparable to low-rank approaches, but is not necessarily orthogonal. Furthermore, the coefficients are thought to be sparse.

A different approach is known as k-t SPARSE-SENSE that has several applications [59, 83] and exploits the joint multi-coil sparsity to accelerate dynamic MR imaging. This technique was further developed recently to be used with golden-angle radial acquisition [84].

A recently proposed sequential PI and CS reconstruction for dynamic MRI is k-t Sparse GROWL [57]. GROWL, which is a specific k-space based parallel imaging technique, is performed before applying flexible virtual coil (FVC) k-t CS. GROWL recovers missing k-space profiles around acquired k-space profiles and thus lowers the overall reduction factor, before the CS reconstruction is performed. FVC is a special channel compression technique that is used for lowering the computational cost of the CS reconstruction. After the CS reconstruction, the signals from the original number of channels are recovered.

Motion is a frequently occurring problem in dynamic MRI that results in artifacts as well as reduced sparsity in images from reconstructions exploiting low rank and periodicity. Approaches were proposed to compensate for this motion by assuming rigid or non-rigid motion and binning the data [85, 86]. Reconstruction of the individual bins and performing image transformations defined by the motion model can be used to jointly reconstruct motion corrected CINE images of all bins [85]. MASTeR [87] is a different algorithm that individually reconstructs the images from the time-series with a CS reconstruction in the first step and afterwards solves a modified problem that enforces data consistency and sparsity of the differences to temporally neighboring images.

Alternatively, the transformation can be performed before CS reconstruction [54, 88]. A recently proposed method, called BLOSM [89], divides the image in small blocks

and tracks them in the following images of the time series. Low rank is enforced on the temporal evolution of the blocks.

A different assumption for improved dynamic MRI is group sparsity [90, 91], called k-t group sparse reconstruction. It is based on the structure of the MR signal in x-f space, neighboring voxels in image space from the support region of the image are grouped together. The optimization problem is reformulated and enforces sparsity on the mixed ℓ_1-ℓ_2 norm of the groups [91]. A different grouping method based on the intensities of the voxels was presented recently [90].

Apart from the redundant information from multiple receive channels and temporal evolution, redundancy is also present in the images from multiple echoes. A joint reconstruction approach is proposed in [26, 92] to exploit this knowledge.

2.5 Water-fat separation

In conventional MRI the signal mainly results from protons of the water molecules and slightly shifted in MR spectrum from protons of the fat molecules. The signal from fat is often hyperintense and can potentially obscure underlying structures in images. Therefore, the suppression of fat is frequently desired and can be performed during the acquisition, or alternatively during the reconstruction. The suppression during acquisition is based on the difference in relaxation time (inversion recovery [93]) and difference in resonance frequency $\Delta\nu$ (selective saturation [94]) between water and fat. These methods have disadvantages, like longer scan time, lower SNR, and imperfect suppression due to magnetic field imhomogeneities. Some of these disadvantages can be overcome by a water-fat separation performed during reconstruction. This is realized in chemical shift-based water-fat separation methods [95] that acquire data at several echo times and that solve for the water and fat content afterwards. The signal of the n-th echo at each pixel j in image space is given by a weighted sum of the complex water W and fat F signals

$$\rho_{nj} = (W_j + F_j e^{i\Theta_n}) e^{i\phi_n} \tag{2.34}$$

with the dephasing angle $\Theta = 2\pi\Delta\nu\, t_n$ and the echo time t_n. The phasor ϕ_n contains the error induced by field inhomogeneity. Different Dixon methods differ in the number of acquired echoes, the corresponding constraints on the echo times, and the separation procedure. One- to multi-echo methods are used dependent on the application. A small

number of echoes with flexible echo times is favorable for abdominal imaging with breath-hold requirements, because the breath-hold clearly restricts imaging time. While single-echo techniques are prone to large errors, if no prior knowledge is available [96], two- and three- echo methods provide high quality water-fat separation and enable flexible echo times [97, 98, 99, 100, 101].

In this work, a two-point water-fat separation with flexible choice of echo times [97] is used. The separation of the signal into its water and fat content is performed in three subsequent steps. The first is the computation of possible values for the phasor for each pixel individually. Afterwards, an appropriate value for the phasor is selected out of the possible values, with an additional smoothness constraint on the spatial variation of the phasor. As a final step, the water and fat content are calculated individually for each pixel based on the signal from the two echo times and the phasor.

2.6 Contrast agents

Contrast in MRI is generated by different physical properties of neighboring tissues. These physical properties include proton density, relaxation properties like T_1, T_2, and T_2^*, and differences in resonance frequency. The differences in these properties of the different tissue types are sometimes quite small and thus difficult to detect. Furthermore, partial volume effects can lead to canceled signal in individual voxels. Enhancement of these characteristic properties can be achieved by the application of contrast agents that are frequently used to facilitate better diagnosis based on the MRI images. The temporal evolution of the contrast agent uptake and wash-out has a further significant influence on diagnosis, because perfusion varies for different tissue types.

Enhancement of the characteristic is only possible for some properties. The proton density can not be changed and is thus always left unattached, but it is possible to change the relaxation properties of the tissue types. Relaxation of individual water protons is induced by dipole-dipole interactions facilitated by small magnetic field fluctuations in the neighborhood of protons. The quantitative influence of contrast agents on T_i is described by the relaxivity

$$r_i = \frac{\Delta(1/T_i)}{c} \tag{2.35}$$

with the concentration of the contrast agent c.

Paramagnetic contrast agents (i.e. Gadolinium) have unpaired outer electrons and thus act as dipols with large magnetic field fluctuations. If these magnetic field fluctuations are close enough to the Larmor frequency of the protons, the relaxation of the neighboring protons is significantly increased and thus leads to enhanced contrast in T_1 weighted MR images. Although the Gadolinium is caged in the contrast media, the concentration of Gadolinium has been lowered during the years to decrease undesired side effects due to the toxicity of Gadolinium. Gadolinium containing contrast agents can lead to nephrogenic systemic fibrosis (NSF) in case of chronic or acute renal impairment even days after examination.

Superparamagnetic contrast agents (i.e. iron oxide), called SPIO, modify the contrast in T_2/T_2^* weighted MR images by inducing large local magnetic field inhomogeneities. The protons within an individual voxel thus experience significantly different magnetic fields and thus precess at different frequencies that leads to signal dephasing and thus lowers T_2/T_2^* intensity in tissues containing the contrast agent.

Chapter 3

Sampling in CS MRI

This chapter describes a CS sampling strategy for optimized 3D Cartesian MR imaging. The 3D k-space is undersampled in the two phase encoding directions. The undersampling is described for a 2D plane, where each sampling point indicates a profile.

As stated earlier, the sampling-pattern is essential for the reconstruction results. The coherence between the sensing basis and the representation basis influences the desired number of samples for successful reconstruction. Random undersampling of k-space with sufficient profiles results in low coherence for an arbitrary representation basis. However, there is a non-vanishing probability that random undersampling results in non-optimal sampling-patterns, either characterized by areas with tendencies of clustering sampling points and large holes in sample distributions, or by missing important areas of k-space. This is especially relevant for uniform undersampling, because every random realization has the same probability. Variable-density sampling could be considered as a means of helping to avoid some of these effects, but is still prone to the above mentioned issues. A possibility to prevent holes and clustering is a Poisson-disk distribution of samples that is at the same time able to ensure appropriate sampling of important regions of k-space.

3.1 Uniform Poisson-disk sampling

For performing CS, the measurement matrix has to lead to incoherence between the measurement domain and the sparsity domain. In CS for MRI, the measurement matrix is composed of the Fourier encoding matrix, the sparsifying transform matrix, and the

undersampling matrix. The choice for the sparsity/compressible domain can be modified, but needs to be adequate for the signal, while the undersampling matrix can be modified. Among different possibilities to achieve incoherence by the sampling pattern, a variant of a Poisson-disk distribution of samples is used here. A Poisson-disk distribution [23, 31, 32] is a pseudo random distribution of samples with constraints that prevents clustering by defining a minimum distance between neighboring samples.

There are different methods to generate a Poisson-disk distribution in a 2D plane without grid [102, 103]. In MRI, it is advantageous to acquire data on a Cartesian grid to be able to use a FFT for a fast transformation between the image and Fourier domain. Poisson-disk distributions generated in a plane without grid can be mapped on a Cartesian grid. Alternatively, distributions can be generated directly on a Cartesian grid. This method is proposed in this work and is described in the following sections.

The coordinates of the samples can be generated directly on a Cartesian grid by restricting the distances between samples by a lower bound κ_{min}. A compliant maximum distance can be implicitly defined by using the appropriate pair of κ_{min} and mean reduction factor $R = \frac{N_t}{N}$ in the plane. N_t is the total, while N is the desired number of samples in k-space. With the desired number of samples and the covered k-space area, the average distance between samples can be calculated and rounded off to the next possible value on a Cartesian grid to define κ_{min}, i.e. the lower bound on the distance between samples. To study the influence of the lower bound and the reduction factor R on the enforced upper bound, the situation is described in more detail in 1D.

For a completely random distribution of N samples on N_t possible positions on a Cartesian grid, the worst case, i.e. the largest hole, occurs if the samples are clustered on one side. The size of the hole is $N_t - N$ in this case, which equals the number of samples that are left to choose from. This describes the worst case. For all other distributions, the distances between samples lie on the interval $[1; N_t - N]$. If the distribution of samples is not completely random, but with an additional constraint on the minimum distance κ_{min} between samples, then the situation is slightly different. The worst case is once again closest-packing of samples, which is less dense than in the completely random case described before. The largest hole is given by $N_t - \kappa_{\text{min}} N$, with

$$\kappa_{\text{min}} = \lfloor \frac{N_t}{N} \rfloor = \max \left\{ k \in \mathbb{Z} | k \leq \frac{N_t}{N} \right\} \geq 1. \tag{3.1}$$

The size of the hole, $N_t - \kappa_{\text{min}} N$, equals once again the number of samples left to choose from. For any distribution better than the worst case, the possible distances of samples are from the interval $[\kappa_{\text{min}}; N_t - \kappa_{\text{min}} N]$. Because $N_t - \kappa_{\text{min}} N \leq N_t - N$, the maximum enforced distance between samples is smaller or equal to the size of the completely random distribution. This restriction is able to prevent large wholes if κ is sufficiently large, but it is not strict enough to prevent smaller holes. This is especially relevant for reduction factors smaller than two, because the value κ_{min} is reduced to $\kappa_{min} = 1$ in these cases and is equivalent to random sampling. The concept of relaxation [32], described later, is needed here.

For the sake of completeness, the minimum distance is given for the 2D case:

$$\kappa_{\text{min}} = \lfloor \sqrt{\frac{N_t}{N}} \rfloor = \max \left\{ k = \sqrt{x^2 + y^2}, x, y \in \mathbb{Z} | k \leq \sqrt{\frac{N_t}{N}} \right\} \geq 1. \tag{3.2}$$

It is stated earlier in this section that the largest possible hole is related to the samples that are still left, after N samples were chosen. If no possible samples are left, it follows by implication that the maximum distance is restricted by an upper bound $2\kappa_{\text{min}}$. The number of samples is not predetermined with this method, but can be restricted by starting with a larger minimum distance $\kappa_0 > \kappa_{\text{min}}$. This leads to the concept of relaxation. Relaxation is known from continuous Poisson-disk distributions [32, 103] and is used there to ensure termination of the Dart-Throwing algorithm. A Poisson-disk distribution with a relatively large radius of forbidden samples is created to fill the plane once, until no possible samples are left, followed by decreasing radii, until the desired sampling density is reached.

This can be applied directly to Cartesian Poisson-disk distributions. With this method, the maximum possible distance between two samples becomes $2\kappa_0$. A quasi random distribution of samples with constraints is achieved. The resulting distance to the nearest neighbor is restricted to the interval $[\kappa_{\text{min}}; 2\kappa_0]$.

While the benefit for large reduction factor is not immediately obvious, this is the case for distributions with $\kappa_{\text{min}} = 1$ on a Cartesian grid. Without relaxation, a pure random distribution would result.

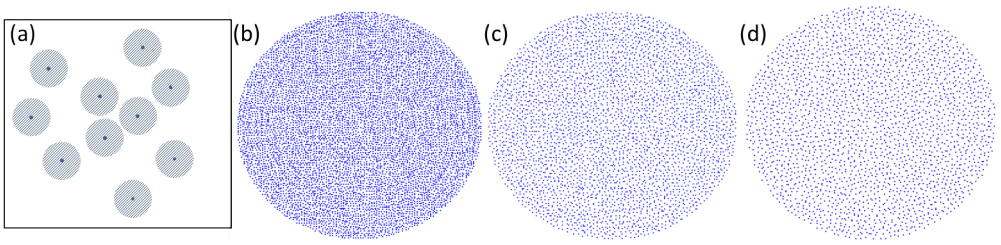

Figure 3.1: Realization of a Poisson-disk distribution. A description of different sets using a uniform random distribution is given in (a). Every chosen sample, indicated by a blue dot, is surrounded by an area of constant diameter κ_{min}, where random selection is prohibited. Additional samples can only be chosen from the white area. Generated realizations of uniform Poisson-disk distributions for reduction factors R of (b) 4, (c) 8, and (d) 12.

3.1.1 Implementation details and evaluation

The choice of random samples out of a defined and fixed set can be made with a Dart-Throwing [102] approach, which subsequently chooses random samples out of the original set S. If one sample has been chosen already, the random selection is repeated. This immediately leads to problems for large numbers of desired samples, because repeated random selections become more frequent as the sampling density increases, which implies prohibitively long computation times. To avoid this, random selections are performed on a temporally changing subset of the original set: the set of available samples P. For illustrative purposes, Figure 3.1(a) is given. The samples are randomly chosen out of the subset $P = S \backslash (M \cup T)$, which is the set of available samples (samples out of the unmarked area). M is the set of already chosen samples (blue dots) and with the additional definition of T, which is the set of forbidden samples (occupying a circle) around the already chosen ones, a minimum distance restricted distribution can be realized as opposed to a pure random distribution. Updates of the subset P need to be performed after every random selection of a sample.

In case of autocalibrated PI, the central k-space area can be fully sampled, but the remaining general approach remains applicable.

For the calculation directly on a Cartesian grid, C-code has been created for this work, following the description given above. Generated realizations of the distributions are given in Figures 3.1(b-d), which differ by the reduction factor, (b) $R = 4$, (c) $R = 8$, and (d) $R = 12$.

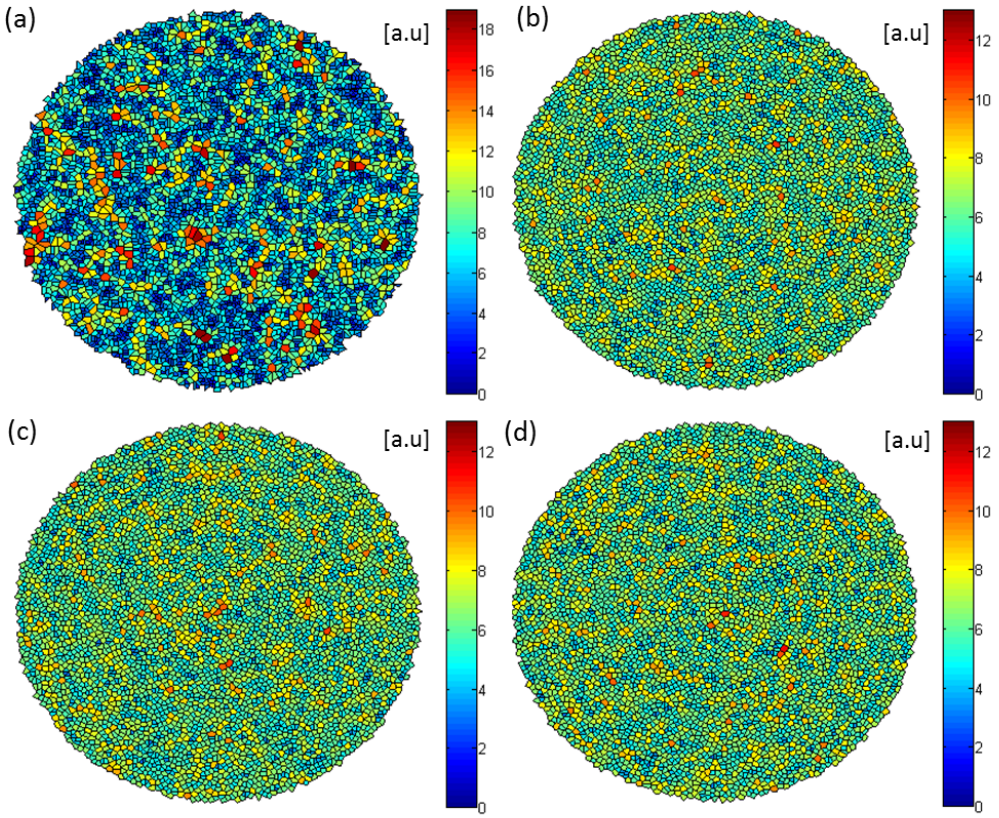

Figure 3.2: Voronoi diagram for uniform sampling density. (a) is from a random sampling-pattern, with Voronoi areas spread over a wide range. (b) is from a Poisson-disk distribution, while (c,d) are from Poisson-disk distributions with relaxation. (c) and (d) differ by the starting value (c) $\kappa_0 \approx \kappa_{min} + 2$, and (d) $\kappa_0 \approx \kappa_{min} + 5$. The range of the size of the Voronoi areas is smaller in (b-d), compared with (a). A smaller range indicates a uniform distribution without holes and clustering of samples.

To evaluate the generated distributions further, Voronoi diagrams are calculated for different uniform density distributions and a reduction factor $R = 6$. The Voronoi diagram for a random distribution without constraints is given in Figure 3.2(a). The disadvantages of this distribution are clearly visible, the sizes of the areas are spread over a wide range, see also Figure 3.3(a). Clustering of samples and large holes are not prevented. For the Poisson-disk distribution without relaxation, shown in 3.2(b), the size of the areas is clearly restricted, see also Figure 3.3(b). The relaxed Poisson-disk distributions, shown in Figure 3.2(c,d), are comparable to the case without relaxation. There is no difference visible, because the target value κ_{min} resulted in a distribution with hardly any possible samples left. The same reason holds for the similarity of (c) and (d), which differ in the starting value κ_0. The means of Voronoi areas, as well as the standard deviations and the maximum values are summarized in Table 3.1. The mean area approximates the reduction factor in all cases. The standard deviation, as well as

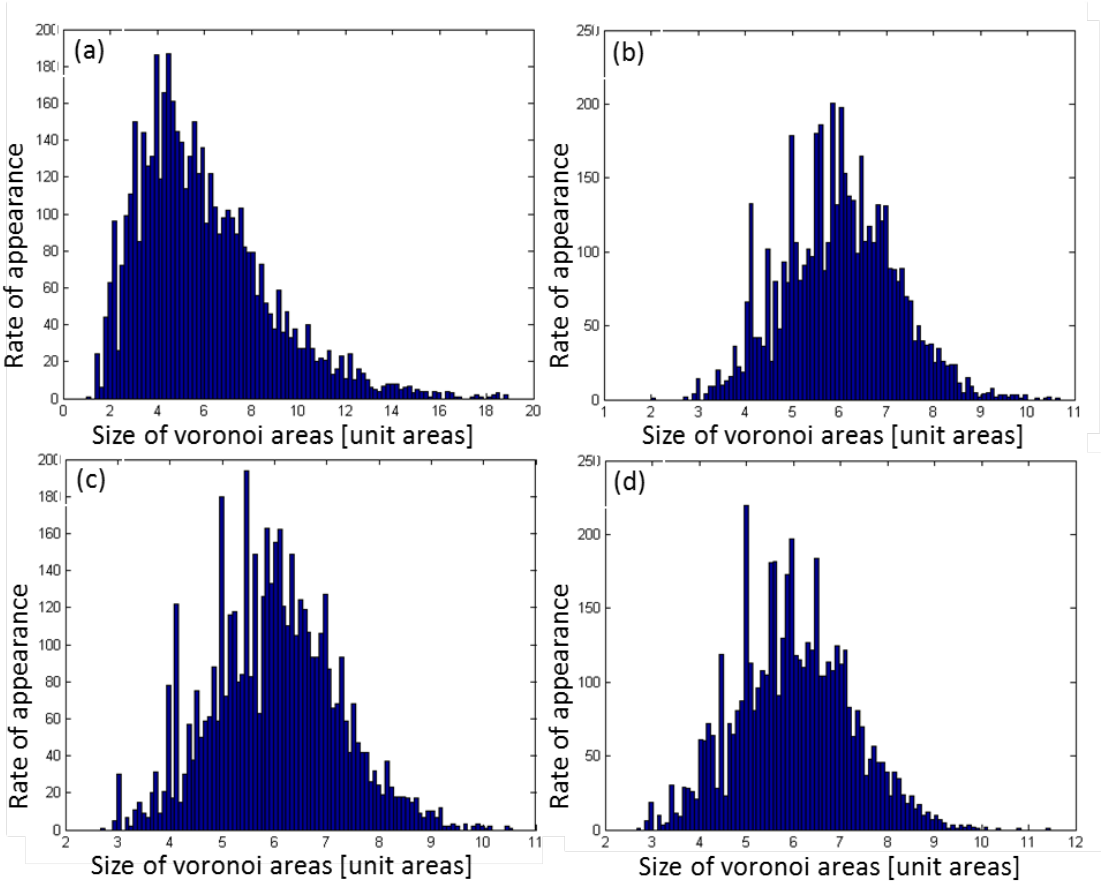

Figure 3.3: Histogram of Voronoi areas for uniform sampling density distributions. (a) Histogram of the random distribution; (b) Poisson-disk distribution; (c,d) Relaxed Poisson-disk distributions, same examples as in Figure 3.2. (b-d) indicate similar distributions, while (a) is obviously spread over a wider range.

the maximum area differ significantly between the random and the Poisson disk case. The differences between the different PD distributions are not significant.

3.2 Variable-density Poisson-disk sampling

The signal distribution in k-space depends on the geometry, the structure of the object, and the experimental settings. Nevertheless, they always have one property in common: the highest signal amplitude is accumulated in the central part of k-space and decays to the periphery. The exact decay as well as the best fitting function depends on the object and the protocol. In MRI, without acceleration using compressed sensing, k-space is typically sampled on a Cartesian grid with constant distance between samples (uniform density), fulfilling the Shannon sampling theorem. If CS undersampling is performed,

Table 3.1: Analysis of Voronoi diagram. For realization of different distributions, Voronoi diagrams are calculated and the means, standard deviations and the maxima of the resulting areas are calculated and summarized in this table in unit areas of k-space. The mean area approximates the reduction factor and the standard deviation gives a hint for the spread of the areas. Clustering corresponds to smaller areas, while holes correspond to large areas. The random distribution is worse than the other methods, which result in similar quality of distributions.

	Random sampling	Poisson disk (PD)	Relaxed PD $\kappa_0 \approx \kappa_{min} + 2$	Relaxed PD $\kappa_0 \approx \kappa_{min} + 5$
mean	5.97	6.01	6.0	6.01
std	2.79	1.2	1.21	1.19
max	18.9	10.3	10.6	11

it is essential to decide, which sampling density (uniform or variable density) should be achieved, and which samples should be acquired. It is known from image compression and previous compressed sensing applications that natural images as well as MR images have a sparse representation in the wavelet domain [23]. The scales in the wavelet domain are band-pass filtered images of the original signal. It is further known that the coarse scales are dense compared with the sparse fine scales [23]. Therefore, higher frequencies potentially need less data to be reconstructed, and undersampling is performed according to a variable-density with decaying density towards the periphery of k-space. The sampling density can be optimized for a selected protocol and anatomy.

In Section 3.1, generation of the sampling-pattern for a uniform Poisson-disk distribution is described. Therefore, this concept is adjusted to generate a variable density in k-space in the following. It is obvious that a variable density is achieved if the radius κ of forbidden neighborhood around a sample becomes location dependent. In the next sections, the construction of a reasonable function $\kappa(i)$ is derived. The variable i counts through all possible positions in k-space.

3.2.1 Probability mass function

The probability mass function (pmf), denoted by $p_I(i)$ here, is the most probable fourier representation of the imaged object. It gives the probability that one sample is placed at one specific location i in k-space. The corresponding sample space consists of all locations in k-space and as a probability mass, the sum of p over all locations is one.

For uniform sampling, the samples are chosen randomly from the set of possible samples with a homogeneous probability mass function (pmf). To achieve a variable density, the samples are chosen from a non-uniform pmf instead.

Variable-density sampling was motivated with the differing sparsity of the wavelet scales and the knowledge about the typical signal distribution in k-space. The exact decay of the sampling density towards the k-space periphery needs to be selected. One approach is presented in [23], where a decaying sampling density according to the power of one to six of the distance from k-space center is proposed. This empirically reduces the interference in the transform domain, but is not proven to be optimal. In [104], the signal distribution in k-space is further analyzed, and a formula is derived empirically for the signal power spectrum

$$I(l) \propto \left(l^2 + \left(\frac{\epsilon}{2\pi} \right)^2 \right)^{-3/2} . \tag{3.3}$$

In this equation, l is the distance from k-space center, and ϵ is an empirical parameter that is chosen according to the relative size of objects compared with the FOV. A factor of 25 is proposed for MR images [104].

Instead of giving a formula for the signal distribution, it can be determined empirically on a series of MR training images for specific applications, briefly described below. As mentioned before, in 3D imaging, the frequency-encoding direction is fully sampled, and undersampling is only performed in the 2D phase-encoding plane. From the 3D k-space data, a 1D Fourier transform in the frequency-encoding direction is performed to achieve a hybrid space. An averaging over the slices results in smoothing of the 2D k-space data. This mean distribution is normalized to fulfill the requirements of a pmf. The resulting pmf is a function of the two coordinates k_y and k_z. It describes roughly the signal and its information distribution in k-space, and is further used to guide the sampling process by influencing its sampling density.

3.2.2 Sampling density function

The aim is to create a variable-density Poisson-disk sampling by influencing the radius κ of forbidden neighborhood around a given sample. As stated earlier, the size of the forbidden neighborhood sets an upper bound on the sampling density. Therefore, the radius needs to match the final location-dependent sampling density function (sdf) for

a random choice of N samples and needs to be known in advance. Thus, the resulting mean sampling density function for a fixed number of chosen samples from a pmf $p_I(i)$ needs to be determined. The sdf can be regarded as the expectation value of finding a sample at one specific location.

One possibility is a Monte-Carlo simulation of the sdf from the pmf by choosing N samples randomly multiple times and then averaging over the individual repetitions. For this procedure, a large number of realizations of the distribution must be performed. This is computationally expensive, and therefore, not done here.

The procedure, how the sdf $d(i)$ can be calculated exactly and in a less time consuming fashion, is derived in the following. The aim of the calculation is the sdf $d(i)$ that is achieved if N samples are randomly chosen without recline from a given pmf $p_I(i)$ out of a finite set. It is obvious that the sdf depends on the total number of samples N. Two cases are immediately clear. If $N = 1$, then one sample is chosen out of the total number of possible samples N_t, and therefore, sdf and pmf equal each other. In the other case, if $N = N_t$, then all possible samples are chosen, which is full sampling and is equivalent to a homogeneous sdf $d(i) = 1$, independent of the pmf $p_I(i)$. The cases in between require deeper insights.

A prediction for the distribution of N samples that are chosen without recline out of a total number of N_t not equally probable samples is challenging, because the experiments are not independent of each other. It is, therefore, necessary to redefine this case with the equivalence of choosing samples with recline, but if one sample has been chosen already, an additional try is performed. This way, the probability of the samples in each try stays constant, because the experiments are independent, but the total number of trials ($N' > N$) is unknown in advance.

The experiments are described by N_t multivariate independent variables $Z_1, ..., Z_{N_t}$. Let $Z_1, ..., Z_{N_t}$ be the stochastic variables giving the times the locations $1, ..., N_t$ were chosen. The sample spaces of $Z_1, ..., Z_{N_t}$ are $[0, 1, ..., N']$. For each location $i \in [1, ..., N_t]$ in the k_y-k_z plane, the probability that this sample is chosen in one try is given by the pmf $p_I(i)$. For N' independent trials, each Z_i follows a binomial distribution with pmf Ψ and parameters $p_I(i)$ and N'.

During the process of generating a sampling pattern, it is decided, whether one sample is taken once or not, repeated selection is no option. Therefore, a simplified stochastic

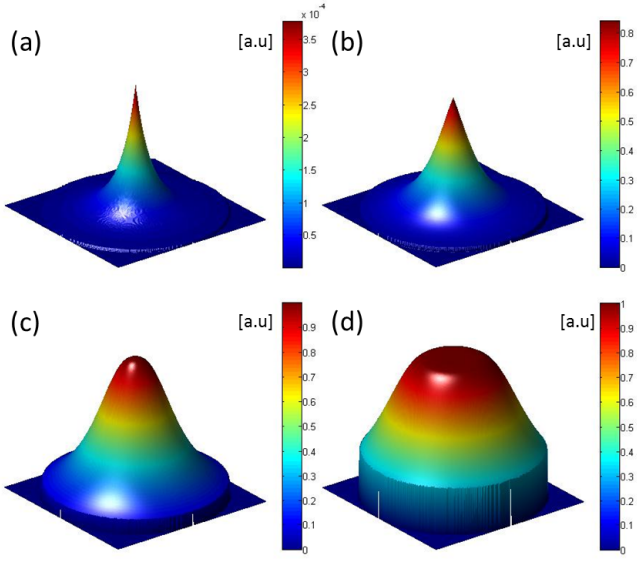

Figure 3.4: Illustration of probability mass funtion (pmf) $p_I(i)$ and sampling density function (sdf) $d(i)$ for an example pmf. The pmf (a) is decaying according to the power of 6 with the distance to k-space center. Based on the pmf, the sdf is determined for different undersampling factors $R = \frac{N_t}{N}$: (b) 8, (c) 4, (d) 1.5. From (b-d) the tendency to more uniform sampled k-space for very low reduction factors can be seen.

variable S_i with a reduced sample space $[0, 1]$ compared with Z_i is sufficient. In this sample space, one means that the sample is taken, and zero means that the sample is not taken. The corresponding pmf Φ of S_i can be calculated from the known pmf Ψ of the variable Z_i:

$$\begin{aligned} \Phi_{S_i}(s_i = 0) &= \Psi_{Z_i}(z_i = 0) = (1 - p_I(i))^{N'} \\ \Phi_{S_i}(s_i = 1) &= \Psi_{Z_i}(z_i > 0) = 1 - \Psi_{Z_i}(z_i = 0) = 1 - (1 - p_I(i))^{N'}. \end{aligned} \tag{3.4}$$

The sdf $d(i)$ at location i is the expectation value $\mathbb{E}[S_i]$ of the variable S_i and is calculated according to the formula

$$d(i) = \mathbb{E}[S_i] = 0 \cdot (1 - p_I(i))^{N'} + 1 \cdot (1 - (1 - p_I(i))^{N'}) = 1 - (1 - p_I(i))^{N'}. \tag{3.5}$$

The equations given above still contain the unknown number of trials N'. This can be determined by making use of an additional constraint: The total number of selected samples needs to be N. Mathematically, this can be described with the help of the expectation value of the stochastic variable $T = \sum_{i=1}^{N_t} S_i$:

$$\mathbb{E}[T] = \mathbb{E}[\sum_{i=1}^{N_t} S_i] = \sum_{i=1}^{N_t} \mathbb{E}[S_i] = \sum_{i=1}^{N_t} 1 - (1 - p_I(i))^{N'} = N_t - \sum_{i=1}^{N_t} (1 - p_I(i))^{N'}. \tag{3.6}$$

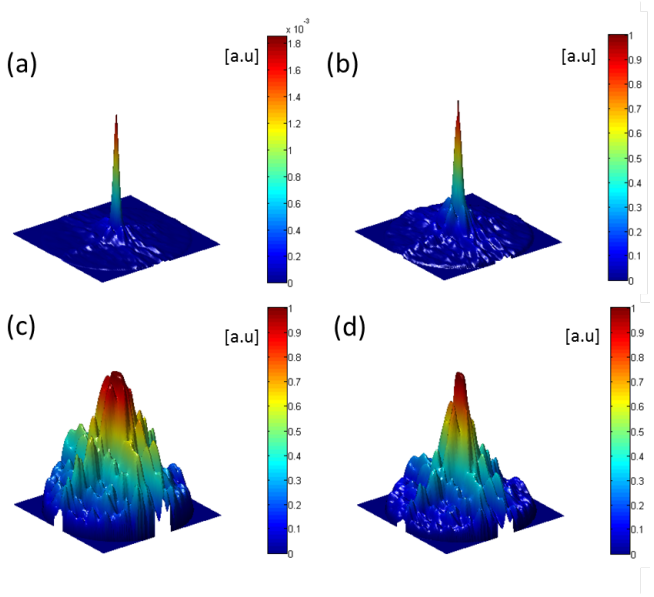

Figure 3.5: Illustration of pmf $p_I(i)$ and sdf $d(i)$ based on invivo data. The pmf (a) is calculated from one invivo dataset as described in Section 3.2.1. Based on the pmf, the sdf is determined for different undersampling factors $R = \frac{N_t}{N}$: (b) 20, (c) 5, (d) 3.

This results in the following formulation of the constraint:

$$\mathbb{E}[T] = N. \tag{3.7}$$

It is possible to determine N' in a few iterations beginning with $N' = N$ and calculating the corresponding expectation value $N_{app} = \mathbb{E}[T]$, which is the result of (3.6) and fulfills the condition $N_{app} < N$. The value N' for the next iteration is $N' = N' \frac{R}{N_{app}}$. The iterations are performed, until $N - N_{app} < 1$. The final N' defines the sdf according to (3.5).

The cases described above for $N = 1$ and $N = N_t \Leftrightarrow \lim_{N' \to \infty}$ can also be described by (3.5) and give consistent results:

$$\begin{aligned} N = 1 \rightarrow \quad & d(i) = 1 - (1 - p_I(i))^1 = p_I(i) \\ N = N_t \rightarrow \quad & d(i) = \lim_{N' \to \infty} 1 - (1 - p_I(i))^{N'} = 1. \end{aligned} \tag{3.8}$$

An illustration is shown in Figure 3.4(a) with a pmf $p_I(i)$ decaying according to the power of 6 with the distance to k-space center. The resulting sdf $d(i)$ is given in Figures 3.4(b-d) for different numbers of undersampling factors R. It indicates that, for low N, the sdf shows similar behaviour as the pmf, which converges towards one on the whole plane for $N \to N_t$. In Figure 3.5(a), the pmf is determined from in

Table 3.2: Computation times for determination of location-dependent radii κ of forbidden neighborhood for a given probability mass function. The number of iterations is rapidly increasing for $R \to 1$, but the result for the case $R = 1$ is immediately clear ($d(i) = 1$) and requires no calculation.

Reduction factor (R)	Iterations	time [s]
4	6	0.104
3	7	0.103
2	10	0.104
1.5	15	0.115
1.2	25	0.156
1.1	38	0.254
1	3080	7.673

3.2.2.1 Computational cost

The algorithm described in Section 3.2.1 and Section 3.2.2 was implemented in C. Its computation time is influenced by the number of iterations needed to achieve convergence. In every iteration, $\mathbb{E}[T]$ is calculated, consisting of a sum over all locations. The number of iterations increases for decreasing reduction factors and has strong influence on the computation time for low reduction factors. For reduction factors larger than $R = 1.1$, the computation times are typically under 1 s. Lower values of the reduction factor result in higher computation times (for example 7.67 s for a matrix size of 300×100 and $R = 1$, see Table 3.2). On the other hand, for the case $R = 1$, it is unnecessary to even start the calculation because of $sdf = 1$ for the whole plane. The algorithm was tested for multiple values of the reduction factor R on a 64-bit system with 12 GB RAM and an Intel Xeon processor with 2.67 GHz. The application is designed to run on a single core. The results for a Cartesian grid of size 300×100 are given in Table 3.2, showing that acceptable computation times can be found for useful reduction factors.

3.3 Realization of variable-density Poisson-disk distribution

In the last section, the determination of a sdf from a meaningful pmf was derived. The missing step is the determination of the function κ. The relation between the sdf and

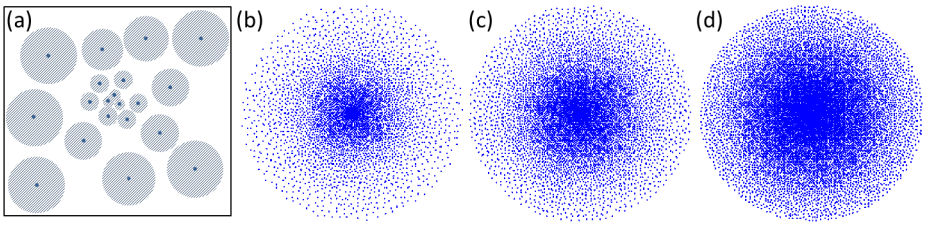

Figure 3.6: Variable-density Poisson-disk sampling pattern. Location-dependent forbidden neighborhood (a). Please note the different diameters of the neighborhood around the samples. Resulting sampling patterns are given for different undersampling factors $R = \frac{N_t}{N}$: (b) 8, (c) 5, and (d) 3. The underlying pmf is taken from Figure 3.4.

the mean distance $\bar{\kappa}$ between samples is given by

$$d(i) \propto \frac{1}{\bar{\kappa}^n}. \tag{3.9}$$

In this equation, κ is given in units of gaps between adjacent samples on a Cartesian grid, and n is the dimension of the undersampling space. For a given sdf $d(i)$, it is therefore possible to determine the location-dependent function $\bar{\kappa}(i)$. By arranging forbidden neighborhoods around already chosen samples with a predefined radius κ, it is obvious that κ does not coincide with the mean, but with the minimum distance between samples. Because the possible distance between samples is a discrete set on a Cartesian grid, it is one possibility to round off $\bar{\kappa}$ to the next possible value on a Cartesian grid, indicated by the symbol $\lfloor\ \rfloor$. This is summarized by the following equation

$$\kappa(i) = \lfloor \bar{\kappa}(i) \rfloor = \left\lfloor \sqrt[n]{\frac{1}{d(i)}} \right\rfloor, \tag{3.10}$$

which describes the location-dependent radius of forbidden neighborhood (Figure 3.6).

Using this strategy alone to generate the Poisson-disk distribution results in distributions with clearly visible steps due to the finite set of possible distances. Therefore, the k-space is segmented into rings. The sdf integrated over these areas gives the number of samples to choose out of this region. The forbidden neighborhood is generated as described before.

For lowering the computational cost, it is essential to choose samples without recline according to the originally described stochastic model. The implementation of the variable-density Poisson-disk generation would otherwise result in prohibitively long computation times due to increasing numbers of repeated trials (N'). Because of that,

Table 3.3: Computation times for sampling-pattern generation. Times include the whole pattern generation and the calculation of the radii κ from a given probability mass function pmf. The time increases for $R \to 1$.

Reduction factor (R)	time [s] for grid size 300×100	time [s] for grid size 200×100
4	1.57	0.84
3	1.68	0.83
2.5	1.83	0.94
2	2.67	1.34
1.5	3.26	1.7
1.4	3.63	1.75
1.3	3.76	1.86
1.2	4.25	1.99
1.1	4.49	2.19

the random choice of samples is not performed on the set of all samples, but on the available set that is updated after each try. The redefined model is only used to calculate the sdf.

3.3.0.2 Computational cost of sampling-pattern generation

The algorithm has been implemented in C and tested for multiple values of the reduction factor R on a 64-bit system with 12 GB RAM and an Intel Xeon processor with 2.67 GHz. The application was designed to run on a single core. The results for a Cartesian grid of size 300×100 and 200×100 are given in Table 3.3. Decreasing the reduction factor R results in higher computation times (for example 4.49 s for a matrix size of 300×100 and $R = 1.1$, see Table 3.3).

3.4 Undersampling in 1D

Although the method is described here for 3D imaging, it is also applicable to 2D imaging. In 2D Cartesian imaging, the frequency direction is fully sampled, and undersampling is performed only on the phase encoding direction. The determination of the sdf from the pmf is unchanged, but the summation over Φ is reduced to a summation in 1D. The Poisson-disk generation can be implemented in the same way, with the difference that the neighborhood is an interval instead of a circle, see Figure 3.7 (a). The C-code implemented for 2D undersampling-patterns is also able to generate the described 1D

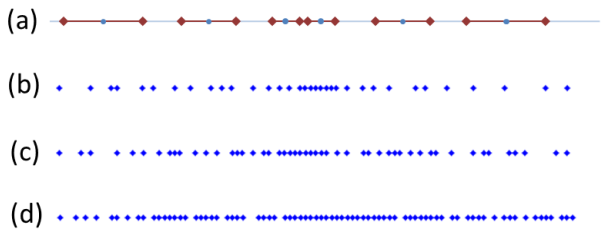

Figure 3.7: Variable-density Poisson-disk sampling-pattern in 1D. Location-dependent forbidden neighborhood (a), indicated by red interval around the samples. Resulting sampling-patterns are given for different undersampling factors $R = \frac{N_t}{N}$: (b) 3, (c) 2, and (d) 1.3.

undersampling-patterns. Examples for generated variable-density sampling-patterns in 1D are given in Figures 3.7 (b-d) for different undersampling factors R.

3.5 Temporal order

The procedure described before can be used to decide, which samples should be acquired. The temporal order of the samples is not determined until now. Acquisition in the same temporal order as the samples were chosen from the set of possible samples is not impossible, but leads to unpredictable results. The distance between subsequent samples could be large, and therefore, result in eddy current induced artifacts or significant contrast change. Because of that, the determination of the final sampling-pattern and the temporal order need to be performed before the actual acquisition.

The best temporal order depends on the MR sequence and the contrast to be achieved. For a signal that is immediately in the steady state and has no fluctuation, the temporal order has no influence. The situation for temporally varying signals is different, because the temporal order influences the contrast as well as the artifact appearance. However, this is out of scope of the considerations here.

In Chapter 4, the temporal order for abdominal T1-weighted dual-echo imaging with incomplete breath-holds is described in detail.

3.6 Initial experiments and results

Among other experiments that were performed to evaluate the sampling, one selective experiment is presented in the following for illustrative purposes. The experiments were performed on a volunteer on a 3T scanner (Ingenia, Philips Healthcare, Best, The Netherlands). An 8-element head-coil was used to acquire multi-slice data of the head with a resolution of $0.9 \times 0.9 \times 1$ mm^3 and a FOV of $280 \times 223 \times 180$ mm^3. A gradient echo sequence with a flip angle of $30°$, and TE/TR of $1.9/25$ ms was chosen. The experiment was performed without acceleration to make retrospective undersampling possible. Different sub-sampling patterns were used retrospectively to evaluate their influence on image quality. Reconstructed images are shown in Figure 3.8 with a detailed view given in Figure 3.9. The images of the whole head (Figure 3.8) are comparable in image quality. Differences are hardly visible in the large volume images obtained for the full sampling (a), completely random sampling (b), uniform Poisson-disk sampling (c), variable-density Poisson-disk sampling, decaying with $(k/\Delta k)^6$ (d), and optimized sampling according to the signal distribution in k-space (e). In the detailed view of the images in Figure 3.9, differences become visible. The largest deviation from the fully sampled data is visible for the random sampling (b), while the image qualities of the reconstructions are similar for the three Poisson-disk distributions with differing sampling density functions. Difference images to the fully sampled image are calculated and shown in Figure 3.10 for the same sampling patterns as in Figures 3.8 and 3.9. Consistent with the latter images, the largest error occurs for the completely random sampling pattern in Figure 3.10 (a). The uniform Poisson-disk sampling (b) reduces the errors, but better results are achieved with the two variable-density Poisson-disk sampling schemes (c,d).

Due to the choice of the reconstruction, the central k-space is fully sampled and used for calibration. This already induces a variable-density for all sampling patterns presented before. The terms uniform, random etc., therefore, are related to the outer part of k-space only.

The experiment presented here was retrospectively undersampled. This enables the calculation of an optimized variable-density according to the actual signal distribution in k-space. This sampling density is very specific to the image and potentially inappropriate for other patients or slightly changed locations, orientations or contrast. In general, the distribution is unknown in advance. Typical distributions can be learned from

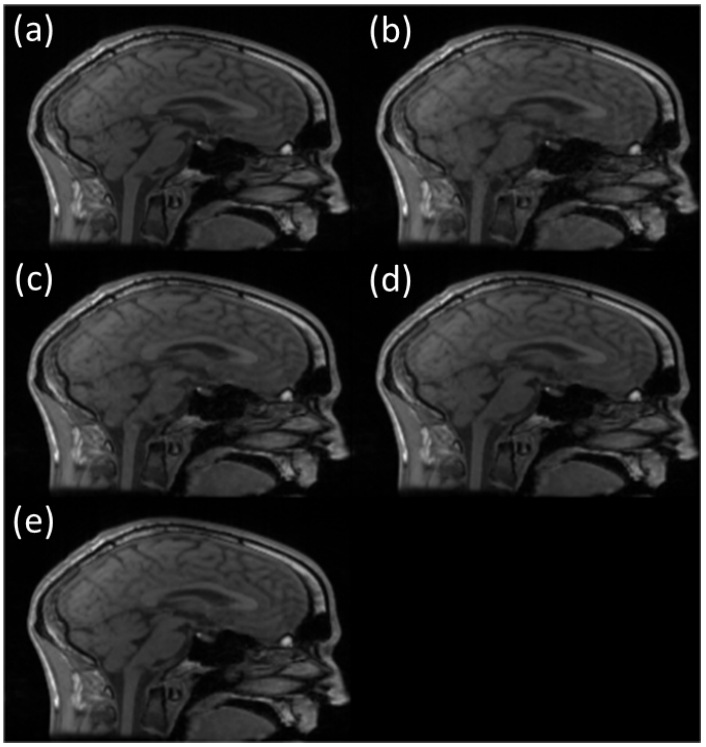

Figure 3.8: Simulation of different sampling-patterns. The fully sampled data is undersampled with the indicated sampling-pattern, each with a reduction factor of $R = 5$, and reconstructed by a combined CS/PI reconstruction (ℓ_1-SPIRiT). For reference the Fourier transformed fully sampled data is given in (a), which is acquired in a 10 minute scan. The reconstructed images of the retrospectively sub-sampled data are shown in (b-e) for different kinds of sub-sampling-patterns. The reconstruction relies on calibration lines, therefore all sampling-patterns have a fully sampled central area in common. The specified sampling refers to the outer part of k-space. (b) is uniform randomly undersampled, while (c) is a uniform Poisson-disk sampling, (d) a variable-density Poisson-disk distribution with a pmf decaying proportional to $(k/\Delta k)^6$, and (e) is optimized according to the signal distribution in k-space.

prior example images, but compared to the procedure described above, the distributions should fulfill some properties, such as radial symmetry, for example. This makes them more robust against small rotations compared to reference. Furthermore, they should be smoothened to cancel out object-specific variations in k-space.

Apart from the usually analyzed MR imaging, there are applications, where the tendency of signal decay towards the periphery is violated. Among others, this is the case for tagging techniques [105]. A series of RF pulses and gradients is applied before the imaging to prepare the magnetization periodically in image space. A periodic 1D or 2D modulation in image space results in replica of the central maximum in outer parts of k-space. In this case, a sampling density that is adapted to the expected signal distribution is clearly advantageous compared to a decay towards the periphery.

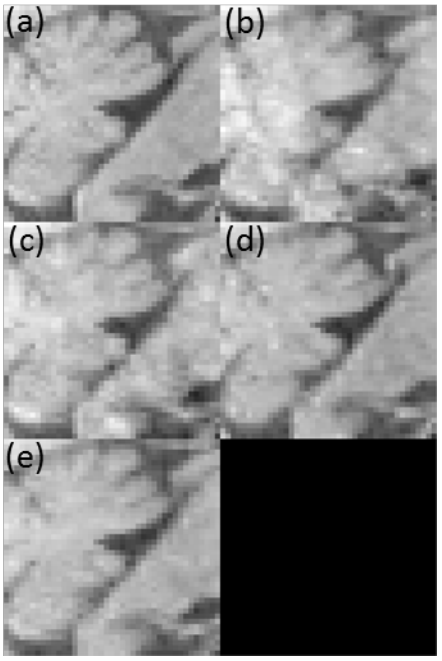

Figure 3.9: Detailed view of the images from Figure 3.8. The image arrangement (a-e) is the same as given in Figure 3.8. Differences are visible in the upper left corner under the letters, as well as in the lower parts of the images. The largest deviation is visible for the random distribution of samples. The two Poisson-disk distributions result in similar image quality.

3.7 Discussion

In this chapter, a fast possibility for generating a quasi-continuous variable density Poisson disk distribution on a Cartesian grid was proposed. As a special case, the algorithm is also able to calculate uniform density Poisson disk distributions. The calculation is fast enough to run on the scanner after setting the experimental parameters.

A possibility was shown to generate a desired variable density by dividing the k-space in rings of desired thickness with constant sampling density inside and a corresponding Poisson disk radius. This radius is specific for the desired variable density function, but also for the wanted total reduction factor, because the sampling density increases with decreasing reduction factor. For this purpose, a method is proposed to derive the sampling density function from the probability density. It is an iterative method that has been shown to have low computation times and is thus clearly advantageous compared to a calculation via Monte-Carlo simulations. It is advantageous for the computational cost and for the quality of the distribution to use an appropriate Poisson disk radius. A Poisson disk radius that is too low for the desired density of samples results in fewer

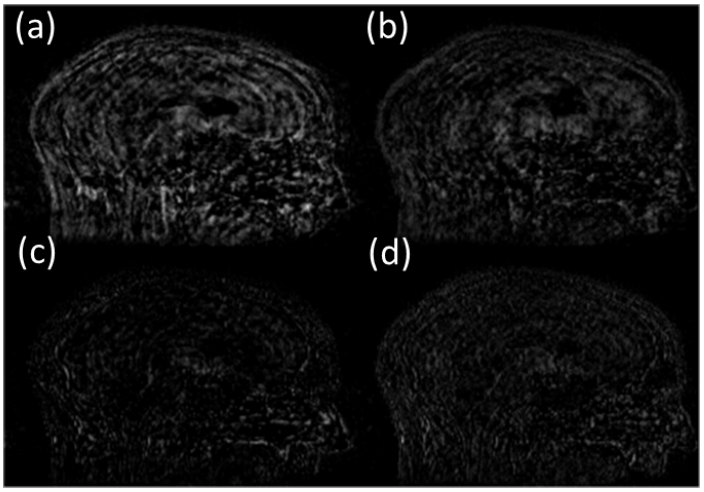

Figure 3.10: Difference images to the fully sampled reference for the simulated different sampling-patterns. Difference images are upscaled by a factor of 7. (a) is from uniform random undersampling, while (b) is from a uniform Poisson-disk sampling, (c) from a variable-density Poisson-disk distribution with a pmf decaying as $(k/\Delta k)^6$, and (d) from a variable-density Poisson-disk distribution with sdf optimized according to signal distribution in k-space.

restrictions to the spread of possible distances between samples and thus to a distribution that becomes more comparable to a pure random distribution. The other extreme is a Poisson disk radius that is chosen too large and produces a distribution with a lower sampling density than desired. To achieve the desired sampling density, the Poisson radius needs to be decreased step by step, a procedure known as relaxation that is computationally intense if the number of iterations is large.

An input for the proposed method is the probability density function that can be chosen freely and is thus able to fulfill any desired variable density function. Sampling patterns generated with this algorithm were tested on different density functions showing clear improvement for the Poisson disk distributions compared with pure random sampling. The pure random distribution of samples frequently leads to a wider spread of realized distances between neighboring profiles. This can be seen in the Voronoi diagrams and clearly leads to a severe loss of information in the images. These distances are restricted by the Poisson disk distribution due to the adequate choice of the forbidden neighborhood. The variable density Poisson disk distributions is slightly improved compared to homogeneous sampling density. The optimum variable density function for combined compressed sensing and parallel imaging needs to be found. The optimum solution is not obvious, because the two methods have potentially conflicting requirements to fulfill. A pure CS reconstruction theoretically shows superior results if the knowledge

about the sparsity of the distinct scales is exploited. This results in variable density with clearly more undersampling in the periphery. A pure PI reconstruction has potentially problems to recover the signal if the reduction factor is lower than a specific value. This value is set by the number of coils and their ability to produce independent images. This is clearly different from the reduction factor in CS that is set by the sparsity of the signal.

The special case for generating a uniform density Poisson disk distribution requires only slight modifications to the algorithm for variable density distributions. The separation of k-space to rings is not necessary for this kind of distribution, because the sampling density is constant on the plane by definition. Furthermore, the sampling density function is uniform and is thus easily calculated. Nevertheless, the calculation as described in Section 3.2.2 also holds for uniform density distributions and is thus kept for convenience in the algorithm for uniform densities. To ensure a good distribution, one relaxation step is recommended that only leads to slightly higher computational cost due to the restricted number of relaxation steps.

Chapter 4

Incomplete breath-holds in abdominal MRI

This chapter is to a large extent based on the full paper ”Robust abdominal imaging with incomplete breath-holds” published in MRM [106].

4.1 Abdominal MRI

Respiratory motion is a common source of artifacts in MRI. Performing the acquisition in a single breath-hold has proven to be an efficient means to minimize such motion artifacts, especially in abdominal imaging. However, the scan time required to cover a large volume with high spatial resolution, as desired in abdominal imaging, often over-strains the breath-holding capabilities of patients, leading to a premature onset of respiratory motion during the acquisition and to an inconsistent dataset. This will be referred to as incomplete breath-hold. The resulting artifacts and their dependence on the acquisition order, i.e. the temporal order, in which the k-space profiles are measured, were studied in [107]. A centric acquisition order that covers the central k-space first, was demonstrated to reduce artifacts. This can be explained by the typical distribution of signal energy in k-space. Inconsistencies in the profiles with higher signal energy from the central k-space result in higher artifact energy. Therefore, it is suggested to collect these profiles first to minimize the risk of respiratory motion during their acquisition.

After the scan, the image quality is often assessed quickly, and if rated inadequate due to artifacts, the scan will be repeated with reduced spatial resolution, in order to adapt

the scan time to the breath-holding capabilities of the particular patient. This procedure obviously complicates the workflow and prolongs the examination. Alternatively, the acquisition may be distributed over multiple breath-holds [108]. This decreases the duration of each breath-hold, but increases the scan time substantially, because the patient needs several breathing cycles between subsequent breath-holds to recover. Moreover, limited repeatability of the breath-hold position may also cause artifacts.

The breath-holding capabilities of a particular patient are unknown in advance and may degrade over multiple breath-holds, rendering the use of a predefined breath-hold duration prone to failure. Performing the acquisition during free-breathing instead is attractive in particular for the examination of very sick or uncooperative subjects [109]. Navigators are employed to determine the breathing position to restrict the acquisition to a certain range of breathing positions, the so-called gating window [110, 111]. However, this approach lowers the scan efficiency dramatically, since k-space profiles are collected in only a fraction of the breathing cycle.

Both breath-holding and free-breathing strategies benefit from various methods for scan acceleration, like PI and CS. This work is focused on single breath-hold abdominal imaging that is favored to achieve a high scan efficiency and motion state consistency. It is aimed at making single breath-hold abdominal imaging more insensitive to incomplete breath-holds to reliably attain high image quality in most patients. PI and CS are jointly applied to cover a large volume with high spatial resolution as fast as possible. A navigator-based detection of the onset of respiration, triggering an automatic scan termination, is suggested to avoid the use of inconsistent data in the reconstruction and thus to suppress artifacts caused by incomplete breath-holds. Two different navigator types are tested. For the first time, an acquisition order is proposed that permits an almost continuous compromise between spatial resolution and undersampling artifacts during the scan and obviates the need for a manual, prospective adaptation of the spatial resolution or coverage to the expected breath-holding capabilities of a particular patient.

In the next section, the design of the sampling pattern and the acquisition order is explained first together with navigator methods for scan termination. Then, an outline of the employed reconstruction is given, and the performed phantom and in-vivo experiments are described. The in-vivo experiments cover 3D T1 weighted gradient echo imaging with and without contrast agent, and dual-contrast imaging within one breath-hold. Finally, the results are summarized and discussed, as are selected aspects of the

new strategy for coping with incomplete breath-holds in single breath-hold abdominal imaging.

4.2 Sampling strategy for incomplete breath-holds

The primary goal in the design of the sampling patterns and the acquisition order is to reconcile the different, possibly conflicting requirements resulting from the individual properties introduced above. These requirements include: (a) increasing spatial resolution over time and full uniform sampling inside a central area for autocalibrated PI, (b) non-uniform sub-sampling outside of the autocalibration area for CS, and (c) variable-density sampling to account for the expected distribution of signal energy. These requirements have to be met in principle throughout the acquisition to facilitate the reconstruction of images from undersampled data collected up to any point in time. Motion artifacts can thus be minimized independently of the actually achieved breath-hold duration by reconstructing from consistent data only. Moreover, these requirements permit enhancing image quality in terms of spatial resolution and undersampling artifacts continuously with the breath-hold duration.

The design of the sampling patterns and the acquisition order is described in detail in the following for 3D Cartesian imaging. The acquisition order reduces to a sequence of k-space profiles in the two phase-encoding directions k_y and k_z, since the k-space is fully sampled along the read-out direction k_x.

4.2.1 Increasing spatial resolution and autocalibration

A commonly used approach is the manual prospective adaptation of the spatial resolution or coverage to reduce the breath-hold duration. Instead, it is proposed to automatically increase the spatial resolution in the two phase-encoding directions gradually during the scan.

The k-space is divided into two parts: a central autocalibration area and the remaining k-space that is denoted as periphery. To support an autocalibration of the sensitivity of multiple receive coils for PI, the central k-space area is fully sampled first. This is typically the most stable period of the breath-hold with the least risk of motion during the acquisition. The number of k-space profiles in this autocalibration area is denoted

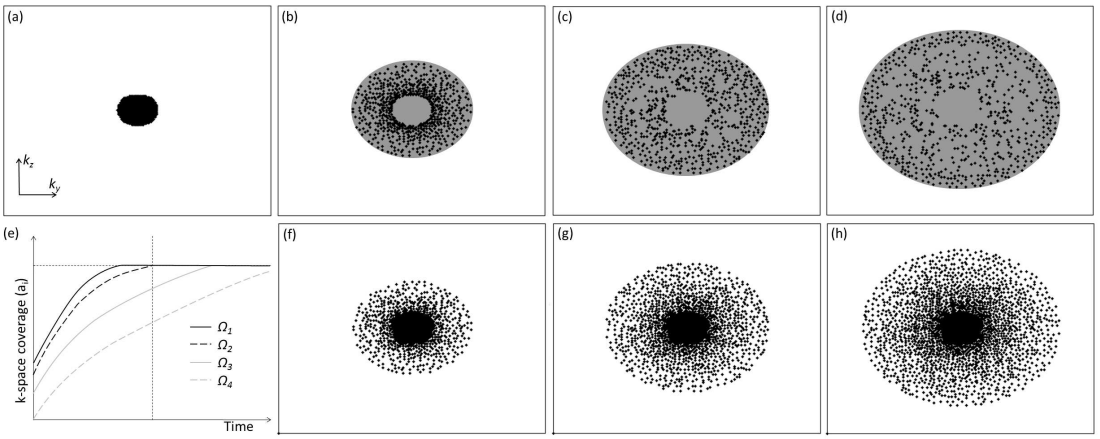

Figure 4.1: Increasing spatial resolution with time. (a) The calibration area sampled fully first. (b) The first section, marked as grey area, and the first fraction, shown as a set of black dots, indicating phase-encoding steps to be measured. (c,d) The second and third section, covering a larger k-space area and thus supporting a higher spatial resolution, and the second and third fraction. (f-h) All phase-encoding steps measured up to the first, second, and third fraction. (e) The maximum $|k|$ is reached at different points in time during the acquisition for different values of Ω. Shown are schematically four graphs with $\Omega_1 > \Omega_2 > \Omega_3 > \Omega_4$. For an increasing value Ω the target $|k|_{\max}$ is reached earlier. The remaining scan time after reaching the target resolution is used to improve SNR and to reduce potential undersampling artifacts by decreasing the reduction factor.

by N_0. The half-axes a_0 and b_0 of the ellipse delimiting this autocalibration area define the first, coarsest spatial resolution level (cf. Figure 4.1(a)).

Typical distributions of the signal energy in MR images have their maxima at the center of k-space and decay towards the periphery [104]. Motion appearing during coverage of the central area, therefore, leads to more severe artifacts than motion appearing during coverage of the peripheral area. Because of that, the center of k-space is acquired first and the coverage of k-space is then successively increased. This approach, described in [107], is extended in this work, to allow for an efficient application of PI and CS and to enable a reconstruction of images from consistent data in case of scan termination due to motion.

The increase of the spatial resolution over time is described by the parameter Ω. It is defined as the inverse of the average sampling density in the covered k-space periphery and related to the temporal increase of the k-space coverage. This user-defined parameter Ω gives an upper limit of the total reduction factor, ensuring that robust reconstruction can be achieved at any breath-hold duration. It thus allows us to trade off between spatial resolution and artifact level during the acquisition. Consequently, the spatial resolution

increases with the breath-hold duration, and the initially larger voxels help in attaining an acceptable SNR and successful reconstruction without undersamplimg artifacts early on. The interpretation of Ω as reduction factor in the periphery is valid until the target resolution is reached. For later times, the reduction factor decreases.

In addition to the parameter Ω, the total reduction factor R is used in the following. R is defined as the reduction factor related to the covered k-space at a given time. As opposed to Ω, a parameter that is defined in the periphery of k-space, the total reduction factor R includes the autocalibration area.

For the generation of the profile order in the periphery, all remaining k-space profiles, apart from the central profiles, ideally to be measured are grouped into fractions. These fractions are acquired sequentially in time. A fraction is a realization of a distribution of N profiles on a section S_i of k-space. Sections are nested sets of k-space profiles, i.e. each subsequent section contains all the previous sections that can be regarded as concentric, elliptically shaped k-space areas, indicated by grey areas in Figure 4.1(b-d). Their half-axes a_i and b_i, $i = 1, 2, 3, \ldots$, determine the subsequent spatial resolution levels. The area of one section multiplied with the density of possible sample locations on a Cartesian grid ρ, which is one per unit area here, gives an estimate of the number of profiles within one section, $N_i \approx \pi a_i b_i \rho$. It has to be ensured that the average reduction factor in the periphery of section i, excluding calibration lines N_0, is Ω

$$\frac{N_i - N_0}{iN} \approx \frac{\pi a_i b_i \rho - N_0}{iN} = \Omega. \tag{4.1}$$

Solving this equation for the product $a_i b_i$ yields

$$a_i b_i = (iN\Omega + N_0)\frac{1}{\pi\rho}. \tag{4.2}$$

Because the ratio

$$\frac{a_i}{b_i} = \frac{a_\mathrm{T}}{b_\mathrm{T}}, \tag{4.3}$$

with $a_\mathrm{T} = \max k_y$ and $b_\mathrm{T} = \max k_z$ corresponding to the target spatial resolution in the k_y and k_z direction, is fixed, the half axis can be written as

$$a_i = \sqrt{(iN\Omega + N_0)\frac{a_\mathrm{T}}{\pi b_\mathrm{T}\rho}}. \tag{4.4}$$

This is a monotonically increasing function, reaching the target resolution corresponding to a_T at some section i that can be calculated by setting $a_i = a_\mathrm{T}$. For larger section numbers i, the half axis $a_i = a_\mathrm{T}$ is fixed. This can be summarized as

$$a_i = \begin{cases} \sqrt{(iN\Omega + N_0)\frac{a_\mathrm{T}}{\pi b_\mathrm{T}\rho}}, & \text{if } i < \frac{\pi a_i b_i \rho - N_0}{N\Omega} \\ a_\mathrm{T}, & \text{otherwise} \end{cases} \tag{4.5}$$

$$b_i = a_i \frac{b_\mathrm{T}}{a_\mathrm{T}}. \tag{4.6}$$

After the target resolution is reached, any remaining time is spent on decreasing the total reduction factor, by increasing the sampling density in k-space according to the non-uniform subsampling described in the next section. The spatial resolution stays fixed, while additional samples result in decreasing reduction factors in the periphery. The temporal evolution of a_i is schematically shown in Figure 4.1(e) for different Ω. The growing half-axes and thus the size of the sections are illustrated in Figure 4.1 on an example, for which $\Omega = 8$ and $N = 347$ were chosen. Each dot in the 2D k-space (two phase-encoding directions) represents a measured profile. Added profiles from one fraction each are indicated in Figure 4.1(a-d). As opposed to this, Figure 4.1(f-h) show the accumulated fractions, representing the resulting sampling patterns. The selection of these profiles for each fraction is explained next.

4.2.2 Non-uniform variable-density Poisson-disk sampling

The sampling patterns have to permit autocalibrated PI and have to lead to incoherent aliasing to support CS. This is achieved with a fully sampled auto-calibration area in the center of k-space and a Poisson-disk distribution [23, 31] in the periphery.

The process of generating a Poisson-disk distribution has already been described in Chapter 3 for a fixed reduction factor that is determined before the scan starts. The difference for the adaptive sampling patterns with unknown reduction factor in advance is the temporally changing subset S that is increasing with time. This corresponds to improving spatial resolution as time passes by.

The elliptically shaped central k-space area is fully sampled, and thus also captures the highest signal energy. In the peripheral k-space, the sampling density should decay as

a function of the distance to the k-space center. This is achievable with a varying minimum distance r_{min} of profiles in k-space. The variation can be a discrete distribution with constant values within specific regions or it can be made approximately continuous, an approach that was chosen in this chapter. Basically, a quadratic decay of the sampling density was used. This is an improvement compared with uniform sampling density. The resulting condition for the minimum distance r_{min} is briefly described in the following. Every profile in k-space with coordinates (k_y, k_z) can be uniquely assigned to an ellipse with fixed half-axes (a, b) that fulfill $a/b = a_{\text{T}}/b_T$. The same r_{min} is assigned to all points on the ellipse (a, b). A linear function in the half-axis a is assumed

$$r_{\text{min}} = ma + c = m\sqrt{k_y^2 + \left(k_z \frac{a_{\text{T}}}{b_{\text{T}}}\right)^2} + c. \tag{4.7}$$

The parameters m and c are determined by the constraints $r_{\text{min}}(\frac{a_i - a_0}{2}) = \bar{r}$ and $r_{\text{min}}(a_0) = \frac{\bar{r}}{2}$, with $\bar{r}$ being the average distance between samples for a given Ω, leading to

$$m = \frac{\bar{r}}{a_i - 3a_0} \tag{4.8}$$

$$c = \bar{r}\frac{a_i - 5a_0}{2(a_i - 3a_0)}. \tag{4.9}$$

Because there is only a discrete set of possible distances between profiles on a Cartesian grid, the initial value of $\bar{r}$ is the largest possible distance smaller than $\sqrt{\Omega}$. If the set of possible samples P is empty, $\bar{r}$ is changed to the next possible lower value. This procedure is known as relaxation and has been explained in more detail in Chapter 3. Updates of the variable $\bar{r}$ can occur at any time if P is empty, but are required at the latest when the target resolution is reached, because the remaining breath-hold duration is used to decrease the overall reduction factor. The additional samples keep approximating a Poisson-disk distribution of profiles with increased sampling density that corresponds to decreased minimum distance between samples.

4.2.3 Acquisition order

The process of assigning profiles to fractions was described in the last sections, but the acquisition time-order of profiles in the fractions has been unaddressed and is therefore discussed in the following. It can potentially be selected freely in this method, thus permitting an optimization of the trajectory in (k_y, k_z)-space.

To reduce eddy-current-induced artifacts, the distances between subsequent profiles can be minimized, for instance. In this work, a different approach is used. To describe the profile ordering scheme it is obvious to represent profiles in polar coordinates. The origin of this coordinate system is the k-space center and the radial axis points along the first phase-encoding direction k_y.

The profiles from one fraction are traversed sequentially in time according to their angles in polar coordinates from lowest values to highest. This enforces an upper bound on the distance between subsequent samples and can be calculated with low computational cost. However, this is not the optimal solution regarding eddy currents induced in the object. Other possibilities are solving the traveling salesman problem for the set of samples from one fraction. This approach is computationally clearly more intense and thus disadvantages for computation on the scanner. Furthermore, the time to $k = 0$ is not easy to predict for this solution and thus not applicable to imaging with contrast agents. A different approach is traversing the profiles in a quasi linear manner that is also computationally efficient.

4.3 Motion sensors

In parallel to the data acquisition, the breath-hold has to be monitored. Therefore, independent of the fractions, motion detection is performed using a navigator interleaved with data acquisition after a fixed number of acquired profiles. Depending on the motion state, sensed by the navigator, scan termination could be enforced. Because of that, it is not guaranteed that the last fraction is complete after scan termination. For a low number of profiles within one fraction, this potential asymmetry in k-space sampling will not have a substantial influence on the reconstruction and the resulting image quality. For motion detection, external sensors, like belts or cameras, or internal MR-based sensors, like the pencil-beam [112, 113] or other kind of navigators, can be used. In this work, two different kind of navigators were tested in combination with the adaptive sampling patterns. First, a pencil-beam navigator, performing a kind of 1D imaging in a small cylindrical volume to estimate the position of the diaphragm, and second a $k = 0$ navigator that repeatedly acquires the k-space center and calculates the correlation between the profiles to estimate consistency, have been used.

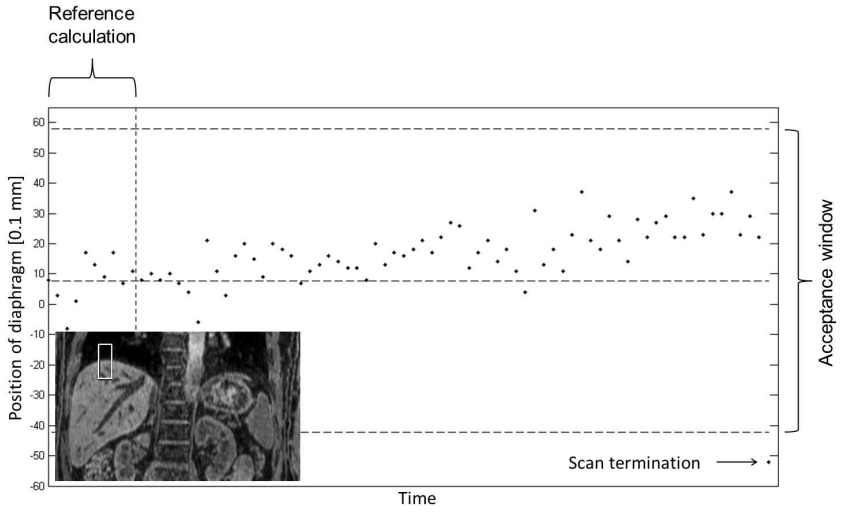

Figure 4.2: Navigator signal used for automatic scan termination. The location of the 1D pencil-beam navigator is schematically shown in the inlay. A typical navigator displacement signal obtained from a correlation with a reference signal is shown. A slight drift during breath-hold is visible. The first averaged navigator positions are used as reference (dotted line). An acceptance window of 10mm width around the reference position is used as termination criterion. The navigator indicating breathing onset in this case is marked with an arrow.

4.3.1 1D pencil-beam

The 1D pencil-beam navigator is an internal MR-based sensor that is part of the scanner software. In clinical practice, it is used in gated acquisitions of the abdomen or the heart, for example. It is manually placed on the diaphragm, based on a survey scan. A 1D imaging volume oriented along the feet-head direction is planned to cover part of the lungs and the liver. Excitation and read-out is performed on this volume (c.f. Figure 4.2). In image space, the contrast between the liver and the lungs changes dramatically and can therefore be detected easily by an edge finding algorithm. The evaluation of the signal is performed in real-time, to decide for the next shot if data acquisition should be performed. In this work, the navigator signal is used to monitor the breath-hold. Therefore, a termination criterion is implemented in the software that stops the TFE acquisition if deviations larger than a predefined value occur. The navigator is acquired after one shot of a TFE train. This corresponds to an update rate of approximately $1/500$ ms. An example for a navigator signal is given in Figure 4.2. The evaluation of the signal is stable and reliable. However, the application of such a navigator to the spin system interrupts the imaging sequence. This can cause signal variation due to steady state perturbations. Furthermore, the spatially selective excitation can lead to saturation artifacts in the image if the flip angle is chosen too high.

This is disadvantageous, because the navigator is placed on the region of interest (ROI) for liver examinations. Additionally, the 1D pencil-beam navigator lengthens the scan time or reduces scan efficiency, because of the long navigator acquisition duration of approximately $20 - 30$ ms. For the purposes of this thesis, the pencil-beam navigator gives more information than what is actually needed. Instead of the actual displacement of the diaphragm, an indication of breath-holding or breathing on-set would be sufficient.

4.3.2 k=0 Navigator

The $k = 0$ navigator uses the imaging sequence itself to monitor the breath-hold. It repeatedly measures the central k-space profile $\boldsymbol{f}_j$ at equidistant times j ensuring a fixed update rate. If the patient starts breathing, the signal changes and the similarity of $\boldsymbol{f}_j$ before breathing onset and $\boldsymbol{f}_k$ after breathing onset reduces. The acquisition takes only one repetition time that is typically in the order of $3 - 6$ms for a dual-gradient-echo acquisition. Because motion significantly changes the phase of k-space data in MR imaging, the complex signal is used for evaluation [114]. The magnitude of the complex correlation coefficient between the reference $\boldsymbol{f}_r$ and subsequent profiles $\boldsymbol{f}_j$

$$c(\boldsymbol{f}_r, \boldsymbol{f}_j) = \frac{\mathrm{cov}(\boldsymbol{f}_r, \boldsymbol{f}_j)}{\sqrt{\mathrm{cov}(\boldsymbol{f}_r, \boldsymbol{f}_r)\mathrm{cov}(\boldsymbol{f}_j, \boldsymbol{f}_j)}} \tag{4.10}$$

is calculated. The covariance is defined as

$$\mathrm{cov}(\boldsymbol{f}_i, \boldsymbol{f}_j) = \frac{1}{N-1}\langle \boldsymbol{f}_i - \bar{\boldsymbol{f}}_i, \boldsymbol{f}_j - \bar{\boldsymbol{f}}_j \rangle \tag{4.11}$$

with the scalar product $\langle \boldsymbol{a}, \boldsymbol{b} \rangle$ of the vectors $\boldsymbol{a}$ and $\boldsymbol{b}$. This method is not able to give an absolute value for the position or the displacement of the diaphragm. It is only a measure of the similarity of subsequent profiles.

One approach to set the reference profile in (4.10) is to choose

$$\boldsymbol{f}_r = \boldsymbol{f}_1. \tag{4.12}$$

This choice for the reference profile is applicable to signals in steady state.

The similarity between navigator profiles is not only influenced by motion, but also by

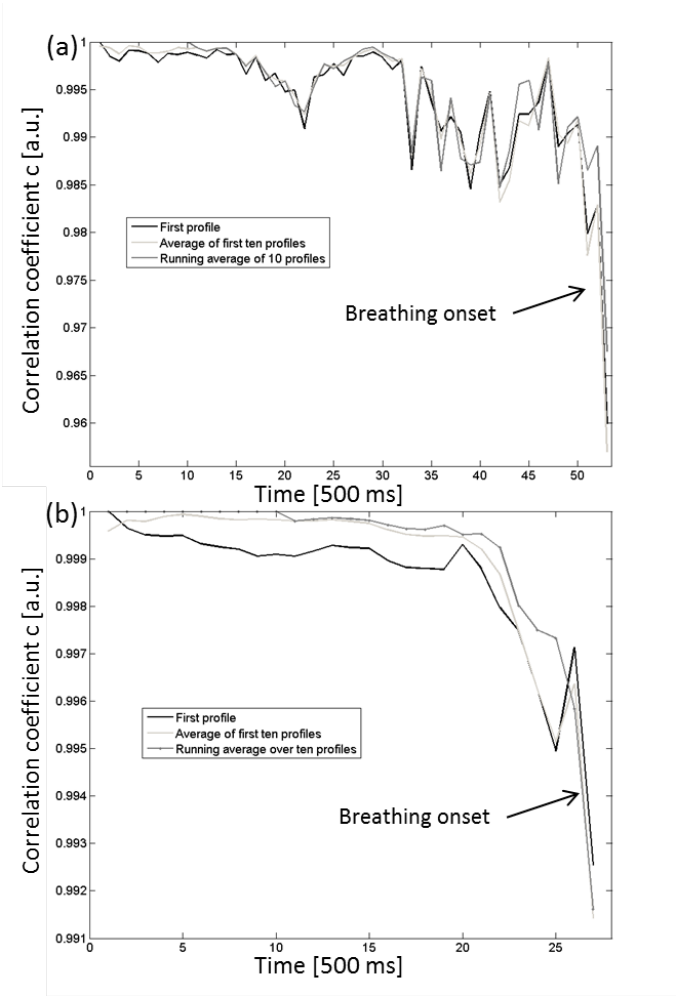

Figure 4.3: Correlation coefficient calculated from k=0 navigator signal for two experienced volunteers from experiments performed in the research laboratories Hamburg. Three different investigated approaches for the reference profile were tested that gave the same time for breathing onset in the volunteers. One approach is to take the first profile as reference profile, the second approach is to take the average of the first ten navigators as reference if the first profile is not reliable. The last investigated method is to take the running average as reference profile. Slight drift in the signal (b) with unknown source is partly suppressed by the running average as reference profile compared with the other two possibilities to choose the reference profile.

signals in transient state or and by contrast agent injection. These changes can be misinterpreted as motion. For signal changes that are much slower than breathing motion, the reference profile can be set to

$$\boldsymbol{f}_r = \frac{1}{j-1}\sum_{i=1}^{j-1}\boldsymbol{f}_i \tag{4.13}$$

or alternatively to

$$\boldsymbol{f}_r = \frac{1}{k-1} \sum_{i=j-k}^{j-1} \boldsymbol{f}_i. \tag{4.14}$$

Equation (4.14) is a running average over k-profiles that adapts to low-frequency changes of the signal, like changes due to contrast agent injection. Equations (4.13) and (4.14) are only examples for the choice of the reference profile that aim at distinguishing between signal changes due to respiratory motion and due to other sources. Different methods to perform the separation based on specific properties are conceivable and are desired to be able to use the $k = 0$ navigator for a specific application.

Apart from this restriction to a limited number of applications, the $k = 0$ navigator has one major advantage. Because the imaging sequence itself is used to acquire the navigator signal, it is not interrupted and the steady-state is therefore maintained. Any saturation effects, as known from pencil-beam navigators, are avoided on top.

In the experiments performed in this work, different reference profiles were used. For

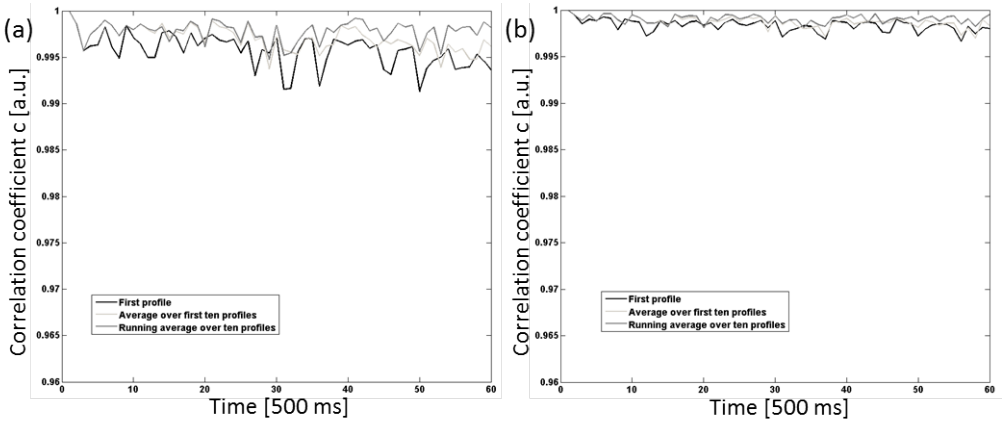

Figure 4.4: Correlation coefficients obtained from clinical DCE imaging, acquired at the UTSW Dallas. Navigator signal evaluated for a patient before contrast injection (a) and post contrast injection (b) during equilibrium phase. The correlation coefficients are consistently higher after contrast injection due to increased SNR. Slight drifts in the signal are suppressed by the running average reference compared with the first profile and the average over the first ten profiles used as reference. Breathing instructions are different at the UTSW Dallas compared with the experiments performed in Hamburg.

the experiments described in Section 4.5.2 the pencil-beam navigator and the k=0 navigator with the reference profile defined in (4.12) were used. The breathing onset was in all cases easily detected and examples are shown in Figure 4.3 for two examinations on two volunteers and different approaches to evaluate the navigator signal.

The breathing onset is clearly visible as a sudden decrease in the correlation coefficient. The different approaches for choosing the reference profile give the same time of breathing onset with slightly higher values of the correlation coefficient for the running average. This is because the running average is insensitive to slow drifts. These drifts can be caused either by motion of the diaphragm or by general signal variation.

The choice of the reference is harder for DCE experiments because the signal is intentionally temporally varying. The experiments in Section 4.5.3 contain pre-contrast and only one post-contrast (equilibrium) phase with minor signal change. The evaluation of the navigator is most complicated for the arterial phase because the largest signal variation occurs at this time. This case is not covered in this work. An example a for navigator signal obtained in a patient with contrast injection is shown in Figure 4.4. The navigator signal was acquired during the examination but intentionally not used for scan termination, because erroneously interruption of the scan had to be prevented. The scan was terminated after a fixed scan duration and the data were retrospectively truncated to the desired breath-hold duration. The navigator signal was evaluated retrospectively and evaluated with the reference profiles given Equations 4.12,4.13, and 4.14 in these cases and an example is shown in 4.4. The end of signal in Figure 4.4 does not correspond to breathing onset as in Figure 4.3, the patients held the breath during the scan and the scan was terminated at the predefined reduction factor.

The equilibrium phase is a phase with only slight signal change due to contrast washout. Therefore, the navigator behavior is not completely different for the two temporal phases. The right and left images are scaled to show the same interval as in Figure 4.3(b). It can be seen that the correlation coefficient of the k=0 navigator is higher for the post-contrast scan compared with the pre-contrast scan. This was observed in all patients and is most probably caused by the improved SNR due to the contrast agent injection. Compared with experienced volunteers, breathing instructions are different in a clinical environment and hard to follow for patients. This hampers the evaluation of the k=0 navigator signal further in a few cases, because the patient did not necessarily start the breath-hold at the same time the scan started. The k=0 navigator with the first profile as reference indicates a slight drift that is corrected by the running-average reference as expected. It depends on the purpose whether a slight drift of the diaphragm should be accepted or not. However, contrast injection potentially results in drift of the correlation coefficient due to contrast wash-in and wash-out as well and is thus hard to distinguish from diaphragm drift.

4.4 Reconstruction

The acquisition is stopped at the onset of breathing, and therefore, motion-free data are used for reconstruction. This prevents motion artifacts, but implies an incomplete dataset. To eliminate aliasing artifacts, a CS-PI reconstruction is applied that deals with the potential missing data problem. The image reconstruction is performed with ℓ_1-SPIRiT [51]. This reconstruction combines compressed sensing and parallel imaging based on auto-calibration. As described in [24], ℓ_1-SPIRiT solves the constrained minimization problem containing the sparsifying transform $\mathbf{\Psi}$, in this case a wavelet transform using Daubechies 4 wavelets,

$$\min_{\boldsymbol{\rho}} \quad \text{Joint}\,\ell_1(\mathbf{\Psi}\boldsymbol{\rho}) \tag{4.15}$$

$$s.t. \quad \mathbf{D}\mathbf{F}\boldsymbol{\rho} = \boldsymbol{f}|_{\text{acq}} \tag{4.16}$$

$$\mathbf{G}\boldsymbol{f} = \boldsymbol{f} \tag{4.17}$$

via a Projections Onto Convex Sets (POCS) algorithm. In this notation, $f|_{\text{acq}}$ are the acquired data in k-space, ρ is the image to be reconstructed, $\mathbf{F}$ is the Fourier transform operator, and $\mathbf{D}$ is the operator that selects the acquired data in k-space. The Jointℓ_1-norm is a combined ℓ_1/ℓ_2-norm, defined by

$$\text{Joint}\,\ell_1(\mathbf{b}) = \sum_r \sqrt{\sum_i |b_{ir}|^2}, \tag{4.18}$$

where i is the channel index and r is the position index of the wavelet coefficient. The joint sparsity takes into account that images from different coils have large coefficients at the same spatial positions. The first constraint enforces data consistency. The second constraint that can also be written as

$$f_i = \sum_{j=1}^{N_c} \mathbf{g}_{ij} * f_j \tag{4.19}$$

enforces calibration consistency with i, j being the channel indices and N_c being the total number of channels. The operator $\mathbf{G}$ performs convolutions with the appropriate convolution kernels $\mathbf{g}_{ij}$. These calibration kernels are estimated from the fully sampled central k-space profiles.

4.5 Experiments and results

4.5.1 Phantom simulation

The proposed sampling patterns depend on the user-defined parameter Ω that determines the trade-off between undersampling artifacts, spatial resolution, and noise level. For the evaluation of the influence of Ω on the reconstructed images as well as for a validation of the increasing spatial resolution with scan time, simulations were performed on a fully sampled 3D dataset acquired on a resolution phantom with the proposed sampling pattern.

The sizes of the in-plane structures in this phantom were in a range of $[0.5\text{mm}; 2\text{mm}]$. The target spatial resolution of the acquisition was $0.75 \times 0.75 \times 3\text{mm}^3$ in a FOV of $240 \times 240 \times 150\text{mm}^3$. The data were acquired with the proposed sampling pattern. For the investigation of the breath-hold duration on the imaging procedure, the data

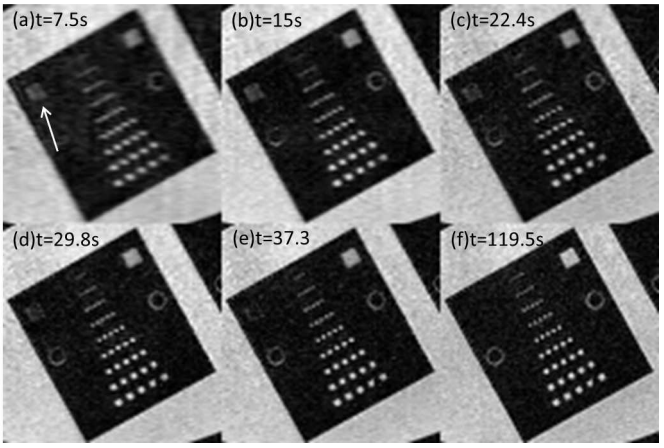

Figure 4.5: Simulation of different 'breath-hold' durations. A 3D phantom dataset was retrospectively undersampled using the proposed sampling pattern and a fixed Ω of 5. Different number of profiles were included in the reconstruction, simulating scan durations as indicated in (a-f). The total reduction factor and the spatial resolution are changing with the 'breath-hold' duration. Corresponding values (number of profiles / total reduction factor R / spatial resolution percentage) are given in the following: (a) $1000/4.1/51$, (b) $2000/4.6/78$, (c) $3000/4.7/94$, (d) $4000/4.0/100$, (e) $5000/3.2/100$, and (f) $20480/1.0/100$. The shown results are zoomed areas of slices from the resolution section of a phantom. A subsection of the fully sampled dataset is shown in (f) for comparison. For increasing number of samples, the image quality improves in terms of resolution and noise.

were retrospectively undersampled with the proposed sampling pattern using different number of samples to systematically evaluate the influence of the scan time on image

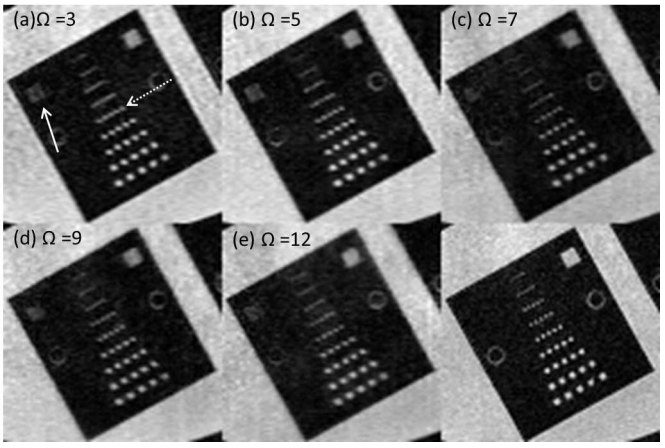

Figure 4.6: Simulation of different values of the parameter Ω. A 3D phantom dataset was retrospectively undersampled, using the proposed sampling pattern and a fixed amount of data (2000 profiles). The chosen values for the parameter Ω are indicated in the images, resulting in different total reduction factors and spatial resolution. Corresponding values (total reduction factor R / spatial resolution percentage) are given in the following: (a) $2.83/61$, (b) $4.58/78$, (c) $6.42/91$, (d) $7.92/100$, and (e) $7.92/100$. The shown results are enlargements of the resolution section of the phantom. The result for full sampling is shown in (f) for comparison. The achieved spatial resolution depends on the chosen Ω and on the reconstruction and improves from (a-c) (see dotted arrow for in-plane and full arrow for through-plane resolution). On the other hand, images with large values of Ω (d,e) suffer from image artifacts and increased noise. This restricts the range of acceptable values of Ω.

quality. According to (4.5), the spatial resolution should increase with time. The image quality is not only dependent on the resolution, but also on the undersampling that can lead to noise amplification.

Results from simulations using a fixed Ω of 5 are shown in Figure 4.5 for increasing number of samples. These results mimic measurements terminated at varying scan progress, with scan durations indicated in the images. As expected, the resolution in AP direction (in-plane), the through-plane resolution, and the SNR improve with growing number of samples. The read-out direction points from left to right and therefore, the resolution in this direction stays fixed. The improved in-plane resolution can be deduced from reduced blurring for increasing number of samples as well as from the structures in the resolution phantom. The improved through-plane resolution becomes obvious when comparing results with the fully sampled reference dataset in Figure 4.5(f). In the upper left corner, a high intensity square (see arrow in Figure 4.5(a)), from a neighboring slice appears in the undersampled data that is absent in the original image. The reduced intensity for increasing number of samples reflects the improved through-plane resolution.

Further simulations on this phantom dataset were performed for different values of Ω while keeping the total number of samples used in the reconstruction fixed. This corresponds to a fixed breath-hold duration and is indicated by the dotted vertical line in Figure 4.1(e). The covered k-space area is determined by (4.5), promising increasing spatial resolution with increasing Ω.

The parameter Ω is important for the generation of the proposed sampling patterns because it determines the velocity that is used to cover k-space over time, affects the undersampling artifacts prior reconstruction, and the SNR at the same time. Reconstruction results from the same phantom dataset are shown in Figure 4.6. It was retrospectively undersampled for different values of Ω and a fixed value of samples $N = 2000$ that corresponds to a fixed scan duration. The values of Ω are indicated in the images. It can be seen in Figure 4.6(a-c) that the in-plane as well as the through-plane resolution increases. The increased in-plane resolution is visible in the line marked with the dotted arrow. In Figure 4.6(a), it appears as a line, whereas it appears as a set of dots in Figure 4.6(c). The tendency of improved through-plane resolution is also visible in the left corner (see full arrow), where a neighboring slice becomes visible in the undersampled data. The intensity becomes lower in Figure 4.6(c) compared with Figure 4.6(a). For higher Ω, resulting images are shown in Figures 4.6(d,e), image quality is starting to degrade by a higher noise level, because the sampling density is too low in the periphery.

4.5.2 3D T1-weighted gradient-echo imaging without contrast agent

Experiments on 8 healthy volunteers, age 30-54, were performed on a 1.5 T scanner (Philips Healthcare, Best, The Netherlands) with a 3D T1-weighted spoiled dual-gradient-echo sequence, for water-fat separation using a two-point Dixon method (mDIXON [97]), employing a 16-element torso coil. The used mDIXON algorithm enables a flexible choice of the echo times and thus eases sequence design. The flip angle was 15°, $\mathrm{TE}_1/\mathrm{TE}_2/\mathrm{TR}$ were $1.3/2.3/3.7$ ms, and the echoes were acquired using bipolar gradients with a pixel bandwidth of 1322 Hz, the FOV was about $375 \times 240 \times 230$ mm^3, and the target actual spatial resolution was $1.5 \times 1.5 \times 3$ mm^3, covering the whole liver.

The implementation of the adaptive PD sampling-pattern generation is fast enough to enable its execution directly on the scanner during protocol specification. This simplifies workflow, especially for in-vivo imaging. For imaging on volunteers, the number of

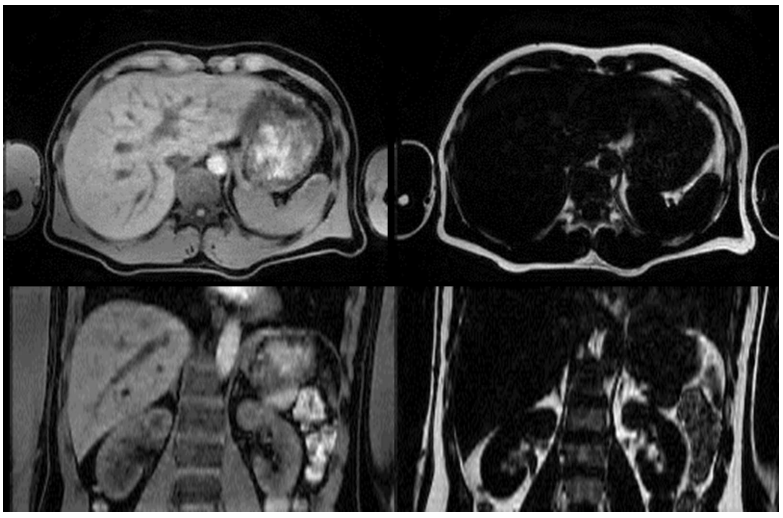

Figure 4.7: Results in a volunteer from a scan with $16s$ breath-hold duration. This corresponds to a total reduction factor of $R = 4.14$ related to the achieved k-space coverage $|k|_{\max}$ at scan termination. Example slices of water and fat images in the axial and the reformatted coronal plane are shown. Images indicate good image quality and 3D coverage without motion artifacts.

fractions was $40 - 50$, and $\Omega = 8$ was chosen. The measurements were complemented by an interleaved 1D pencil-beam navigator acquisition to detect the onset of respiration. The reference breath-hold position was derived from the first diaphragm positions of the breath-hold. The navigator was measured interleaved every $200 - 500$ ms using a flip angle of 15° for low interference with the magnetization in the target volume. An acceptance window with a width of 10 mm around the reference position was chosen. During breath-holding, the position of the diaphragm only changes little with a slight drift. The first navigator after onset of breathing causes scan termination approximately half a second later. The profiles acquired in this period were also used for reconstruction. The alternative k=0 navigator was used for scan termination as well with the reference profile given by (4.12).

The reconstruction has been performed off-line so far. To accelerate the reconstruction, a coil compression technique [22] was used before ℓ_1-SPIRiT [51]. The signals from the 16 channel coil were reduced to six virtual channels without significant information loss. The compressed signal was then used as an input for the CS-PI reconstruction (included in the available freeware[1]) that is written in C++ supporting multiple cores of CPUs or GPUs. In this work, a 64-bit Linux system with 4 CPUs (Dual-Core AMD Opteron 2220) was used resulting in reconstruction times in the order of 4-5 min for one echo. The reconstruction times of this kind of algorithm for multiple CPUs and GPUs

[1] http://www.eecs.berkeley.edu/∼mlustig/Software.html

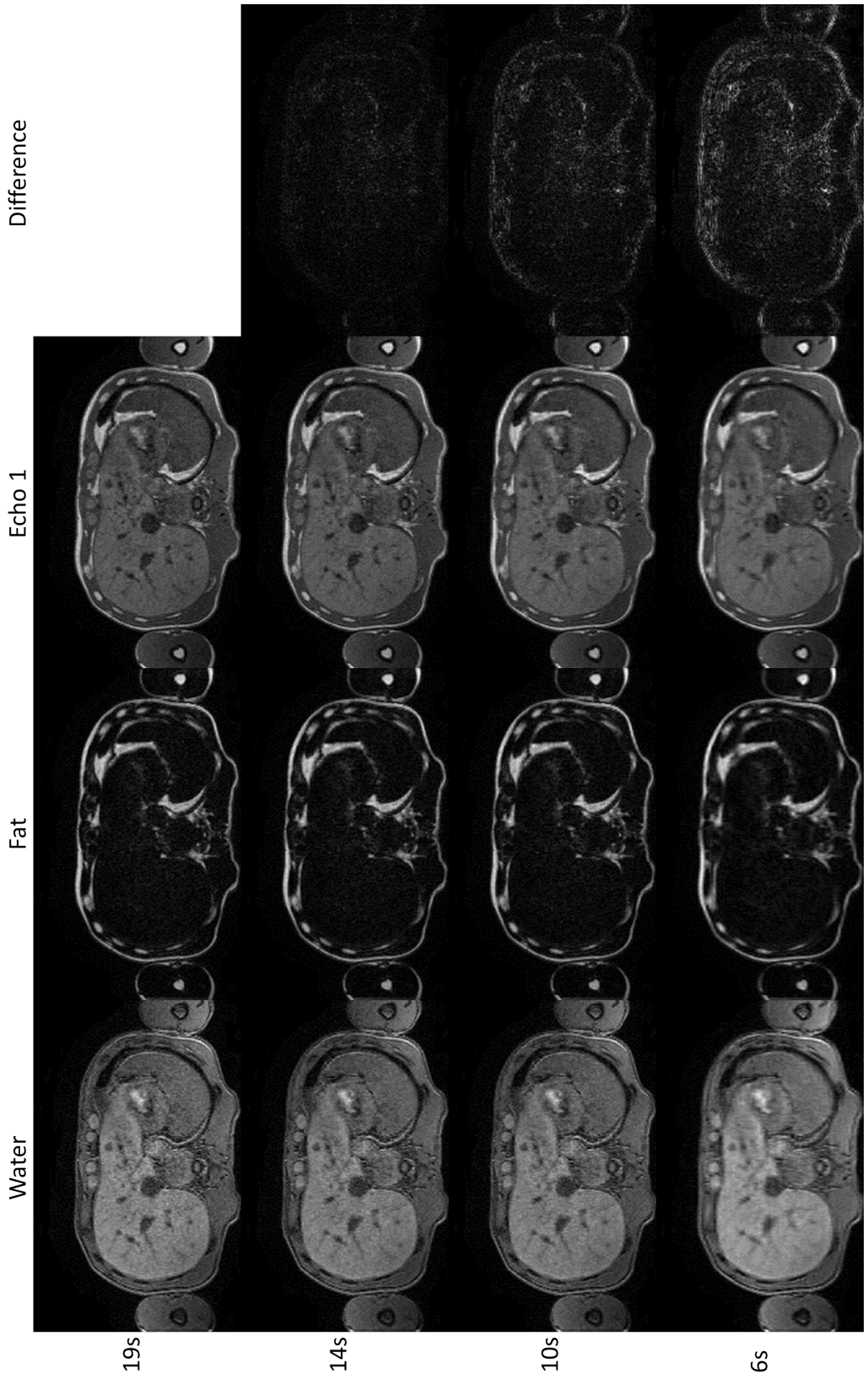

Figure 4.8: Influence of breath-hold duration on image quality. The underlying measurement was automatically stopped after 19 s at breathing onset. For a comparison without misregistration artifacts data were retrospectively discarded to simulate shorter breath-hold durations of $14s$, $10s$ and $6s$. Images of a selected slice of the 3D datasets are shown. The water- and fat-only image, the first echo image and the difference of this image to the first echo image obtained with the 19 s breath-hold, upscaled by a factor of three, are shown. A lower spatial resolution, both in-plane and through-plane, becomes apparent for shorter breath-hold durations.

were studied in detail by Murphy et al. [25]. The resulting images from the individual coils were combined using a Roemer [13] reconstruction to obtain one complex-valued image for each of the two echoes. To these two echo images, an mDIXON [97] separation step was optionally applied, resulting in one water and one fat image. Feasibility was shown on eight different volunteers for different breath-hold durations yielding good image quality. Representative reconstructed images from a scan with flexible scan termination after 16 s, which is a moderate breath-hold duration, are shown in Figure 4.7. The reformatted water and fat images in the axial and coronal plane show good image quality without artifacts from respiratory motion.

One of the in vivo datasets was further analysed by retrospectively simulating shorter breath-hold durations. This allows for a comparison without misregistration artifacts from multiple breath-holds. The measurement underlying Figure 4.8 was automatically

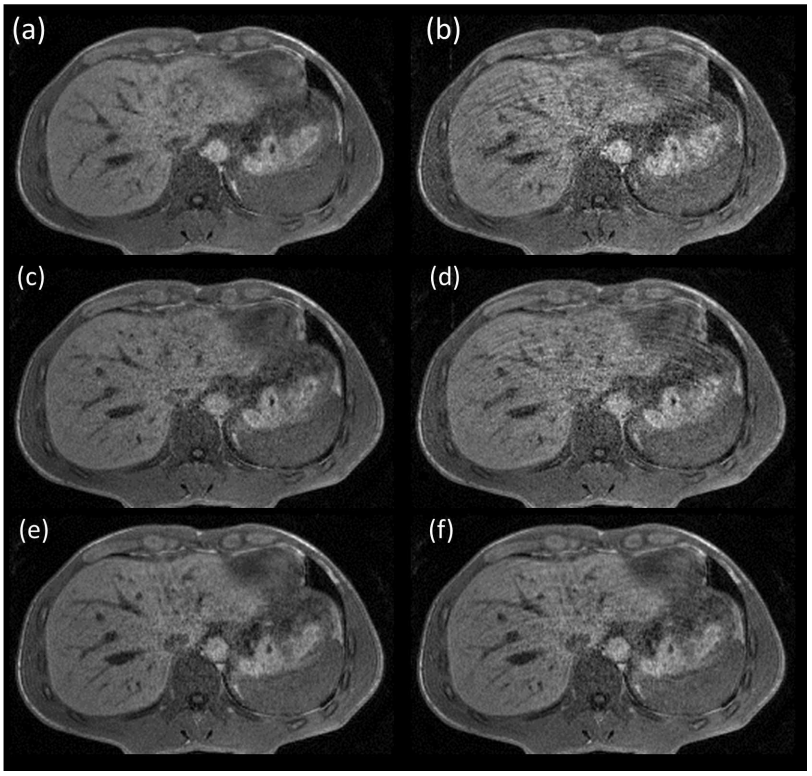

Figure 4.9: Motion artifact suppression by scan termination. Reconstructed images from the first echo of a dual echo acquisition for three individual scans using the proposed sampling patterns with a total duration of 20 s ($R = 2.8$) without self-termination and incomplete breath-holds of (a,b) 12 s ($R = 4.5$), (c,d) 15 s ($R = 3.8$), and (e,f) 18 s ($R = 3.1$) duration. (a,c,e) are reconstructed from data acquired before onset of breathing, (b,d,f) from all data acquired in the first 20 s while the reconstruction parameters were kept the same in all cases. Motion artifacts are clearly visible in (b,d,f), significantly degrading image quality.

stopped at the onset of breathing after 19 s. For comparison, shorter breath holding

was simulated by retrospectively skipping data. Towards shorter acquisition times, the spatial resolution of the single echo images is reduced in the two phase-encoding directions that are anterior-posterior and feet-head. The lowered resolution is transferred to the water and fat images. Dual-echo acquisitions were performed resulting in improved SNR for the water-fat separation compared to fat suppression techniques performed during acquisition. The corresponding difference images of the first echo in the fourth column, upscaled by a factor of three, demonstrate once again the loss of in-plane and through-plane resolution for shorter breath-holds. Difference images of the water and fat images were calculated as well, showing similar result.

To illustrate the effectiveness of motion suppression with the proposed method, a series of experiments on one volunteer with different breath-hold durations was additionally performed. The scans were terminated after a fixed duration of 20 s. Reconstruction is performed from data acquired only before onset of breathing and from all acquired data.

Reconstructed images of the first echo from a dual-echo acquisition with a scan duration of 20 s are shown in Figure 4.9. The volunteer started breathing already after (a,b) 12 s, (c,d) 15 s, and (e,f) 18 s respectively. Figures 4.9(a,c,e) show images reconstructed from data acquired before breathing onset, while Figures 4.9(b,d,f) show images reconstructed from all acquired data. Although the data are acquired with the proposed sampling patterns that are already less sensitive to motion, (b,d,f) are degraded by severe motion artifacts. As opposed to this, no motion artifacts are visible in (a,c,e) from the same data, because they were reconstructed only from the consistent part of the data.

4.5.3 3D T1-weighted gradient-echo imaging with contrast agent

Image quality in clinical dynamic contrast enhanced (DCE) MRI of the abdomen is often challenged by respiratory motion artifacts. DCE studies are commonly acquired at the end of the MRI examination, after the patient has gone through several breath-holds and the average breath-hold capability is known. However, patients may have trouble holding their breath after contrast injection [115] and this is often unpredictable as many of them may have been able to do so earlier in the examination.

The temporal order of an abdominal T_1 weighted dynamic imaging study is schematically shown in Figure 4.10. Typically, in a standard protocol, a series of 3D abdominal

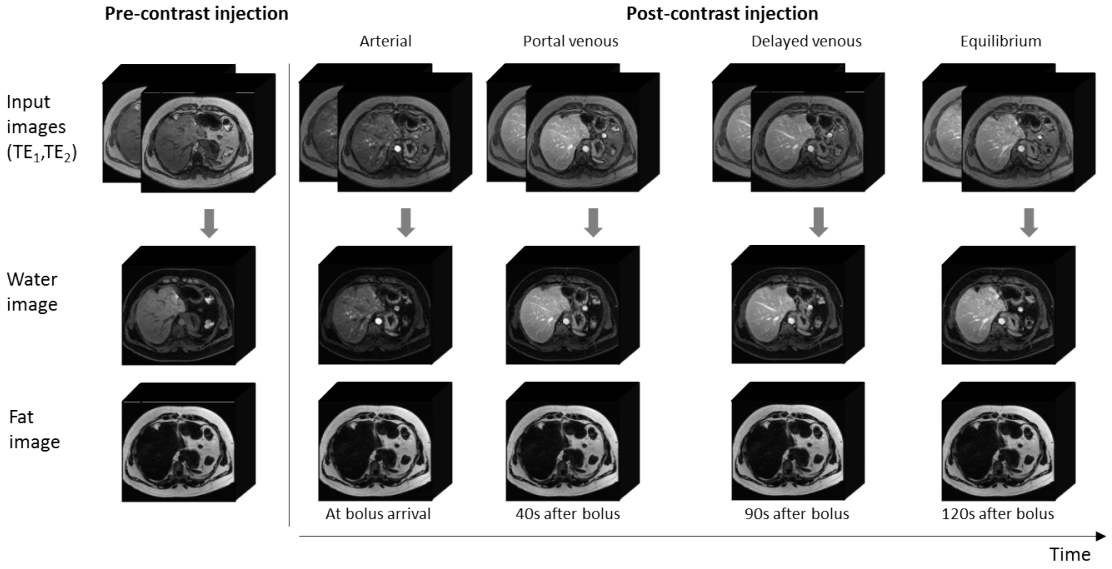

Figure 4.10: Schematic temporal sequence of dynamic contrast-enhanced liver MRI. The same imaging sequence is performed before contrast injection and at multiple time points after contrast injection to cover significant stages of contrast wash-in and wash-out. At each time-point a 3D dual-gradient echo imaging procedure is performed to be able to separate the water and fat signal retrospectively.

dual-gradient echo images with constant imaging parameters is acquired followed by water-fat separation. The first one is acquired before contrast injection and is used as a reference image. Gadovist is used in clinical practice and was also used as contrast agent in this study with a concentration of 0.1 mmol/kg injected as bolus injection using a power injector set to 2 cc/s, followed by a 20 cc saline flush at 2cc/s. Gadovist is a paramagnetic non-selective contrast agent that contains Gadolinium. The physical principle behind the increase of contrast in T_1-weighted images is described in Section 2.6. Gadovist is ranked to have low risk for the patients to develop nephrogenic systemic fibrosis (NSF). Gadolinium is increasing the signal intensity in T_1 weighted images by lowering the T_1 relaxation time of surrounding tissue. The contrast wash-in is monitored with a bolus track sequence that repeatedly measures a 2D coronal slice of the abdomen. At bolus arrival, the acquisition of the arterial phase images is started. The contrast is visible in the aorta, the hepatic artery and potentially in diseased tissue. The further contrast wash-in in the liver is monitored during the portal-venous phase that is typically 40 s after bolus arrival. The wash-out of contrast is further monitored during the delayed venous (90 s after bolus arrival) and the equilibrium phase (120 s after bolus arrival). Different tissue types have different temporal characteristics of contrast wash-in and wash-out dependent on their blood circulation and supply. This knowledge helps in separating healthy tissue from diseased as well as malignant from benign tumors.

Contrast-agent is furthermore helpful to determine the full extent of malignant tumors and to characterize extrahepatic diseases with non-selective contrast agents.

Because of the occurring incomplete breath-holds in clinical practice, the presented adaptive sampling is applied to abdominal DCE MRI to study the benefit for this application. Basic feasibility has to be shown for the adaptive sampling approach with injection of contrast agent. The acquisition stays basically the same as described in the Section 4.5.2. As opposed to the experiments described there, the application of contrast to the patient results in changing physical properties of the tissue. The relaxation times change continuously in time and spatially dependent during the entire examination. Therefore, the signal can no longer be regarded as temporally constant and thus potentially leads to artifacts in the image.

In conventional DCE abdominal MR imaging, the k-space is traversed in a linear manner. This results in minor artifacts in the image, because the contrast change is rather smooth. Potentially, the artifacts are less severe for parallel imaging compared with fully sampling, because the acquisition time is shorter and thus the contrast change is lower. The contrast in the image is mainly influenced by the time to k_0 that is half the scan time for conventional abdominal DCE MRI.

The adaptive sampling patterns are far more irregular. By construction, the central k-space is acquired first. Therefore, the time to k_0 is zero for the adaptive sampling patterns and the timing of the acquisition relative to contrast injection needs to be adapted to achieve exactly the same contrast as in the conventional case. A more challenging fact to consider is the irregular sampling after the acquisition of the calibration lines. Temporally close profiles are distributed over k-space, instead of being 'spatially' close to each other in k-space. This can result in a totally different signal intensity of spatially close profiles in k-space that appear as artifacts in image space. The artifacts seem comparable to incoherent aliasing that appears if undersampled data is Fourier transformed to image space without a CS reconstruction performed before. As opposed to the incoherent aliasing, the artifacts due to signal variations are not removed by a CS reconstruction, because the artifacts are induced by inconsistencies in the acquired data and not by unacquired k-space profiles. This observation points out that, although the experimental parameters are almost unchanged, the application has to cope with even more difficulties.

Abdominal imaging was performed on one healthy volunteer and four patients on a

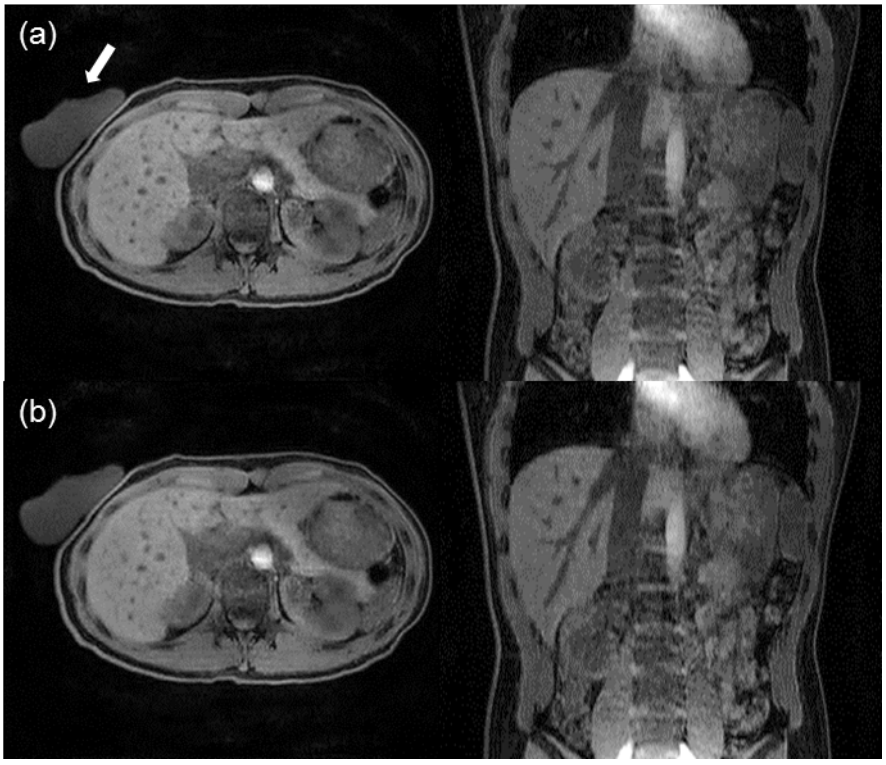

Figure 4.11: Images reconstructed from data acquired before contrast-injection. The images correspond to the pre-contrast injection images of the clinical protocol. (a) is reconstructed from the first $19s$ of the scan with stable breath-hold, while (b) is reconstructed from truncated data to simulate shorter breath-hold of 13s. A control volume was added within the FOV (see arrow) to study the signal intensity dependence on the breath-hold duration, because quantitative enhancement characteristics are used for diagnosis.

3T scanner (Achieva, Philips Healthcare, Best, The Netherlands) at the University of Texas Southwestern Medical Center using a 16-element torso coil. Embedded in a clinical DCE series, two additional 19 s breath-hold acquisitions were obtained: one before contrast injection and one after the clinical DCE acquisitions in order to avoid interference with the existing clinical procedure. As a side-effect the difficulties caused by signal variations are expected to be less harmful in the late phases compared with the early phases. The early image is comparable to the first pre-contrast dataset of the clinical series, while the late image is comparable to the last post-contrast acquisition. A T1-weighted spoiled dual-gradient-echo sequence with a $TE_1/TE_2/TR$ of $1.13/2.0/3.7$ ms (mDIXON) and a flip angle of $\alpha = 10^\circ$ was employed to cover a typical FOV of $340 \times 262 \times 300\,\text{mm}^3$ with an actual acquired spatial resolution of $1.5 \times 1.5 \times 3.0\,\text{mm}^3$. A combined PI and CS reconstruction (ℓ_1-SPIRiT [51]) was used for reconstruction of the two echo images, and two-point water fat separation [97] with flexible echo times was performed as a final step.

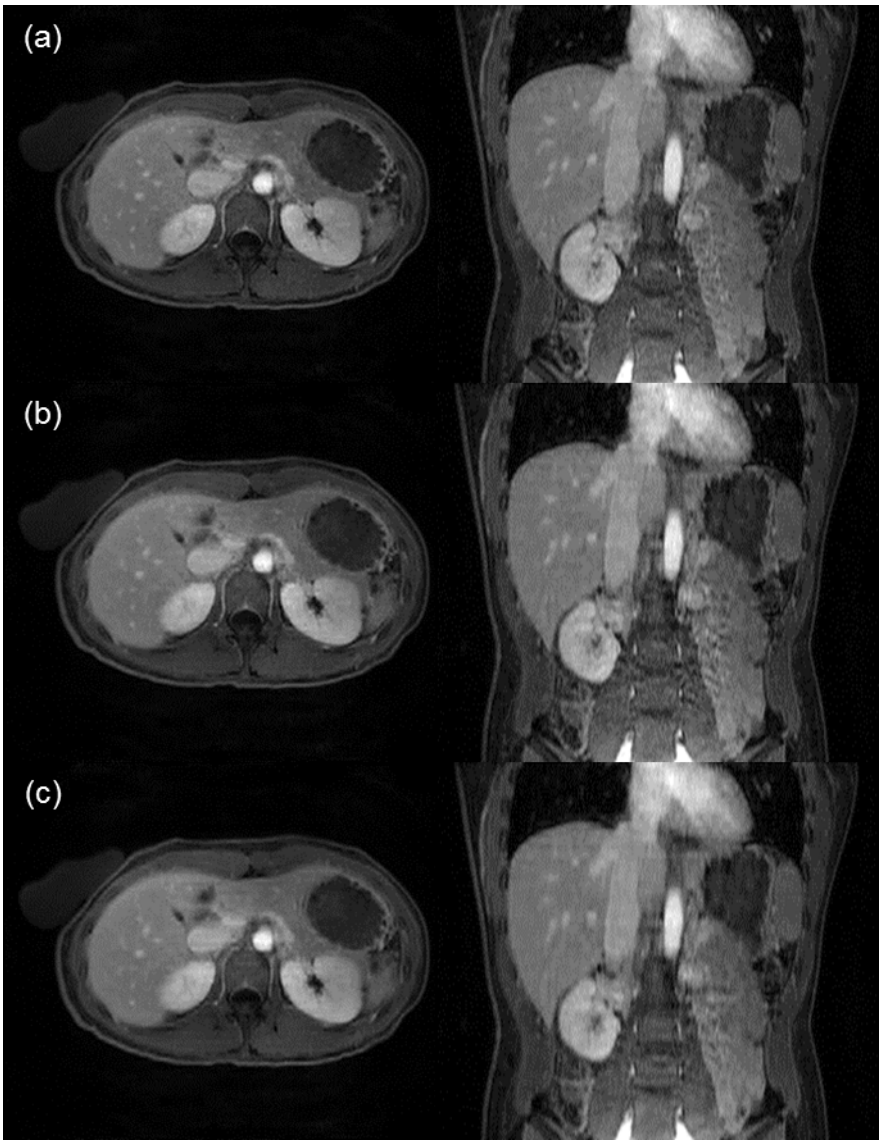

Figure 4.12: Images reconstructed from data acquired after contrast-injection and after the dynamic series of the clinical protocol. The images therefore correspond best to the last phase of the clinical protocol. (a) is reconstructed from the first 19s of a scan with stable breath-hold, while (b,c) are reconstructed from truncated data to simulate shorter breath-holds of 13s (b), and 10s (c). The control volume remains in the FOV for the post-contrast images.

The reconstruction ensures the same final voxel size of pre- and post-contrast acquisitions to enable subtraction. Because relative enhancement is a crucial criterion for lesion characterization in clinical practice, one needs to be sure that the signal amplitude is not influenced by the breath-hold duration. This is evaluated in this work with an additional phantom placed on the volunteer, acting as control volume within the FOV. Signal difference maps are calculated for distinct breath-hold durations of pre- and post-contrast images to evaluate the influence of the breath-hold duration on quantitative enhancement characteristics.

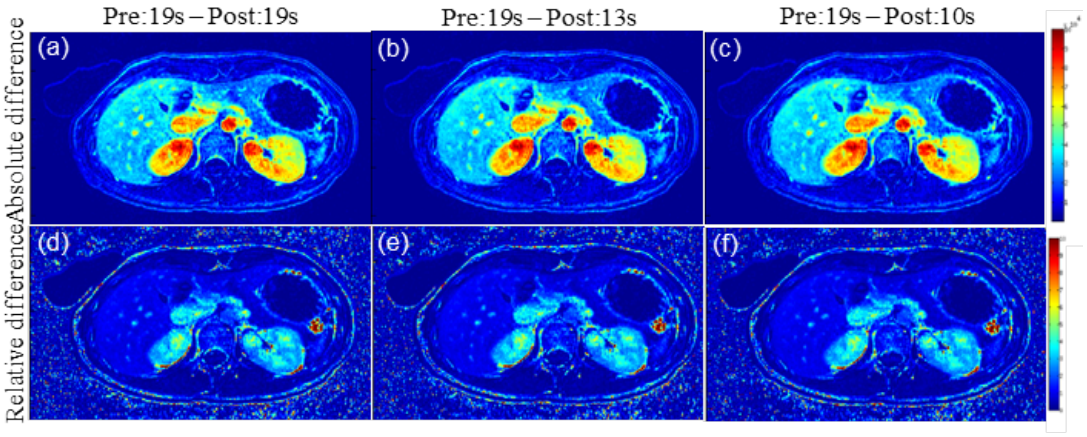

Figure 4.13: Dependence of enhancement characteristics on the breath-hold duration. (a-c) is the absolute difference between the water images of the two phases ($S_{post} - S_{pre}$), while (d-f) is the ratio between difference and the pre-contrast image ($(S_{post} - S_{pre})/S_{pre}$). The breath-hold duration of the pre-contrast scan is kept constant, while the post-contrast breath-hold is truncated to varying breath-hold durations. The images show enhancement in expected regions within the body with quantitative values that are independent of the breath-hold duration. The signal intensity within the control volume remains unaffected for all breath-hold durations.

The data shown in Figures 4.11(a) and 4.12(a) are from acquisitions with 19 s breath-hold duration before contrast injection, and the other with the same breath-hold duration, but after the clinical dynamic protocol. The additional control volume can be seen in the axial images. In addition, a shorter 13 s breath-hold Figure 4.11(b) was also simulated by truncating the acquired data. Pre-contrast images were successfully reconstructed from various simulated breath-hold durations with preservation of image quality (Figure 4.11). Post-contrast images were also reconstructed with shorter, i.e. 13 s in Figure 4.12(b), and 10 s in Figure 4.12(c) simulated breath-holds. Reconstruction of pre- and post-contrast images can be performed for different breath-hold durations indicating robustness against premature breathing onset. Evaluation of the influence of the breath-hold duration on quantitative enhancement characteristics needs to be performed. Therefore, the difference between the pre- and post-contrast images as well as the ratio of the difference and the pre-contrast images is calculated for different breath-hold durations of the post-contrast images. For Figure 4.13, the pre-contrast images are taken from the first 19 s, while the post-contrast images are from 19 s, 13 s and 10 s breath-hold durations. Figure 4.13 indicates expected enhancement characteristics within the body and no significant change of the mean value within the control volume for the two acquisitions with distinct breath-hold duration. The breath-hold duration influences the resolution of the motion artifact-free images, but leaves the quantitative information unaffected. The breath-hold position of the pre -and post- contrast images

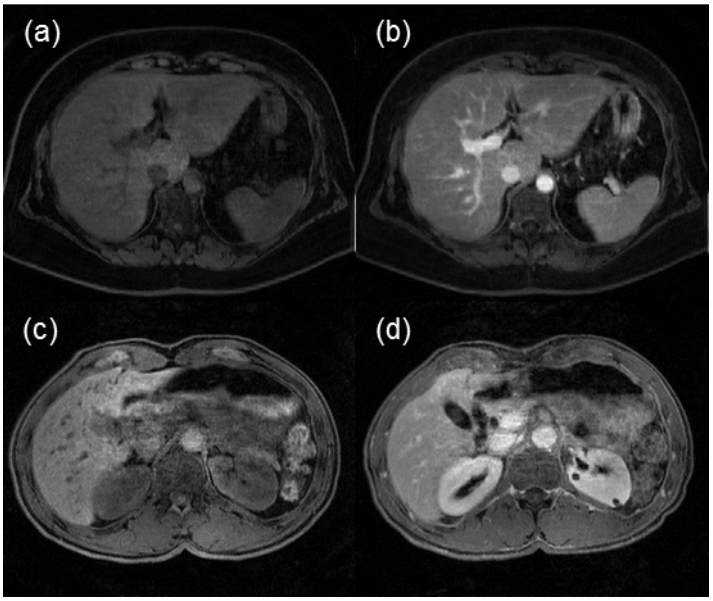

Figure 4.14: Reconstructed patient data. Images are from two different patients. On the left: patient I (a) pre-, (b) post-contrast. On the right: patient II (c) pre-, (d) post-contrast, acquired with the proposed adaptive sampling pattern. Promising image quality without motion artifacts is also achieved in patients.

is assumed to be consistent for these experiments. This experiment was performed on a healthy volunteer, but it was also tested on three patients after the influence of the breath-hold duration on quantitative diagnostic values was clarified. Representative pre- and post-contrast water images out of 3D patient data from two different patients are shown in Figure 4.14. In Figure 4.14, (a,b) correspond to one patient, while (c,d) correspond to the other. Pre-contrast images are shown in (a,c), while post-contrast images are shown in (b,d). The image quality is promising without any motion artifacts induced by respiration.

4.5.4 Dual-contrast imaging within one breath-hold

In MRI, several images with different contrasts are often advantageous for a precise differential diagnosis. To avoid potential respiratory motion induced artifacts, abdominal imaging is usually performed during one or multiple breath-holds. Nevertheless this approach can lead to spatial inconsistencies between data acquired in different breath-holds. Recently, it was proposed to perform multi-contrast MRI within the same breath-hold [116] using highly accelerated parallel imaging (PI). However, the disproportionately long delay between the two scans of approximately 1 s increases the risk of a premature onset of breathing during the second scan and thus degraded image quality.

To overcome this problem, fast sequence switching [117] and the proposed adaptive sampling is applied to dual-contrast imaging.

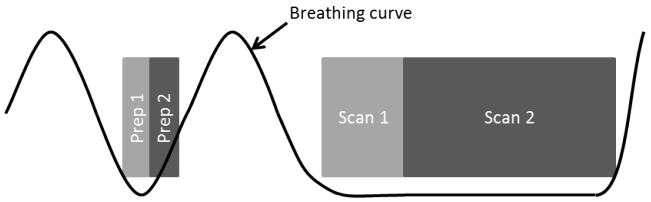

Figure 4.15: Schematic illustration of temporal sequence for dual-contrast within one breath-hold. The preparation scans of both scans are performed before the actual scan while the patient/volunteer is free-breathing. After the breath-holding instructions, the first scan is started manually and its duration easily fits into the breath-hold. Immediately at the end of the first scan, the second scan starts automatically

The aim is to acquire two distinct scans immediately after each other to ensure consistency of the scans. The required preparation phases of both scans are performed before the actual acquisition while the patient is free-breathing as shown in Figure 4.15 to ensure they are not performed in between the scans. After their completion, breath-hold instructions are given and the first scan is performed immediately at the beginning of the breath-hold. During the first scan that is chosen to last only a fraction of the breath-hold, it is likely that the patients are capable to hold their breath. Therefore, this scan could be fully sampled. This is no stringent claim, the first scan can also be acquired using acceleration techniques like parallel imaging. Switching to the subsequent scan is performed using a spectrometer task swapping approach, pre-storing arbitrary MR sequences on the data acquisition system as parallel tasks, allowing switching sequences in less than a few micro-seconds. The second scan, starting immediately after the first scan, has to be designed differently to be able to cope with sudden breathing onset. The adaptive sampling approach presented in this chapter is applied to this dual-contrast imaging sequence.

Abdominal imaging was performed on volunteers on a 1.5T scanner (Philips Healthcare, Best, The Netherlands), using a 16-element torso coil. For the first scan a conventional 2D Look-Locker sequence, sampling 12 complete low-resolution single shot gradient-echo images after inversion ($\alpha = 10°$, TE/TR : $2.8/6.4$ ms, resolution: $3 \times 2.6 \times 15$ mm^3, total scan time= 3 s) was chosen to estimate a central slice liver T1 map, reconstructed using conventional reconstruction. For the second scan, a T1-weighted

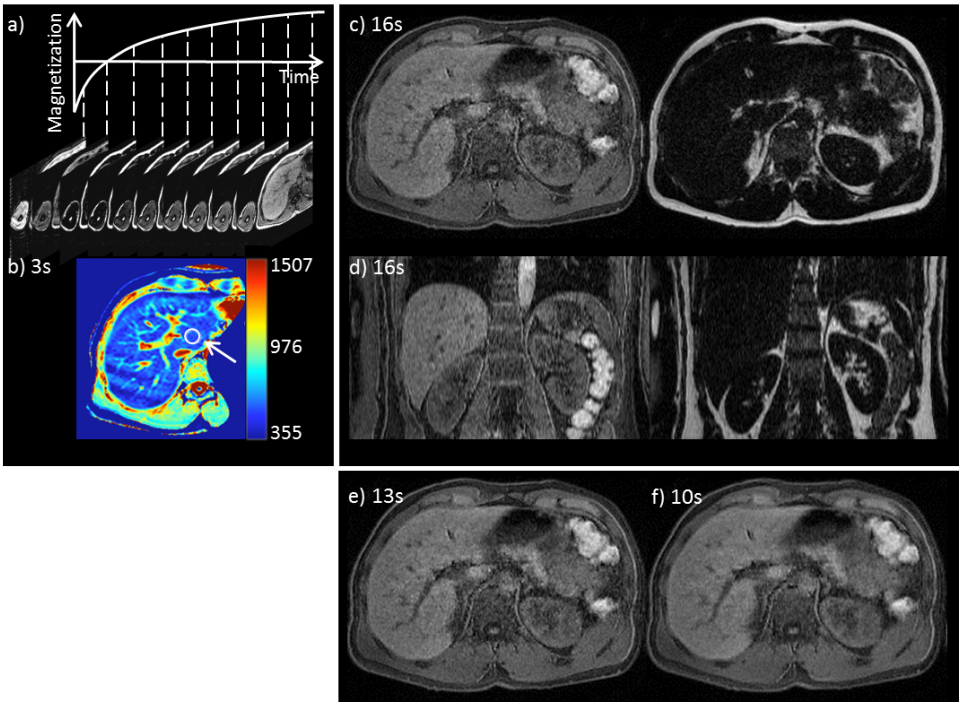

Figure 4.16: Results for dual-contrast single breath-hold abdominal MRI: In this example a standard Look-locker T1 mapping scan was combined with a second 3D water/fat resolved dual-echo Dixon. (a) Pixel-wise estimation of T1 and (b) resulting T1 map from the first scan (3 s scan duration) during a breath-hold. (c,d) Selected water/fat images from the second scan acquired during the same breath-hold. From the total breath-hold duration of 19 s were 16 s left for the second scan (c,d). Water images for simulated earlier breathing onsets resulting in scan duration of the second scan of 13 s (e) and 10 s (f), underlying the temporal resolution adaptation.

spoiled gradient-echo sequence with a $TE_1/TE_2/TR$ of $1.29/2.34/3.67$ ms was employed to cover a typical FOV of $380 \times 280 \times 240$ mm^3 with an actual spatial resolution of $1.5 \times 1.5 \times 3.0$ mm^3. A combined PI and CS reconstruction (ℓ_1-SPIRiT [51]) was used for reconstruction of the two echo images, and water fat separation [97] was performed as a final step.

The estimation of the T1 map of the liver from the first scan is shown in Figure 4.16(a,b) with a measured T1 value from ROI of 570 ms, while the reconstructed images from the second scan are shown in Figure 4.16(c,d). This volunteer held their breath for 19 s, with automatic scan termination at breathing onset. The effective scanning time of the second scan was 16 s. For comparison, this data was further undersampled to simulate breath-hold durations of (3+13) s (Figure 4.16(e)) and (3+10) s (Figure 4.16(f)) to emphasize the automatically adapted resolution of the second scan.

4.6 Discussion

Imaging of the abdomen often suffers from motion artifacts. Therefore, a novel approach for more robust 3D abdominal imaging with incomplete breath-holds was proposed and feasibility was shown in simulations and in vivo measurements for different applications. Good image quality was obtained for the single-echo and the water-fat images for all breath-hold durations albeit at different spatial resolutions. Motion artifact suppression by scan termination was clearly shown to be superior to using inconsistent data for reconstruction (cf. Figure 4.9). This approach ensures an optimal compromise between undersampling artifacts and spatial resolution for an arbitrary breath-hold duration, while preventing motion induced artifacts. Instead of adapting the spatial resolution in advance, based on an estimate of the breath-hold duration a particular patient is able to achieve, it is automatically increased during the scan. This is advantageous, because the breath-hold duration of a patient is difficult to predict, especially for sick or uncooperative patients, and in any case potentially diagnostically useful images can be obtained making undesired scan repetitions unnecessary.

In the previously proposed approach by Maki et al. [107], the acquisition is not terminated, and the complete dataset is used for reconstruction. This ensures full resolution, but leads to motion artifacts, dependent on the breath-hold duration. A simple extension of the previous method would be the combination with a motion sensor for scan termination. This would result in lower resolution than in the approach proposed here, which integrates PI and CS and, therefore, enables undersampling of k-space.

The main parameters for the generation of the sampling patterns are the number of calibration lines in the center of k-space, the number of fractions f and Ω. The number of calibration lines is mainly determined by the reconstruction and the energy of the signal. In the reconstruction technique used in this work (ℓ_1-SPIRiT), a convolution kernel fit is performed from the calibration lines. A sufficient number of equations is needed for this optimization process. Therefore, an increasing number of calibration lines up to a certain limit leads to an improved calibration kernel. Furthermore, it is advantageous if the part of the signal with highest energy is fully sampled. However, with increasing number of calibration lines, the time to acquire the central part of k-space is also increased, leading to lower spatial resolution.

For the selection of a suitable number of fractions, two competitive factors, acquisition

time of one fraction and distance between samples, have to be taken into account. An incomplete fraction results in an asymmetrically acquired k-space, which is less severe if the number of samples within one fraction is low. This makes a large number of fractions preferable. On the other hand, a larger number of samples in one fraction results in a reduced average distance between samples, and therefore, in reduced eddy currents. The potential asymmetry in k-space is caused by the chosen temporal order within the fractions according to the angle in polar coordinates of the profiles. Improvements can be achieved if the profiles within one fraction are traversed in a manner similar to a spiral. Another possibility is to choose the same number of profiles in a shot as in one fraction that ensures a symmetric sampling pattern. This potentially comes at the cost of lower temporal resolution of the motion sensing or of a higher distance between samples.

The evolution of the covered k-space area is determined by the parameter Ω through (4.5). This evolution together with the reconstruction determines the spatial resolution and the artifact level, which are competitive. To determine the reasonable range for Ω, simulations were performed on a retrospectively undersampled phantom scan. As expected from (4.5), the resolution improves for increasing Ω. At some stage, residual undersampling artifacts and noise arise, which cannot be removed by the reconstruction and become clearly visible for $\Omega = 12$. Therefore, as a compromise, $\Omega = 8$ was chosen for the experiments. This choice is specific for the chosen coil and sequence, which potentially needs to be adapted slightly for other configurations.

The chosen variable density is adapted only slightly to the expected signal distribution in k-space. It is decaying to the k-space periphery, which is an improvement compared with uniform sampling density. This choice for the sampling density, as implicitly given in (4.7), is just one possibility and can potentially be changed to an arbitrary function. Optimization could lead to further improved reconstruction results.

Once the maximum resolution is reached, the remaining scan time is used to improve the SNR and for better conditioning the reconstruction, until the patient starts to breathe. The acquisition adapts to the actually achieved breath-hold duration, which can be monitored either by external sensors or navigators, or can be determined from a series of images reconstructed from different amounts of data. Two different navigator methods were tested, the 1D pencil beam navigator and the k=0 navigator, while only one

was used in each acquisition. With the 1D pencil-beam navigator, a robust termination method was implemented. Scan termination is favorable compared to retrospective truncation because of patient comfort and scan efficiency. However, the 1D pencil-beam navigator has the disadvantage of interrupting the steady state of the magnetization in the imaging volume. Because of that, the intershot signal intensity varies resulting in contrast variations. Furthermore, the navigator can lead to magnetization saturation in the imaging volume. The use of motion detection based on repeatedly measuring the k-space center could avoid these artifacts [114]. The application of the k=0 navigator to imaging in the steady-state is obvious, but application to temporally changing signals is more challenging. Methods to cope with signal drift, like a running average as reference profile indicated significant compensation of the temporal behavior while still enabling detection of breathing onset.

The single echo images are reconstructed independently of each other in this study, instead of performing a joint CS reconstruction and water-fat separation [26, 27, 28]. As discussed in [26], the advantage of applying a joint CS reconstruction and water-fat separation reconstruction grows with the number of echoes, because both of the increased spectral dimension and the improved model accuracy. The reason for focusing on a sequential CS reconstruction and water-fat separation in this work is that the improvement expected from a joint CS reconstruction and water-fat separation is small for a two-point water-fat separation and hardly justifies the additional complexity.

The joint reconstruction of the temporal phases of a DCE examination is presented and discussed in more detail in Chapter 6. The presented approach is not restricted to gradient-echo sequences and can potentially be applied also to other sequences and contrasts. For this purpose, the acquisition order within the fragments needs to be adapted to match the imaging conditions for the particular sequence.

Two further applications for the proposed sampling patterns are presented in this chapter, DCE imaging of the abdomen and dual-contrast imaging. The concept of flexible scan termination based on the individual breath-hold duration of a patient can be applied to dynamic contrast enhanced imaging of the abdomen. Feasibility is shown here for a temporal phase acquired directly after the clinical protocol that is comparable to the equilibrium phase. Data were acquired with a fixed termination at a reduction factor of 2.5 with the k=0 navigator used for monitoring the breath-hold. The data were

retrospectively truncated to the achieved breath-hold duration. While the k=0 navigator proved to be reliable for healthy volunteers for imaging without contrast agent, the situation seemed different for inexperienced volunteers and patients with the administration of contrast agent. Further studies have to be done further study on this kind of navigator to apply it in a reliable way on patients. One major problem to address is the choice of the reference profile. Due to the breath-holding instructions, the first part of the scan is not necessarily the best choice for reference, because the breath is potentially not held yet. One option is the presented average over a fixed number of profiles or the running average over profiles as reference. The study shows that different breath-hold durations do not have an influence on the mean signal value which enables an evaluation of spatially restricted absolute and relative enhancement for diagnosis on the water/fat images as well as difference images. The adaptive sampling patterns need to be applied to the arterial phase to exploit the full advantages of the method, but the influence of the rapidly changing contrast on the k=0 navigator and the data consistency can lead to problems for this temporal phase.

Dual-contrast imaging could be of interest as a building stone for future liver perfusion studies, delivering a coarse T1 map to estimate relaxivity in every dynamic for high temporal correlation to improve perfusion analysis. However, the concept of combining multiple-contrast scans in a single breath-hold with ultra-fast sequence switching and the adaptive profile order to cope with early breathing onset without compromising image quality can find many other applications. With the proposed approach, multiple contrast images of the abdomen could be acquired quasi-simultaneously within a single breath-hold reducing the risk of misregistration. While the first scan is uncritical, the second scan is adapted to the breath-hold capabilities of the patient and terminated automatically in case of breathing onset preventing motion artifacts at the cost of a potential lower resolution.

Chapter 5

Dual-scan multi-echo acquisition for estimating the liver fat fraction

The liver fat fraction is an important biomarker for early diagnosis of non-alcoholic fatty liver disease (NAFLD) that can result in liver cirrhosis and carcinoma in later stages of corresponding diseases. Diseases of the liver are hard to recognize, before the majority of the liver is affected, because the liver works normally before. Early diagnosis is especially relevant for liver diseases, because apart from the skin, the liver is the only organ that can regrow and thus recover from diseases if a sufficiently large amount of the organ is still working.

Quantitative assessment of the liver fat fraction with MRI is becoming more important. The reason for this is twofold. First of all, the occurrence of NAFLD increases significantly due to the increasing obesity in developed countries. Furthermore, the conventional method for diagnosis, the biopsy, has clear disadvantages. It is an invasive technique that always includes some risk, and it is a point-wise probing approach that is less accurate, because the small number of probes are not representative for the whole liver.

MRI is a non-invasive alternative to estimate the quantitative fat fraction of the whole liver [118]. The quantitative value does not only rely on a small set of samples, but on the water/fat content of the whole organ. This sounds promising, but imaging of the abdomen is challenging due to long scan duration in MRI and the restricted ability of patients to hold their breath to prevent motion artifacts. The imaging times become even longer for multi-echo sequences that are needed for a water-fat separation based

on chemical shift encoding techniques [95, 97, 98]. The separation requires a minimum of two echoes, obtained at different TEs, and is performed during reconstruction. The required number of echoes depends on the number of unknowns in the signal model, namely the number of fat peaks in the spectrum. With increasing number of included peaks, the accuracy of the separation improves. This is especially relevant for the quantitative fat fraction, because abnormal values already begin at a rather low percentage of the fat content.

Lately, different papers were published facing the topic of fat fraction estimation from MRI measurements [118, 119, 120]. The fat fraction is also relevant in other parts of the body, as described in [121]. The techniques require a correction of the magnetic field inhomogeneities and T_2^* relaxation to obtain an accurate separation and artifact minimization. Multi-echo sequences can be performed using unipolar or bipolar read-out gradients. Unipolar gradients use the same read-out direction for each echo with fly-back in between. This increases the length of the acquisition compared to bipolar read-out gradients, but does not require correction for the different shift directions of the fat from every other echo due to gradient reversal.

The breath-hold duration of patients can be difficult to predict and is potentially shorter than for healthy volunteers. Breathing onset before scan termination can result in respiratory motion artifacts. These artifacts can lead to an incomplete separation or to inaccurate estimates of the fat fraction. The influence of a premature onset of breathing for an accelerated fat fraction scan using SENSE with a reduction factor of two is shown in Figure 5.1. The total scan duration was 17 s, and the volunteer once held the breath for the whole scan time, and once started breathing after 14 s leading to respiratory motion artifacts. Artifacts are already visible in the scan with 17 s breath-hold duration, although the volunteer perfectly held the breath. The source of these artifacts is not completely clarified yet, but it is obvious that inconsistency can produce even severe artifacts in undersampled CS acquisition due to inconsistency in the data.

5.1 Methods

The artifacts in the images in Figure 5.1 have multiple reasons. One is definitely the slow convergence of the transverse magnetization to the steady state, although the flip angle is rather low. Furthermore, the low resolution that is needed to achieve sufficient

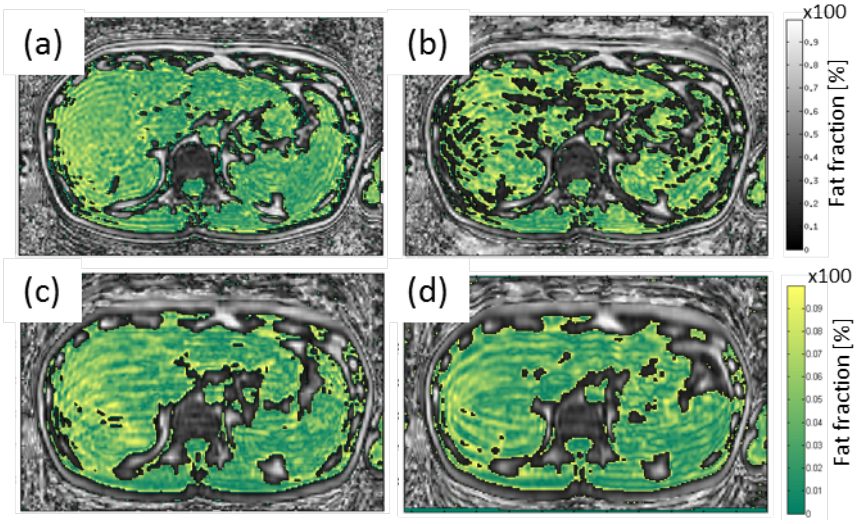

Figure 5.1: Influence of motion on fat fraction maps. The images are reconstructed fat fraction maps that were acquired with a multi-echo sequence with a SENSE factor of two (a,b) and the adaptive sampling pattern described in Chapter 4 (c,d). During the acquisition of the images on the left (a,c) the volunteer held the breath for the whole acquisition (17 s). For the images on the right (b,d) the volunteer started breathing after holding the breath for 14 s. Artifacts are already visible in the 17 s breath-hold standard acquisition (a), but are much more pronounced for the incomplete breath-hold in (b) leading to a higher estimate of the liver fat fraction with values higher than 0.1 in some regions of the liver. The images acquired with the adaptive sampling patterns have clearly degraded image quality. Due to inconsistency in the data, the CS reconstruction fails.

SNR, induces Gibbs ringing. The large number of echoes sampled with bipolar read-out gradients can potentially induce eddy current related effects.

To obtain some insight into the nature of the induced artifacts, multiple experiments were performed that indicate a strong dependence on scanning parameters, e.g. TR, TE, TFE-factor, resolution, flip angle, and acquisition order. Furthermore, the artifacts are different for distinct echoes as is visible in Figure 5.2 showing different echoes from a single scan with six echoes and full sampling with linear profile order on a volunteer, who perfectly held the breath during the scan. Fully sampled experiments were performed on phantoms to preclude motion as the origin of the artifacts. A dependence on the echo number and the echo times is also visible, see Figure 5.3. The images in Figure 5.3 are central slices out of a 3D gradient echo sequence with six Echoes, and TE1/ΔTE/TR of 0.95/0.8/6.1 ms. The artifacts appear more pronounced for later echoes, e.g. the sixth echo in (c), then for the first (a) and third (b) echo. Problems arising from a multi-echo sequence, especially with bipolar read-out, were already mentioned in [121] that finally used multi-acquisition to reduce the artifacts while accepting

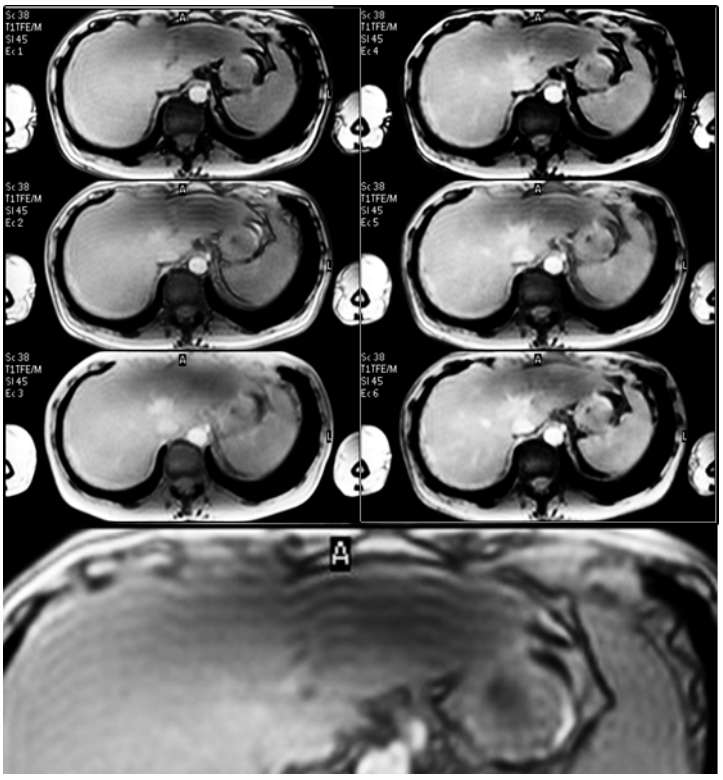

Figure 5.2: Echo images from a fully sampled data acquisition and a linear profile order. Artifacts are already visible in these images although the breath was held. The artifacts appear different for different echoes. In the lower part of the figure a detailed view of one echo is shown to clarify the appearance of artifacts.

prolonged acquisition times.

The examples of experiments that were performed for this work indicate that the experimental parameters need to be carefully chosen. Otherwise, the signal is quite unstable, leading to artifacts in the image for an irregular sampling. The principal ability to reconstruct an image from retrospectively undersampled data does not imply that reconstruction is also possible from prospectively undersampled data, because the sampling process can have significant influence on the signal. For demonstrative purposes, an example of the influence of a smooth estimated signal build up with time is shown in Figure 5.4 for a simulated phantom data. The distribution of the signal variation in k-space is shown in (a) for a linear profile order (blue) and a random profile order (black). To mimic the effect, the Fourier transformed image data of a phantom were multiplied with the weighting factors. An inverse Fourier transform results in the images shown in (b) for the linear profile order and (c) for the random profile order. It is clearly visible that the random profile order produces more severe artifacts than the linear profile order. The artifacts from the random sampling patterns seem comparable to incoherent undersampling artifacts and thus hard to distinguish in case of undersampled data

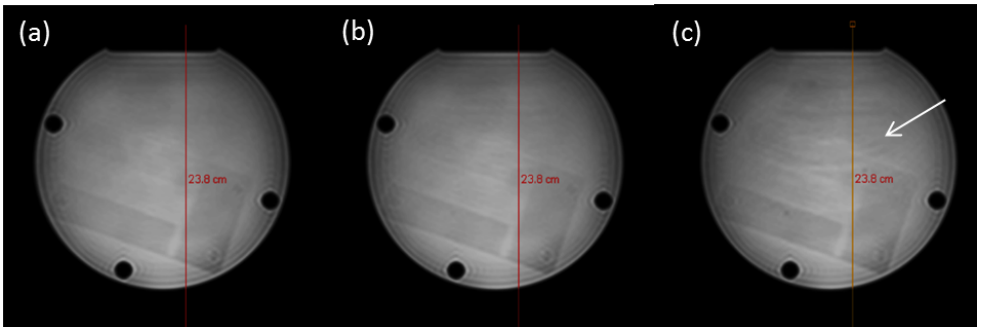

Figure 5.3: Echo images from a phantom scan. The phantom data was fully sampled on a phantom to investigate the causes of artifacts, like motion and undersampling. The data acquisition was performed with the adaptive sampling pattern in low-high order without scan termination before the data was fully sampled. Screen shots of the first echo is shown in (a), the third echo in (b), and the sixth echo in (c). The vertical red line indicates a profile that is not shown here. The artifacts appear much more severe for later echoes than for the first one.

for CS reconstruction. Furthermore, the artifacts that seem comparable to incoherent undersampling artifacts cannot be removed with a CS reconstruction, because they are induced by inconsistency in acquired data and not by unacquired data. The pixel-wise difference image to the original phantom is shown in (d) for the linear order and (e) for the random order. This is only one complication induced by an irregular sampling, apart from potential additional eddy current effects that might occur compared with linear profile order.

The artifacts were more pronounced in later echoes, visible in Figure 5.3. No combination of experimental parameters was able to remove the artifacts completely for all echoes, but some make them less apparent in the first echoes. This suggests acquiring only earlier echoes making use of the adaptive sampling pattern described in Chapter 4.

This enables a flexible scan termination, respectively truncating the data retrospectively and reconstructing from consistent data. However, for an exact estimation of the fat fraction, a larger number of echoes is required to support a more precise signal model. Thus, the data for the fat fraction maps were acquired in a two stage procedure with a gradient echo sequence sampling three echoes each, see Figure 5.5. The echo spacing ΔTE and the repetition time TR in both sub-scans coincide, but the two scans differ by the echo times set by the first echo. Let the echo time of the first echo in the first scan be TE_1, the shortest possible echo time, then the echo time of the first echo in the second scan is $\mathrm{TE}_1 + \Delta\mathrm{TE}/2$. The repetition time is chosen to be the shortest possible for the second scan. This choice of acquisition parameters effectively halves

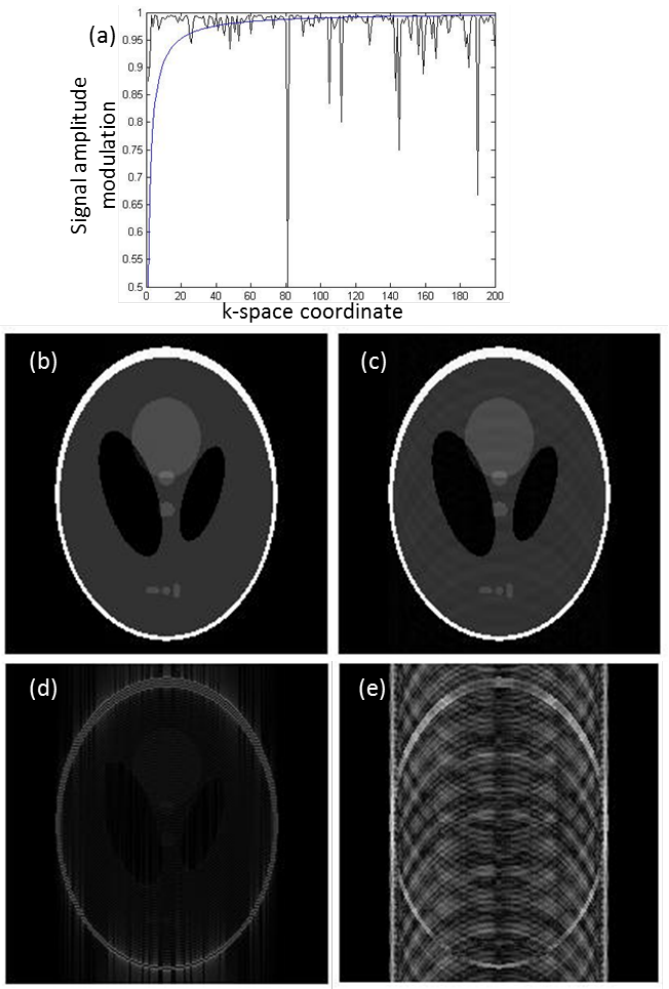

Figure 5.4: Influence of the sampling pattern for signal with signal amplitude varying. The signal amplitude in k-space was modulated along one direction with the weightings shown in (a) that are distributed in a linear sampling pattern (blue) and in a random sampling pattern (black). The artifacts induced by this weighting factors are shown in (b) for the linear order and in (c) for the random order. In image (b) the artifacts are hardly visible, while the artifacts in the image in (c) seem comparable to incoherent undersampling artifacts. The corresponding difference to the reference image is shown in (d) and (e).

the echo spacing, which would not have been possible with the standard acquisition and other parameters unchanged, see upper part in Figure 5.6. This dual-scan procedure slightly lowers the scan efficiency, because 2TR are required to obtain six echoes, and 2TR of the dual-scan is slightly larger than the TR of the single scan multi-echo scan with six echoes. The scans were performed directly after each other (Figure 5.6 (a)) or interleaved after execution of one kernel (Figure 5.6 (b)) with a sequence switching approach [117]. One kernel corresponds to one TR in FFE sequences and one TFE shot in TFE sequences. Both possibilities were tested for this application, and results are shown in the following section. This technique was already used in Section 4.5.4 for

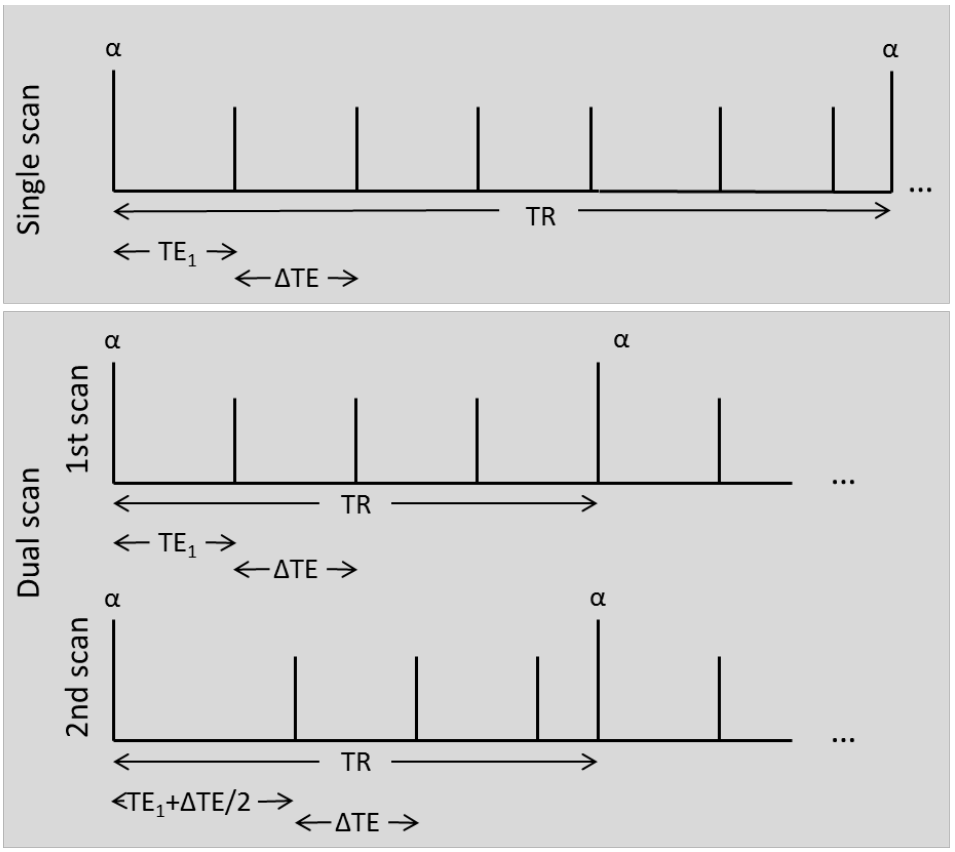

Figure 5.5: Timing of the single scan multi-echo acquisition compared with the dual scan multi-echo acquisitions. The single scan multi-echo acquisition acquires 6 echoes after the excitation pulse α. Dual scan: The first scan is acquired with three echoes using the shortest possible TE_1 and $\Delta\mathrm{TE}$. The TR corresponds to the TR from the second scan that is slightly larger than the shortest possible from the first scan because the echoes from the second scan are shifted by a fixed amount $\Delta\mathrm{TE}/2$. Apart from that the two scans are equivalent with the same flip angle α of the excitation pulse and other experimental parameters.

the acquisition of two contrasts in one breath-hold.

The data shown in the following section were acquired with adaptive sampling patterns, but without the additional navigator to minimize additional influences on the steady state of the signal. The data can be truncated retrospectively to include only consistent data in the reconstruction.

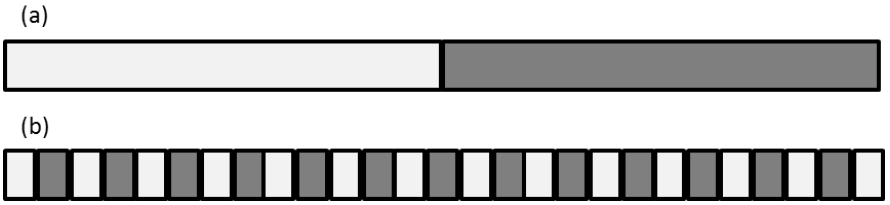

Figure 5.6: Explanation: interleaved scan and interleaved kernel. The two scans, indicated by gray and white areas, were acquired with different temporal order. The first order is called interleaved scan (a), which means acquiring the first scan completely or with a predetermined undersampling factor and afterwards switching to the next scan. The other possibility is interleaved kernel (b), which means that switching is performed after one kernel of a scan. A kernel has different definitions for TFE and FFE sequences. A kernel in TFE sequences is one TFE shot with a duration of the TFE-factor multiplied with TR. In FFE sequences, a kernel is one excitation pulse with the following multi-echo read-outs and has a duration of 1 TR.

5.2 Experiments

Experiments on four healthy volunteers, age 30-54, were performed on a 3 T scanner (Philips Healthcare, Best, The Netherlands) with a 3D T1-weighted spoiled multi-gradient-echo sequence, for water-fat separation using a six-point Dixon method (mDIXON [97]), employing a 32-element torso coil. The used mDIXON algorithm enables a flexible choice of the echo times and thus eases sequence design. The flip angle was $3°$, $\mathrm{TE}_1/\Delta\mathrm{TE}/\mathrm{TR}$ was $1.07/1.3/5.8$ ms, respectively $1.72/1.3/5.8$ ms, acquired using bipolar gradients with a pixel bandwidth of 1081 Hz, the FOV was about $375 \times 240 \times 230$ mm^3, and the target actual spatial resolution was $2.8 \times 2.8 \times 3.6$ mm^3, respectively $2 \times 2 \times 3.6$ mm^3 covering the whole liver.

The calculation of the adaptive Poisson-disk sampling patterns was performed on the scanner after scan planning to enable prospective undersampling of the data and flexible scan termination. For imaging on volunteers, the number of fractions was 30, and $\Omega = 4$ was chosen. The resolution of the fat fraction scans is much lower. Sparsity is first of all expected for higher frequencies, thus the achievable reduction factor is lower.

The reconstruction is performed off-line so far. To accelerate the reconstruction, a coil compression technique [22] was used before ℓ_1-SPIRiT [51]. The signals from the 28-channel coil were reduced to ten virtual channels without significant information loss. The compressed signal was then used as an input for the CS-PI reconstruction that was also used for the reconstruction of the images in Chapter 4. The resulting images from the individual coils were combined using a Roemer [13] reconstruction to obtain one

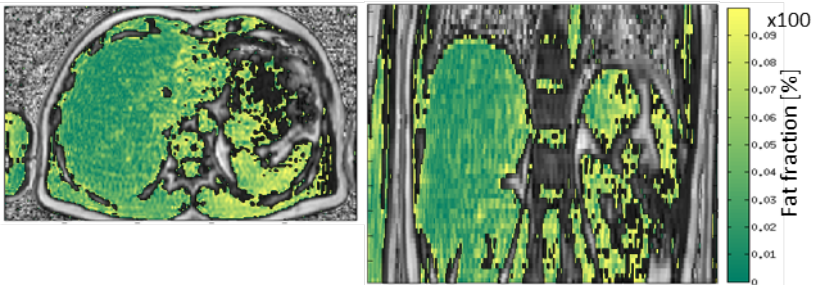

Figure 5.7: Axial fat fraction map and coronal reformat. The images were acquired within two scans with a scan pause of approximately 2 s in between, both acquired with a reduction factor of four to be able to acquire them in one breath-hold. The sampling corresponds to the sequence switching scheme shown in Figure 5.6 (a). The scans both consist of three echoes with different echo times, but the same echo spacing and repetition time. The fat fraction maps show non of the artifacts visible in the six echo scans suggesting further investigation to reduce the scan pause between the scans.

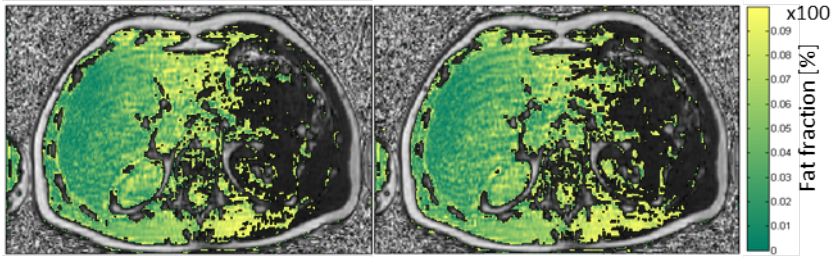

Figure 5.8: Fat fraction maps from two scans each without spacing between the scans. The images were reconstructed from two scans acquired interleaved and a reduction factor of four with adaptive sampling patterns. The switching between the scans is performed after completion of the first scan for the image shown in the left, corresponding to the sequence switching scheme shown in Figure 5.6(a), and after each TFE shot on the right, corresponding to the sequence switching scheme shown in Figure 5.6(b). The gray-scale ranges from zero to one to see the underlying anatomy and the colored overlay from zero to 0.1 for better distinction in the liver. For this volunteer the artifacts seem more severe for the switching after each kernel than for switching after the completion of the first scan.

complex valued image for each of the six echoes. The echoes are ordered according to their echo times respecting the reverse read-out gradients of the second echoes from each scan. To these six echo images, an mDIXON [97] separation step was optionally applied, resulting in one water and one fat image. Based on the water W and fat images F the 3D fat-fraction map Q is calculated according to

$$Q = \frac{|F|}{|F| + |W|}. \tag{5.1}$$

In Figure 5.7, the acquisition was performed comparably to interleaved scan, but with a scan pause of 2 s in between to be able to see the benefit of this scan procedure before

implementing the combination of the adaptive sampling pattern together with the fast sequence switching approach on the scanner. The data were acquired on a volunteer with good breath-holding capabilities that could hold the breath during the acquisition of both scans. The reconstructed images have good image quality suggesting the need for further work in this direction.

The combination of the fast sequence switching with the adaptive sampling patterns was implemented for the Ingenia 3T scanner, and fat fraction maps were acquired using the approach of distributing the six-echo scan to two three-echo scans and acquisition with adaptive sampling patterns. To reduce disturbances, the acquisition was performed without an additional navigator, and the truncation was performed afterwards. The scans were automatically terminated, after a reduction factor of four was achieved.

Reconstructed images are shown in Figures 5.8 and 5.9 for two volunteers. The data for the images in Figure 5.8 were acquired using a TFE sequence with a TFE factor of 150 and further experimental parameters described earlier in this section. The left image is obtained with the interleaved scan approach and the right image with the interleaved kernel. Both images indicate superior image quality and more reasonable fat fraction values compared with the images in Figure 5.1(b-d).

The same acquisition with slightly reduced resolution and a TFE factor of 30 was performed on a different volunteer, and the images are shown in 5.9(c,d). The image in (c) is obtained using the interleaved scan and (d) using interleaved kernel. The images in (a,b) are obtained from an FFE sequence using (a) interleaved scan and (b) interleaved kernel. The image quality is comparable in the images with slightly less reasonable values for the FFE interleaved kernel acquisition. It is visible that the water-fat separation could not perfectly separate the water and fat content in the volunteers for both methods, interleaved scan and interleaved kernel.

5.3 Discussion

The application of the adaptive sampling patterns to the fat fraction estimation described in this chapter is a perfect example to show that reconstruction from retrospective and prospective undersampled data has a different degree of difficulty. Inconsistency in the data can be induced by eddy current effects caused by the irregular sampling. However,

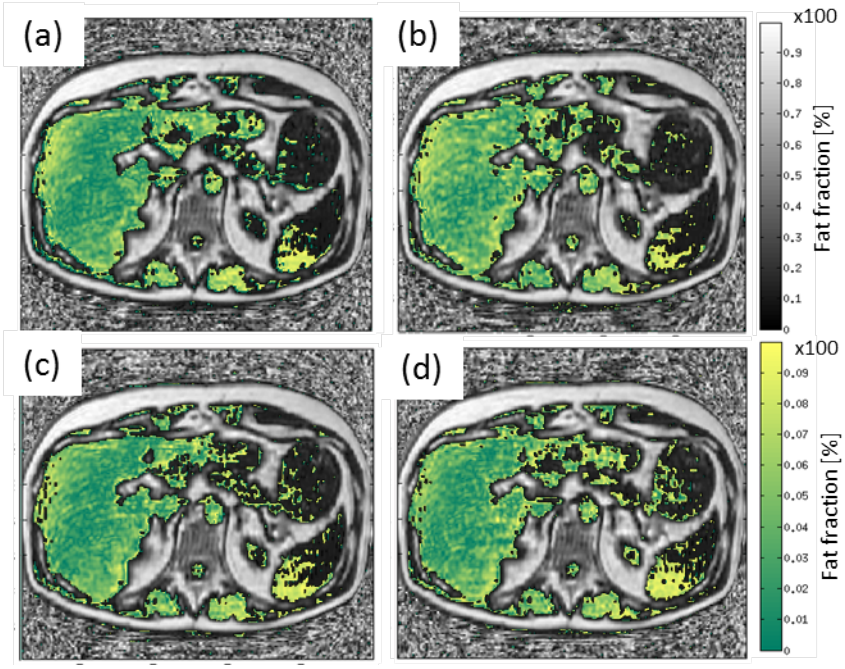

Figure 5.9: Comparison of acquisition methods. The images in (a,b) were obtained using a FFE sequence and (c,d) using a TFE sequence. The switching between the two scans can be performed at different points in time. The images in (a,c) were obtained from interleaving scans, which means that the first scan needs to be complete before the second scan is immediately performed. During the acquisition of (b,d) the switching was performed after completion of one kernel and thus multiple times during the scan.

apart from that, irregular sampling causes strong signal fluctuations in k-space, even if the signal variation is temporally smooth. It was argued in this chapter that this causes clearly severe artifacts for the irregular sampling compared with linear sampling. Retrospective undersampling of linearly sampled data ignores this difficulty completely. Therefore, one big issue for this application was to reduce signal inconsistency before starting with an undersampling of these data during acquisition. The distance between temporally close profiles is controlled in the same way as described in Chapter 4 by traversing the profiles from fractions according to their angle in polar coordinates.

By variation of the experimental parameters, the artifacts were not removed completely, and thus further investigations need to be undertaken. Nevertheless, the experiments on phantoms indicated best image quality for the first echoes and suggested the dual-scan multi-echo sequence. Each of the scans in this approach contained only half the echoes compared with the standard approach. Instead, two scans are acquired in an interleaved mode to perform the water-fat separation based on the same total number of echoes. One disadvantage of this approach is the slightly reduced scan efficiency.

Furthermore, the dual-scan multi-echo acquisition has some other interesting advantages. Given a fixed gradient performance, very high spatial resolution may result in an unacceptable long inter-echo time, which is not appropriate for proper chemical shift encoding and subsequent water-fat separation. The proposed approach represents a hybrid chemical shift encoding approach that can help to increase the flexibility to tailor the sequences to the clinical needs.

The dual-scan multi-echo acquisition enables different possibilities to order the scans temporally, i.e interleaved scan and interleaved kernel. Performing the scans one after another has the advantage that the scans hardly influence each other. On the other hand, the adaptive scan termination can only be applied to the second scan with this choice. The duration of the first scan has to be chosen prior to scan execution implying a limitation. The joint reconstruction described in Chapter 6 can also be used to reconstruct the data from both scans together. This is especially helpful, as the data from both scans are acquired during the same breath-hold and are therefore spatially corresponding. This could help to achieve the same image quality for both scans, but is not implemented for this work. In the interleaved case, the scan termination can be applied to both scans exploiting the whole potential of the breath-hold for both scans. Nevertheless, this is only possible if the scans do not influence each other.

The CS reconstruction of the echoes is performed separately in this work. This is not stringent, and reconstructing the echoes together can improve the image quality, especially if the undersampling patterns of the echoes are distinct. The water-fat separation is performed based on the echoes from both scans of the dual-scan approach. The artifacts are clearly reduced compared to the initially performed experiments, but are not completely gone. A reason for the incomplete separation of the water and fat content could be a small inaccuracy in the echo times. The separation algorithm is based on equal distance between echoes. Due to the distribution of the echoes to two scans, the echo time of the first echo of the second scan is manually determined based on values given in the user-interface of the scanner. The physically used values differ slightly and can lead to a small deviation from the required value for the echo time of the first echo from the second scan $\mathrm{TE}_1 + \Delta\mathrm{TE}/2$. This potential cause of inaccuracy needs to be eliminated in future evaluations of this quantitative procedure. The correspondence of the quantitative values generated with this procedure to state-of-the art methods is not covered in this work, but needs to be addressed in the future.

Chapter 6

Joint reconstruction

6.1 Background

Imaging of the abdomen is often corrupted by respiratory motion-induced artifacts. One possibility to cope with this problem has already been stated in Chapter 4. A breath-hold adaptive approach is used to obtain as much consistent data as possible and reconstruct an image from the acquired amount of data. Abdominal imaging becomes even more challenging for dynamic contrast-enhanced (DCE) imaging, because of the strict time constraints due to the use of contrast agent. The patients have no time to recover from the used breath-holding regimes, especially in early phases. Furthermore, proper breath-holding becomes more difficult for some patients after contrast injection. Among these additional problems, DCE imaging has a meaningful advantage. An abdominal dynamic contrast-enhanced (DCE) examination typically consists of a series of five or more images of essentially the same anatomy. They are acquired with the same imaging parameters, FOV, and resolution during multiple breath-holds, and therefore, have much in common. The resulting images represent the same anatomy, but differ due to contrast-agent arrival and wash-out. Compressed sensing (CS) can potentially improve the temporal and spatial resolution of such image series further [53]. Different approaches for CS in dynamic imaging were previously proposed, for example low rank and sparse matrix decomposition [122]. These approaches were primarily tailored to dynamic cardiac imaging. In the following, a joint reconstruction of abdominal DCE images is proposed.

6.2 Reconstruction

In abdominal DCE imaging, a series of 3D image data are acquired, while the imaging parameters remain unchanged. Nevertheless, the images show temporal evolution that has mainly two reasons. The first cause of change is motion. The data are acquired in multiple breath-holds, which are potentially not at the same breath-hold position every time. As a first approximation, this motion is neglected. The second cause of change, next to motion, is the injection of contrast agent. The contrast-agent injection intentionally causes a wash-in of contrast agent shortly after injection and slower wash-out, changing overall contrast based on the amount of contrast media present in the different tissues. The contrast is monitored during all temporal phases, and the temporal behavior is used for differential diagnosis.

Apart from the unaltered anatomy, it is known that the contrast agent leaves the fat signal unchanged. This can be used in the reconstruction as prior knowledge. The reconstruction is normally formulated as a constrained optimization problem. The prior knowledge can be incorporated in the reconstruction as an additional constraint that is formulated as a joint sparsity of the 3D image data from different temporal phases. The modified minimization problem is incorporated in a reconstruction that is called ℓ_1-ESPIRiT [52]. ESPIRiT is divided into two reconstruction steps that are described in the following.

First, coil sensitivity maps are calculated from a fully sampled central k-space region. The data from the central k-space are stored in the calibration matrix $\boldsymbol{A}$ in a special form. Each row of $\boldsymbol{A}$ contains the calibration data from a block running throughout the fully sampled region as a sliding window. The calibration consistency can be written as

$$\boldsymbol{W}\boldsymbol{f} = \boldsymbol{f} \tag{6.1}$$

with the operator $\boldsymbol{W}$ that mainly consists of the vectors spanning the row space of $\boldsymbol{A}$. These vectors are calculated by an SVD of $\boldsymbol{A}$. The equation indicates that $\boldsymbol{f}$ is an eigenvector of $\boldsymbol{W}$ with eigenvalue 1. The k-space data $\boldsymbol{f}$ can be written in terms of the original image $\boldsymbol{\rho}$ weighted with coil sensitivities $\boldsymbol{S}$

$$\boldsymbol{f} = \boldsymbol{F}\boldsymbol{S}\boldsymbol{\rho} \tag{6.2}$$

with the Fourier transform operator $\boldsymbol{F}$, and can be used to reformulate the eigenvalue problem in (6.1) for each location in image space

$$\boldsymbol{F}^{-1}\boldsymbol{W}\boldsymbol{F}\boldsymbol{S}\boldsymbol{\rho} = \boldsymbol{S}\boldsymbol{\rho}. \tag{6.3}$$

The coil sensitivity maps correspond to the eigenvectors with eigenvalue one. Because of imperfections in the acquisition, in some cases, one set of coil sensitivity maps is not sufficient. This corresponds to multiple eigenvectors to eigenvalue one or slightly smaller than one.

The second step is the reconstruction. The coil sensitivity maps can be used in the reconstruction step to achieve images via a SENSE reconstruction. The incorporation of multiple sets of coil sensitivity maps in the reconstruction is called ”soft” SENSE [52] and requires a reformulation of the signal:

$$f_i = \boldsymbol{P}\boldsymbol{F}\sum_{j=1}^{M}\boldsymbol{S}_i^j\boldsymbol{\rho}^j. \tag{6.4}$$

The k-space data vector is denoted by $\boldsymbol{f}$, while $\boldsymbol{P}$ is the undersampling operator. The index j counts through the set of images and the corresponding coil sensitivity maps. Several images $\boldsymbol{\rho}^j$ result at once from a least-squares solution of (6.4).

The minimization functions for CS applications solved with ESPIRiT contain at least a data consistency term. The extension with a sparsity-enforcing term was proposed in [52] and is called ℓ_1-ESPIRiT. This sparsity-enforcing term is modified in this work to incorporate all temporal phases of the DCE acquisition instead of only one and results in the minimization function

$$\min_{\boldsymbol{\rho}}\sum_i\left\|\left|f_i - \boldsymbol{P}\boldsymbol{F}\sum_j\boldsymbol{S}_i^j\boldsymbol{\rho}^j\right|\right\|_2^2 + \alpha\sum_j\left\|\left|\sqrt{\sum_k\beta_k|\boldsymbol{\Psi}\boldsymbol{\rho}_k^j|^2}\right|\right\|_1^2. \tag{6.5}$$

The first term corresponds to (6.4), while the second term enforces sparsity and is weighted with the regularization parameter α. The squared weighted sum of the sparsified (transform $\boldsymbol{\Psi}$) temporal phases is taken. The weighting β can be used to give more importance to the temporal phase with higher reliability. Most probable, this will be the data that are acquired before contrast-agent injection, because of minor imposed time constraints. The squared sum can potentially help to recover coefficients that would be

lost in the incoherent aliasing with separate reconstruction. In that way, some redundant information becomes accessible due to the entire measurement and can be used to improve final reconstruction quality. The method is insensitive to slight disturbances, because the influence of the temporal phases on each other is indirect and not strict. The reconstruction is implemented in Matlab and was modified to reconstruct 3D data sets with the joint sparsity-enforcing constraint.

6.3 Phantom simulation

Initial experiments are performed on simulated phantom data using Matlab. While covering the same geometric objects, the phantom images are generated with different gray-scale values in some regions to simulate contrast enhancement in the liver and the arteries. The images are multiplied in image space with artificial coil sensitivities to simulate six receive channels. Afterwards, the images are Fourier transformed and undersampled in k-space with varying undersampling factors. A variable-density Poisson-disk sampling-pattern described in Chapter 3 is used. Additionally, the central k-space is fully sampled to allow the calculation of sensitivity maps from these regions. Both datasets are reconstructed with the joint approach and separately for comparison.

6.3.1 Simulations without disturbance

The procedure described before is performed on the images shown in Figure 6.1(a,b). The image in (a) imitates an axial slice from an abdominal MRI scan with organs of different size before contrast injection. Image (b) imitates the same scan after contrast injection, which is indicated by changing contrast in some regions. The contrast agent only changes contrast in locations with water-containing voxels. The part of the abdomen only containing fat is unaffected by the contrast injection. The images are Fourier transformed and the post-contrast data is undersampled with a variable-density Poisson-disk distribution of samples. The reduction factor differs for the individual images, $R_{\text{post}} = 8$ in (c,d) and $R_{\text{post}} = 16$ in (e,f). The data is reconstructed using ℓ_1-ESPIRiT (c,e) and Joint ℓ_1-ESPIRiT (d,f). Reconstruction results are clearly improved with the joint reconstruction for high reduction factors. The pre-contrast scan is fully sampled in this case without any disturbance and therefore quite reliable. The weighting β was therefore chosen rather extreme, $\beta_1 = \frac{50}{51}$ and $\beta_2 = \frac{1}{50}$. The influence of the

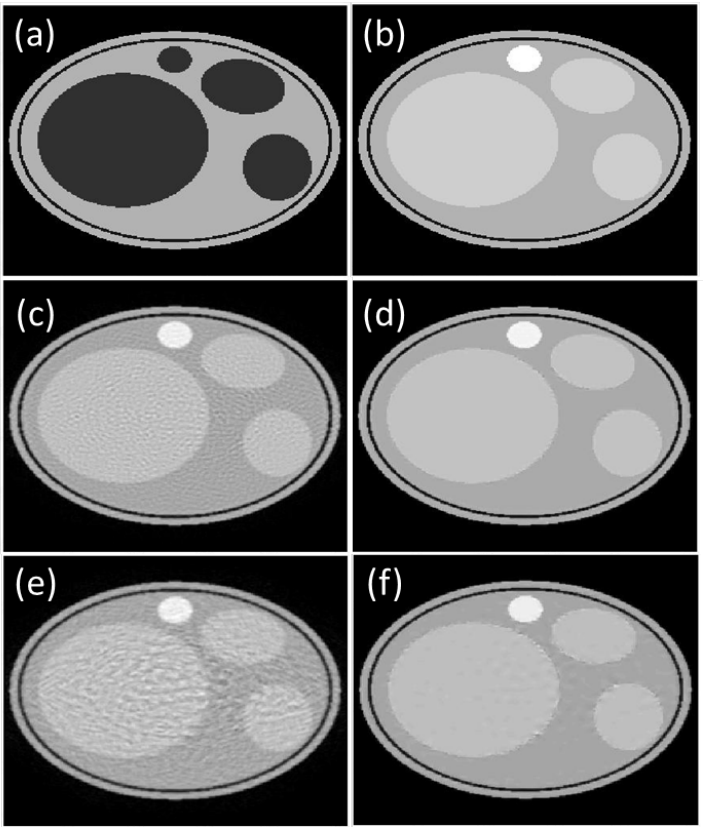

Figure 6.1: Joint reconstruction of simulated DCE phantom. In (a,b) fully sampled phantom data are shown. The image in (a) mimics the abdomen before contrast injection, while the image in (b) is used as post-contrast image. In (c,d) reconstructed post-contrast images are shown for $R = 8$ and reconstructed using (c) ℓ_1-ESPIRiT, and (d) Joint ℓ_1-ESPIRiT. In (e,f) post-contrast images are shown with $R = 16$, reconstructed using (e) ℓ_1-ESPIRiT, and (f) Joint ℓ_1-ESPIRiT. Improved reconstruction results are obtained for high reduction factors, while a separate reconstruction is sufficient for low reduction factors.

quality of the pre-contrast scan on the joint reconstruction is evaluated by varying the reduction factors R_{pre} and calculating the normalized RMSE e according to

$$e = \frac{\sqrt{\frac{1}{N}\sum_{i=1}^{N} |\rho_i - \rho_{\text{ref},i}|^2}}{\max_i |\rho_{\text{ref},i}|}, \tag{6.6}$$

with the fully sampled reference image ρ_{ref}. The RMSE is calculated in image space and is summarized in Table 6.1. The joint reconstruction consistently results in a lower error for all combinations of R_{pre} and R_{post} compared with separate reconstruction. As expected, the errors become worse for increasing R_{pre}. The same tendency is visible for increasing R_{post}. The sparsity of the phantom data is quite high, which constitutes the high achievable reduction factors. In the examples shown here, only the influence of the joint reconstruction on the post-contrast images is studied. Nevertheless, the results are

Table 6.1: Joint reconstruction: RMSE calculated according to (6.6) for $R_{\text{post}} = 4$ and $R_{\text{post}} = 8$. For comparison the post contrast images were reconstructed with the separate reconstruction (ℓ_1-ESPIRiT) as well and the RMSE calculated. For the joint reconstruction a dependence on the reduction factor $R_{\text{pre}} = 1, 2, 4, 8$ of the reference pre-contrast image is visible. The RMSE is reduced for the joint approach compared to the separate reconstruction.

Recon-struction	R_{post}	R_{pre}	RMSE of $\rho_2(\%)$
ℓ_1-ESPIRiT	4	/	3.78
Joint-ℓ_1-ESPIRiT		1	3.11
		2	3.48
		4	3.66
		8	3.54
ℓ_1-ESPIRiT	8	/	6.37
Joint-ℓ_1-ESPIRiT		1	4.16
		2	4.47
		4	4.77
		8	5.72

equally applicable to the reverse case, the pre-contrast data can benefit from the post-contrast data. The focus here is on the post-contrast data, because these data tend to be prone to incomplete breath-holds more strongly than the pre-contrast data. It needs to be stated clearly that the benefit of the joint approach is not fully exploited here. The examples are based on a set of data with two temporal phases, while a DCE examination contains at least four temporal phases. In real MRI data, the sparsity is lower, noise is present, and motion can potentially occur. The influence of the latter two is simulated in the phantom data in the following.

6.3.2 Additional noise

The results shown so far indicate better reconstruction results for the joint reconstruction. Under MRI experimental conditions, the signal is prone to different types of imperfections, like non-steady state of signal, noise, motion, eddy currents. The influence of noise is studied here. Gaussian noise with mean $\mu = 0$ and variance σ^2 was added to the pre- and post-contrast data. The noise was generated for every single experiment independently, and therefore, differs for the varying reduction factors. The RMSE of the reconstruction result, calculated according to (6.6), without noise is calculated and

Table 6.2: Joint reconstruction: RMSE calculated according to (6.6) for the post contrast result given for varying R_{pre} and R_{post}. Normal distributed noise with mean $\mu = 0$ and variance $\sigma^2 = 0.01$ was added to the pre- and post-contrast phantom data. For comparison the post contrast images were reconstructed with the separate reconstruction (ℓ_1-ESPIRiT) as well and the RMSE calculated. The dependence on the reduction factor R_{pre} of reference pre-contrast image is visible with reduced RMSE for the joint approach.

Reconstruction	R_{post}	R_{pre}	RMSE of $\rho_2(\%)$	Reconstruction	R_{post}	R_{pre}	RMSE of $\rho_2(\%)$
ℓ_1-ESPIRiT	2	/	3.57	ℓ_1-ESPIRiT	6	/	4.57
Joint-ℓ_1-ESPIRiT		1	2.99	Joint-ℓ_1-ESPIRiT		1	3.66
		2	3.54			2	4.27
		4	3.56			4	4.25
		6	3.55			6	4.2
		8	3.35			8	4.23
ℓ_1-ESPIRiT	4	/	4.55	ℓ_1-ESPIRiT	8	/	5.29
Joint-ℓ_1-ESPIRiT		1	3.69	Joint-ℓ_1-ESPIRiT		1	4.3
		2	3.99			2	4.44
		4	3.95			4	4.49
		6	4.0			6	4.69
		8	3.96			8	5.0

summarized in Table 6.2 for $\sigma^2 = 0.01$. The absolute gray-scale values of the original images are scaled to the interval $[0, 1]$.

The weighting β needs to be chosen adequately based on the expected consistency and artifacts in the images. Because the pre-contrast data is potentially of degraded image quality due to the added noise in these cases, the weighting β is modified for these experiments, $\beta_1 = 0.1$ and $\beta_2 = 0.9$. The benefit of the joint reconstruction is not as apparent as without noise. However, for $R_{\text{pre}} = 1$, the joint reconstruction is still consistently improved compared to the separate reconstruction. This changes slightly for $R_{\text{pre}} = 2$, where improvements are only visible for $R_{\text{post}} \geq 4$. The separate reconstruction is able to cope with $R = 2$ itself, a prior knowledge with comparable artifacts helps only slightly. This behavior stays the same for $R_{\text{pre}} > 2$ and $R_{\text{post}} = 2$. Some improvements are still apparent for larger R_{post}.

The experiments were repeated with a higher noise level, $\sigma^2 = 0.05$. The results are summarized in Table 6.3 indicating an even lower benefit for the joint reconstruction. The dependence of the RMSE on the reduction factor R_{pre} is lowered. Potentially, the

Table 6.3: Joint reconstruction: RMSE calculated according to (6.6) for the post contrast result given for varying R_{pre} and R_{post}. Normal distributed noise with mean $\mu = 0$ and variance $\sigma^2 = 0.05$ was added to the pre- and post-contrast phantom data. For comparison, the post contrast images were reconstructed with the separate reconstruction (ℓ_1-ESPIRiT) as well and the RMSE calculated. The dependence on reduction factor of reference pre-contrast image is becoming lower, because the additional noise is inducing large errors already.

Reconstruction	R_{post}	R_{pre}	RMSE of $\rho_2(\%)$	Reconstruction	R_{post}	R_{pre}	RMSE of $\rho_2(\%)$
ℓ_1-ESPIRiT	2	/	4.77	ℓ_1-ESPIRiT	6	/	6.67
Joint-ℓ_1-ESPIRiT		1	4.42	Joint-ℓ_1-ESPIRiT		1	4.88
		2	4.86			2	5.22
		4	4.62			4	5.24
		6	5.31			6	5.56
		8	4.43			8	5.73
ℓ_1-ESPIRiT	4	/	6.32	ℓ_1-ESPIRiT	8	/	6.58
Joint-ℓ_1-ESPIRiT		1	5.18	Joint-ℓ_1-ESPIRiT		1	5.48
		2	5.97			2	5.75
		4	4.97			4	5.41
		6	6.46			6	5.91
		8	5.52			8	5.92

noise level is of the same order as the incoherent aliasing from undersampling or even higher.

6.3.3 Influence of motion

Another cause of experimental imperfections is a potential misalignment due to motion. Because the images are acquired during a series of breath-holds, it is often difficult to achieve exactly the same breath-hold position in every individual breath-hold. The influence of motion is simulated here by a translation of the pre-contrast image. Some other rigid or affine transformation could be performed alternatively to evaluate the influence of motion. A translation of two pixels in one direction was performed on the pre-contrast data in image space. The RMSE of the reconstruction results of the post-contrast data, calculated according to (6.6), were calculated and are summarized in Table 6.4. The results are consistent with the ones from the simulations with noise. For a reduction factor of $R_{\text{post}} = 2$, the separate reconstruction is sufficient. Prior knowledge that is prone to inconsistencies worsens the reconstruction. The benefit of

Table 6.4: Joint reconstruction: RMSE calculated according to (6.6) for the post contrast result for varying R_{pre} and R_{post}. A shift of two pixels in one direction was applied to simulate slight motion. For comparison the post contrast images were reconstructed with the separate reconstruction (ℓ_1-ESPIRiT) as well and the RMSE calculated. Dependence on reduction factor R_{pre} of reference pre-contrast image is visible with reduced RMSE for the joint approach compared to separate reconstruction.

Reconstruction	R_{post}	R_{pre}	RMSE of $\rho_2(\%)$	Reconstruction	R_{post}	R_{pre}	RMSE of $\rho_2(\%)$
ℓ_1-ESPIRiT	2	/	3.61	ℓ_1-ESPIRiT	6	/	4.53
Joint-ℓ_1-ESPIRiT		1	3.74	Joint-ℓ_1-ESPIRiT		1	3.85
		2	3.78			2	3.88
		4	3.61			4	4.0
		6	3.51			6	4.06
		8	3.46			8	4.11
ℓ_1-ESPIRiT	4	/	4.25	ℓ_1-ESPIRiT	8	/	5.28
Joint-ℓ_1-ESPIRiT		1	3.82	Joint-ℓ_1-ESPIRiT		1	4.69
		2	3.9			2	4.57
		4	3.93			4	4.74
		6	3.8			6	4.85
		8	3.91			8	4.93

the joint reconstruction is based on the assumption that the same wavelet coefficients are large for the differing temporal phases. Exactly this assumption is violated for motion between the temporal phases. For higher reduction factors, the situation becomes different. There is some benefit for the joint reconstruction, although the rigid-body motion-model was not taken into account in the signal model and the corresponding reconstruction problem given in (6.5). It is further visible that slight motion has a larger impact on the RMSE than slightly increased noise.

The experiments were repeated for a large translation of five pixels. The corresponding RMSE (6.6) of the reconstruction results are given in Table 6.5 and indicate degraded results for small R_{post} and slight improvement for larger R_{post} compared to separate reconstruction (ℓ_1-ESPIRiT). A motion correction needs to be included in the minimization problem to achieve better reconstruction results with the joint approach.

The influence of the choice of the weighting β needs to be evaluated further. In the case of disturbances, an equal weighting of the temporal phases can potentially lead to better results for small reduction factors, because inconsistencies have a lower impact on the post-contrast images.

Table 6.5: Joint reconstruction: RMSE calculated according to (6.6) for the post contrast result for varying R_{pre} and R_{post}. A shift of five pixels in both directions was applied to simulate stronger motion. For comparison the post contrast images were reconstructed with the separate reconstruction (ℓ_1-ESPIRiT) as well and the RMSE calculated. The dependence on reduction factor R_{pre} of reference pre-contrast image is visible. For low reduction factors R_{post} the RMSE error is increased for the joint reconstruction compared to separate reconstruction. The situation is reversed for higher reduction factors R_{post}.

Reconstruction	R_{post}	R_{pre}	RMSE of $\rho_2(\%)$	Reconstruction	R_{post}	R_{pre}	RMSE of $\rho_2(\%)$
ℓ_1-ESPIRiT	2	/	3.61	ℓ_1-ESPIRiT	6	/	4.53
Joint-ℓ_1-ESPIRiT		1	3.93	Joint-ℓ_1-ESPIRiT		1	4.42
		2	3.7			2	4.37
		4	3.64			4	4.24
		6	3.63			6	4.3
		8	3.64			8	4.33
ℓ_1-ESPIRiT	4	/	4.25	ℓ_1-ESPIRiT	8	/	5.28
Joint-ℓ_1-ESPIRiT		1	4.44	Joint-ℓ_1-ESPIRiT		1	4.45
		2	4.22			2	4.69
		4	4.01			4	4.9
		6	4.02			6	5.05
		8	4.04			8	5.03

6.4 In vivo experiments

Experiments on healthy volunteers were performed on a 3 T scanner (Philips Healthcare, Best, The Netherlands) with a 3D T1-weighted spoiled dual-gradient-echo sequence. The flip angle was $10°$, $\text{TE}_1/\text{TE}_2/\text{TR}$ were $1.3/2.3/3.7$ ms, data were acquired using bipolar gradients with a pixel bandwidth of 1322 Hz, the FOV was about $375 \times 240 \times 230$ mm^3, and the target actual spatial resolution was $1.5 \times 1.5 \times 3$ mm^3, covering the whole abdomen. Data were measured with the adaptive sampling-pattern described in Chapter 4 that implies lower resolution for shorter breath-holds. This is not optimal for the joint reconstruction described before, because improvements are expected for high incoherent aliasing, which is not achieved with the sampling-patterns optimized for separate reconstruction. Nevertheless, some volunteer data with long breath-hold durations, for which the target resolution was achieved, can be used. The post-contrast data were further undersampled retrospectively to achieve more uniform undersampling patterns. In this way, shorter breath-holds during data acquisition were

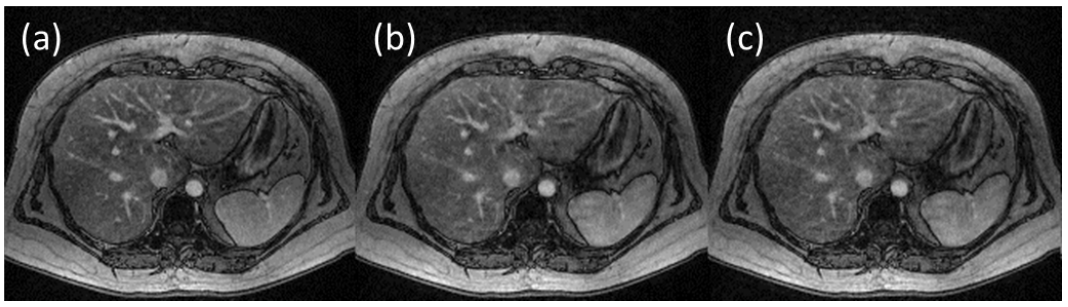

Figure 6.2: Comparison of individual and joint reconstruction. The image in (a) is reconstructed with individual ESPIRiT from the longest available breath-hold. The data for the reconstructed images (b,c) were further undersampled to obtain a reduction factor of 6,6 to simulate shorter breath-holds. The image in (b) was reconstructed using ℓ_1-ESPIRiT, while (c) was reconstructed using Joint-ESPIRiT. The images in (b,c) are comparable in image quality.

simulated, and the data were reconstructed with the joint reconstruction. For comparison, same data were reconstructed with each temporal phase individually. As a reference, the separate reconstruction was also performed on the longest available breath-hold.

The reconstruction was modified to handle 3D data. Slices were reconstructed in parallel to reduce reconstruction times. Images of the first echo from on selected volunteer are shown in Figure 6.2. The reconstruction result from the longest breath-hold is shown in (a) for reference. An individual reconstruction of the temporal phases from short breath-hold duration is given in (b) and joint reconstruction in (c). The data were undersampled by an undersampling factor of 6.6. The images (b) and (c) are comparable in image quality, with a RMSE, calculated according to (6.6), of 3.04% for the individual reconstruction and 2.84% for the joint reconstruction and thus slightly improved for the joint reconstruction. The reconstructed image from the longest available breath-hold was used as ground-truth here, because fully sampled data are not available.

6.5 Discussion

Phantom simulations indicate superior reconstruction results for the joint reconstruction of pre- and post-contrast images compared with separate ℓ_1-ESPIRiT reconstruction if the images perfectly correspond to each other. This means that no motion occurred between the two temporal phases, and there is no noise in the images. If the undersampling factors of the two temporal phases are different, the phase with fewer samples

clearly benefits from the joint reconstruction.

The situation changes for the phantom simulations with noise or motion, because the reliability becomes lower and the improvement of the joint reconstruction compared with the separate reconstruction less obvious. For a reduction factor of $R = 2$, the separate reconstruction gives good results. Incorporating the second temporal phase gives hardly any improvement, because the quality of the additional knowledge is degraded due to noise or motion and not better than the first image. For higher reduction factors R_{post}, the separate reconstruction gives results with higher artifacts due to undersampling. The lowered reliability of the second scan, compared to the first scan, thus induces lower artifacts than the higher undersampling factor, and the joint reconstruction gives slightly improved results. This is not the case for large motion between the phases. The joint reconstruction partially gives worse results than the separate reconstruction or hardly any improvement. It is thus stated that a joint reconstruction can give clearly better results for high reliability of the temporal phases. If motion occurs, a motion correction is essential.

For in vivo data, the error relative to the 27 s post-contrast scan is only slightly reduced for the joint reconstruction. The improvement is strongly dependent on the quality of the pre-contrast image and the geometric alignment of the phases. Furthermore, the phantom simulations indicate that the joint approach is especially helpful in extreme cases, where separate sparsity fails. Larger improvement for in vivo data is expected for higher undersampling. This work shows that joint approaches can potentially improve image quality in DCE abdominal imaging in patients with insufficient breath-hold capability. If the geometric alignment is insufficient, a motion correction needs to be performed.

Chapter 7

Conclusion

MRI is a non-invasive imaging technique with clear advantages over other imaging modalities, but also one major disadvantage: long imaging times. A lot of development effort has been invested in the recent years to accelerate the acquisition. One of these promising methods is compressed sensing (CS). Apart from a general CS sampling pattern, this thesis does not only aim at maximum possible scan acceleration, but proposes the application of CS for the achievement of more robustness in abdominal MRI.

The theoretical impact of this thesis is the design of optimized compressed sensing sampling patterns in general and sampling patterns with a focus on abdominal applications. The incoherent sampling pattern, which uses a fixed reduction factor, is not specifically designed for abdominal imaging. It is a more general approach that enables a fast generation of Poisson disk sampling distributions with arbitrary variable density functions. Incoherence is ensured, while clustering and large holes are prevented successfully. The low computational cost makes generation directly on the scanner possible. With the choice of the variable density function, it is possible to adopt the sampling pattern to the requirements of several clinical application. Although the variable densities shown here are constant or decaying with the distance to the k-space center, this is not mandatory. The variable densities are arbitrary and can thus have e.g. multiple maxima in k-space or increasing density towards the periphery. While the sampling-pattern generator provides sufficient freedom for the choice of the variable density, the optimal sampling density for a combined compressed sensing and parallel imaging reconstruction is not discussed here in case of 3D head or abdominal imaging and needs to be investigated in the future. It is argued that the sampling density should decay with distance to k-space center due to the increased sparsity of finer wavelet scales that are represented

by coefficients in the periphery of k-space. This is relatively compelling for pure CS reconstruction, but not necessarily optimal for parallel imaging, because the sampling density in the periphery is reduced and potentially lower than the lower bound required for artifact-free parallel imaging reconstruction. Once this variable density is found, the sampling-pattern generator is able to generate corresponding sampling patterns for 1D and 2D undersampling.

In this thesis, a method is proposed to attain an increased robustness in 3D abdominal imaging by applying compressed sensing and a flexible sampling scheme to abdominal MRI. The sampling pattern increases the resolution automatically during the scan and ensures incoherence at any time during acquisition. This enables arbitrary scan termination at breathing-onset and compressed sensing reconstruction from consistent data. Shorter breath-holds are compromised with lowered resolution, but motion artifacts are prevented in the reconstructed images for any breath-hold duration respiratory. The breath-hold adaptive sampling pattern preserves the benefits of breath-holding, while suppressing motion artifacts induced by premature breathing onset. The method was successfully applied to 3D gradient-echo imaging of the abdomen and extended to dual-echo imaging for water-fat separation. Furthermore, the adaptive sampling pattern was applied to dual-contrast imaging within one breath-hold using a sequence switching approach that enables switching between scans almost immediately. In this way, geometrically consistent data, providing two contrasts, are obtained by exploiting the individual breath-hold duration with the adaptive sampling pattern.

The sampling pattern was applied successfully to dynamic contrast enhanced imaging that is typically prone to motion artifacts because of the time constraints of the imaging series. The reconstruction results are promising for all examined applications, but further research has to be done on one of the used navigators to obtain reliable breath-holding information even for dynamic contrast-enhanced imaging of the abdomen. This is challenging because of two reasons. The evaluation of the navigator in examinations on volunteers is reliable, because the volunteers are experienced. In clinical practice, however, the ability of patients to follow breath-holding instructions is limited, and the evaluation of the navigator signal is thus quite challenging. Furthermore, the intended contrast change during an individual scan induced by contrast-agent injection has to be separated from changing signal due to respiratory motion. One concept is shown in this work that was tested on one of the late phases of the imaging series. Nevertheless, evaluation is also crucial for the early phases. This needs to be done in the future, because

these phases are the most critical temporal phases with highest contrast change. Along this line, the sampling pattern has to be evaluated on the other temporal phases of a dynamic contrast-enhanced imaging series.

The images from a dynamic contrast-enhanced examination have quite some information in common. This knowledge was exploited in this thesis by a weighted joint reconstruction of the temporal phases. The experiments on phantom data consistently indicate better reconstruction results than separate reconstruction in case of perfect spatial correspondence and without noise. The image quality of the joint reconstruction and separate reconstruction is comparable with slightly reduced errors for the joint approach. As a next step, an included motion correction could help in obtaining better results, but apart from that, it is obvious that two phases cannot have a tremendous impact. The inclusion of more temporal phases is potentially promising.

The method was extended in this thesis to multi-echo imaging for a water-fat separation with high accuracy. This sequence was used for a new application to improve quantitative MRI. The fat fraction of the entire liver was estimated using the adaptive sampling pattern to obtain maps without motion artifacts to increase accuracy. Although improvement is visible in the images, questions remain to be answered in the future. A signal change during image acquisition leads to severe artifacts in the adaptive sampling approach compared with a linear sampling approach, because spatially closed profiles in k-space are not acquired in a temporally closed fashion. The adaptive sampling pattern is thus only partly applicable to signals not in the steady state. Apart from the approach to the steady-state, the echoes varied significantly in image quality with a tendency to a decreased image quality for later echoes. Thus, the required number of six echoes were acquired separately in two scans of three echoes with a sequence switching approach that enables switching between the scans with hardly any delay. This effectively reduces the echo spacing and the artifacts in the image to a comparable image quality with respect to a linear sampling. The artifacts are not completely removed, and further research needs to be done on this topic.

Starting from a general sampling pattern for compressed sensing in MRI, a sampling pattern is proposed for abdominal imaging that increases patient comfort. The abdominal imaging procedures, presented in this thesis, offer a promising and realistic clinical application of compressed sensing to MRI with the aim to improve image quality and robustness in 3D abdominal imaging.

Bibliography

[1] E M Haacke, R W Brown, M R Thompson, and R Venkatesan. *Magnetic Resonance Imaging: Physical Principles and Sequence Design*. Wiley, 1999.

[2] M T Vlaardingerbroek and J A Boer. *Magnetic Resonance Imaging: Theory and Practice*. Physics and astronomy online library. Springer, 2003.

[3] P C Lauterbur. Image formation by induced local interactions: examples employing nuclear magnetic resonance. *Nature*, 242:190–191, 1973.

[4] M Hutchinson and U Raff. Fast MRI data acquisition using multiple detectors. *Magnetic Resonance in Medicine*, 6:87–91, 1988.

[5] J R Kelton, R L Magin, and S M Wright. An algorithm for rapid image acquisition using multiple receiver coils. In *Proceedings of the 8th Annual meeting of the ISMRM*, page 1172, 1989.

[6] D Twieg. The k-trajectory formulation of the NMR imaging porcess with applications in analysis and synthesis of imaging methods. *Medical physics*, 10:610–621, 1983.

[7] S Ljunggren. A simple graphical representation of Fourier-based imaging methods. *Journal of Magnetic Resonance Imaging*, 54:338–343, 1983.

[8] K P Pruessmann, M Weiger, M B Scheidegger, and P Boesiger. SENSE: Sensitivity encoding for fast MRI. *Magnetic Resonance in Medicine*, 42:952–962, 1999.

[9] M A Griswold, P M Jakob, R M Heidemann, M Nittka, V Jellus, J Wang, B Kiefer, and A Haase. Generalized autocalibrating partially parallel acquisitions (GRAPPA). *Magnetic Resonance in Medicine*, 47:1202–1210, 2002.

[10] R M Heidemann, M A Griswold, R R Edelmann, A Haase, and P M Jakob. VD-AUTO-SMASH imaging. *Magnetic Resonance in Medicine*, 45:1066–1074, 2001.

[11] D K Sodickson and W J Manning. Simultaneous acquisition of spatial harmonics (SMASH): Fast imaging with radiofrequency coil arrays. *Magnetic Resonance in Medicine*, 38(4):591–603, 1997.

[12] M A Griswold, P M Jakob, M Nittka, J W Goldfarb, and A Haase. Partially parallel imaging with localized sensitivities (PILS). *Magnetic Resonance in Medicine*, 44:602–609, 2000.

[13] P B Roemer, W A Edelstein, C E Hayes, S P Souza, and O M Mueller. The NMR phased array. *Magnetic Resonance in Medicine*, 16:192–225, 1990.

[14] E H Moore. On the reciprocal of the general algebraic matrix. *Bulletin of the American Mathematical Society*, 26:394–395, 1920.

[15] M Buehrer, K P Pruessmann, P Boesiger, and S Kozerke. Array compression for MRI with large coil arrays. *Magnetic Resonance in Medicine*, 57:1131–1139, 2007.

[16] F Huang, S Vijayakumar, Y Li, S Hertel, and G Duensing. A software channel compression technique for faster reconstruction with many channels. *Magnetic Resonance in Medicine*, 26:133–141, 2008.

[17] S King, S Varosi, and G Duensing. Optimum SNR data compression in hardware using an eigencoil array. *Magnetic Resonance in Medicine*, 63:1346–1356, 2010.

[18] S King and G Duensing. The MRI Eigencoil: 2N-channel SNR with N-Receivers. In *Proceedings of the 11th Annual meeting of the ISMRM*, page 712, 2003.

[19] M Doneva and P Börnert. Automatic coil selection for channel reduction in SENSE-based parallel imaging. *Magnetic Resonance Materials in Physics, Biology and Medicine*, 21:187–196, 2008.

[20] S Feng, Y Zhu, and J Ji. Efficient large-array k-domain parallel MRI using channel-by-channel array reduction. *Magnetic Resonance Imaging*, 29:209–215, 2011.

[21] P Beatty, J Holmes, S Chang, E Bayram, J Brittain, S Reeder, and A C S Brau. Coil-by-coil vs. direct virtual coil (DVC) parallel imaging reconstruction: an image quality comparison for contrast-enhanced liver imaging. In *Proceedings of the 18 th Annual meeting of the ISMRM*, page 2879, 2010.

[22] T Zhang, J M Pauly, S S Vasanawala, and M Lustig. Coil compression for accelerated imaging with Cartesian sampling. *Magnetic Resonance in Medicine*, 69:571–582, 2013.

[23] M Lustig, D L Donoho, and J M Pauly. Sparse MRI: The application of compressed sensing for rapid MR imaging. *Magnetic Resonance in Medicine*, 58:1182–1195, 2007.

[24] S S Vasanawala, M T Alley, B A Hargreaves, R A Barth, J M Pauly, and M Lustig. Improved pediatric MR imaging with compressed sensing. *Radiology*, 256:607–616, 2010.

[25] M Murphy, M Alley, J Demmel, K Keutzer, S Vasanawala, and M Lustig. Fast l1-SPIRiT compressed sensing parallel imaging MRI: Scalable parallel implementation and clinically feasible runtime. *IEEE Transactions on Information Theory*, 31:1250–1262, 2012.

[26] M Doneva, P Börnert, H Eggers, A Mertins, J M Pauly, and M Lustig. Compressed sensing for chemical shift-based water-fat separation. *Magnetic Resonance in Medicine*, 64:1749–1759, 2010.

[27] S D Sharma, H H Hu, and K S Nayak. Accelerated water-fat imaging using restricted subspace field map estimation and compressed sensing. *Magnetic Resonance in Medicine*, 67:650–659, 2011.

[28] C N Wiens, C M McCurdy, J D Willig-Onwuachi, and C A McKenzie. R2*-corrected water–fat imaging using compressed sensing and parallel imaging. *Magnetic Resonance in Medicine*, 71:608–616, 2014.

[29] D L Donoho. Compressed Sensing. *IEEE Transactions on Information Theory*, 52:1289–1306, 2006.

[30] E Candes, J Romberg, and T Tao. Robust uncertainty principles: Exact recovery from highly incomplete Fourier information. *IEEE Transactions on Information Theory*, 52:489–509, 2006.

[31] J I Yellott. Spectral consequences of photoreceptor sampling in the rhesus retina. *Science*, 221(4608):382–385, 1983.

[32] M McCool and E Fiume. Hierarchical Poisson disk sampling distributions. *Graphics interface*, pages 94–105, 1992.

[33] S Mallat and Z Zhang. Matching pursuits with time-frequancy dictionaries. *IEEE Transactions on Signal Processing*, 41:3397–3415, 1993.

[34] J Tropp and A Gilbert. Signal recovery from random measurements via orthogonal matching pursuit. *IEEE Transactions on Information Theory*, 53:4655, 2007.

[35] D Needell and J Tropp. CoSaMP: Iterative signal recovery from incomplete and inaccurate samples. *Applied and Computational Harmonic Analysis*, 26:301–321, 2009.

[36] S Chen, D Donoho, and M Saunders. Atomic decomposition by basis pursuit. *SIAM review*, 43:129–159, 2001.

[37] R Tibshirani. Regression shrinkage and selection via the lasso. *Journal of the Royal Statistical Society. Series B (Methodological)*, 58:267–288, 1996.

[38] T Blumensath and M Davies. Iterative hard thresholding for compressed sensing. *Applied and Computational Harmonic Analysis*, 27:265–274, 2009.

[39] D Donoho. De-noising by soft-thresholding. *IEEE Transactions on Information Theory*, 41:613–627, 2002.

[40] D Donoho, A Maleki, and A Montanari. Message-passing algorithms for compressed sensing. 106(45):18914, 2009.

[41] D Baron, S Sarvotham, and R Baraniuk. Bayesian compressive sensing via belief propagation. *IEEE Transactions on Signal Processing*, 58(1):269–280, 2009.

[42] P Indyk and M Ruzic. Near-optimal sparse recovery in the l1 norm. In *IEEE 49th Annual IEEE Symposium on Foundations of Computer Science*, pages 199–207, 2008.

[43] R Berinde, P Indyk, and M Ruzic. Practical near-optimal sparse recovery in the l1 norm. In *2008 46th Annual Allerton Conference on Communication, Control, and Computing*, pages 198–205. IEEE, 2009.

[44] R Berinde and P Indyk. Sequential sparse matching pursuit. In *2009 47th Annual Allerton Conference on Communication, Control, and Computing*, pages 36–43. IEEE, 2010.

[45] A Beck and M Teboulle. A Fast Iterative Shrinkage-Thresholding Algorithm for Linear Inverse Problems. *SIAM Journal on Imaging Sciences*, 2(1):183–202, 2009.

[46] J F Murray and K Kreutz-Delgado. An improved FOCUSS-based learning algorithm for solving sparse linear inverse problems. 1:347–351, 2001.

[47] R Chartrand and Wotao Yin. Iteratively reweighted algorithms for compressive sensing. pages 3869–3872, 2008.

[48] D P Wipf and B D Rao. Sparse Bayesian learning for basis selection. *Signal Processing, IEEE Transactions on*, 52(8):2153–2164, 2004.

[49] S J Godsill, A T Cemgil, C Févotte, and P J Wolfe. Bayesian computational methods for sparse audio and music processing. In *Prococeedings EUSIPCO*, pages 345–349, 2007.

[50] W Yin, S Osher, D Goldfarb, and J Darbon. Bregman iterative algorithms for l1-minimization with applications to compressed sensing. *SIAM Journal on Imaging Sciences*, pages 143–168, 2008.

[51] M Lustig and J M Pauly. SPIRiT: Iterative self-consistent parallel imaging reconstruction from arbitrary k-space. *Magnetic Resonance in Medicine*, 64(2):457–471, 2010.

[52] M Uecker, P Lai, M J Murphy, P Virtue, M Elad, J M Pauly, S S Vasanawala, and M Lustig. ESPIRiT - An eigenvalue approach to autocalibrating parallel MRI: Where SENSE meets GRAPPA. *Magnetic Resonance in Medicine*, 71:990–1001, 2014.

[53] U Gamper, P Boesiger, and S Kozerke. Compressed sensing in dynamic MRI. *Magnetic Resonance in Medicine*, 59:365–373, 2008.

[54] H Jung, K Sung, K S Nayak, E Y Kim, and J C Ye. k-t FOCUSS: A general compressed sensing framework for high resolution dynamic MRI. *Magnetic Resonance in Medicine*, 61(1):103–116, 2009.

[55] M Lustig, D L Donoho, and J M Pauly. Rapid MR imaging with Compressed Sensing and randomly under-sampled 3DFT trajectories. In *Proceedings of the 14th Annual Meeting of the ISMRM*, page 695, 2006.

[56] D Liang, B Liu, J Wang, and L Ying. Accelerating sense using compressed sensing. *Magnetic Resonance in Medicine*, 62(6):1574–1584, 2009.

[57] F Huang, W Lin, GR Duensing, and A Reykowski. k-t sparse GROWL: Sequential combination of partially parallel imaging and compressed sensing in k-t space using flexible virtual coil. *Magnetic Resonance in Medicine*, 68(3):772–782, 2012.

[58] H She, R-R Chen, D Liang, E V R DiBella, and L Ying. Sparse BLIP: BLind Iterative Parallel imaging reconstruction using compressed sensing. *Magnetic Resonance in Medicine*, 71(2):645–660, 2014.

[59] R Otazo, D Kim, L Axel, and D K Sodickson. Combination of compressed sensing and parallel imaging for highly accelerated first-pass cardiac perfusion MRI. *Magnetic Resonance in Medicine*, 64(3):767–776, 2010.

[60] K F King. Combinig compressed sensing and parallel imaging. In *Proceedings of the 16th Annual Meeting of the ISMRM*, page 1488, 2008.

[61] F Huang, Y Chen, W Yin, W Lin, X Ye, W Guo, and A Reykowski. A rapid and robust numerical algorithm for sensitivity encoding with sparsity constraints: Self-feeding sparse SENSE. *Magnetic Resonance in Medicine*, 64(4):1078–1088, 2010.

[62] B Wu, R P Millane, R Watts, and P J Bones. Prior estimate-based compressed sensing in parallel MRI. *Magnetic Resonance in Medicine*, 65(1):83–95, 2011.

[63] P Kellman, F H Epstein, and E R McVeigh. Adaptive sensitivity encoding incorporating temporal filtering (TSENSE). *Magnetic Resonance in Medicine*, 45(5):846–852, 2001.

[64] M Lustig, J M Santos, D L Donoho, and J M Pauly. kt SPARSE: High frame rate dynamic MRI exploiting spatio-temporal sparsity. In *Proceedings of the 14th Annual Meeting of the ISMRM*, page 2420, 2006.

[65] S Rapacchi, F Han, Y Natsuaki, R Kroeker, A Plotnik, E Lehman, J Sayre, G Laub, J P Finn, and P Hu. High spatial and temporal resolution dynamic

contrast-enhanced magnetic resonance angiography using compressed sensing with magnitude image subtraction. *Magnetic Resonance in Medicine*, 2013. doi: 10.1002/mrm.24842.

[66] R M Lebel, J Jones, J-C Ferre, M Law, and K S Nayak. Highly accelerated dynamic contrast enhanced imaging. *Magnetic Resonance in Medicine*, 71(2):635–644, 2014.

[67] J D Trzasko, C R Haider, E A Borisch, N G Campeau, J F Glockner, S J Riederer, and A Manduca. Sparse-CAPR: Highly accelerated 4D CE-MRA with parallel imaging and nonconvex compressive sensing. *Magnetic Resonance in Medicine*, 66(4):1019–1032, 2011.

[68] J J Van Vaals, M E Brummer, W T Dixon, H H Tuithof, H Engels, R C Nelson, B M Gerety, J L Chezmar, and J A Den Boer. "Keyhole" method for accelerating imaging of contrast agent uptake. *Journal of Magnetic Resonance Imaging*, 3(4):671–675, 1993.

[69] R A Jones, O Haraldseth, T B Müller, P A Rinck, and A N Øksendal. K-space substitution: A novel dynamic imaging technique. *Magnetic Resonance in Medicine*, 29(6):830–834, 1993.

[70] F R Korosec, R Frayne, T M Grist, and C A Mistretta. Time-resolved contrast-enhanced 3D MR angiography. *Magnetic Resonance in Medicine*, 36(3):345–351, 1996.

[71] J Tsao, P Boesiger, and K Pruessmann. k-t BLAST and k-t SENSE: Dynamic MRI with high frame rate exploiting spatiotemporal correlations. *Magnetic Resonance in Medicine*, 50(4):1031–1042, 2003.

[72] F Huang, J Akao, S Vijayakumar, G R Duensing, and M Limkeman. k-t GRAPPA: A k-space implementation for dynamic MRI with high reduction factor. *Magnetic Resonance in Medicine*, 54(5):1172–1184, 2005.

[73] D Xu, K F King, and Z-P Liang. Improving k-t SENSE by adaptive regularization. *Magnetic Resonance in Medicine*, 57(5):918–930, 2007.

[74] Z Liang, H Jiang, C Hess, and P Lauterbur. Dynamic imaging by model estimation. *International Journal of Imaging Systems and Technology*, 8(6):551–557, 1997.

[75] Q Zhao, N Aggarwal, and Y Bresler. Dynamic imaging of time-varying objects. In *Proceedings of the 9th Annual meeting of the ISMRM*, page 1776, 2001.

[76] N Aggarwal and Y Bresler. Patient-adapted reconstruction and acquisition dynamic imaging method (PARADIGM) for MRI. *Inverse problems*, 24(4):045015, 2008.

[77] H Jung, J Park, J Yoo, and J C Ye. Radial k-t FOCUSS for high-resolution cardiac cine MRI. *Magnetic Resonance in Medicine*, 63(1):68–78, 2010.

[78] Z Liang. Spatiotemporal imaging with partially separable functions. In *4th IEEE International Symposium on Biomedical Imaging: From Nano to Macro*, pages 988–991, 2007.

[79] H Pedersen, S Kozerke, S Ringgaard, K Nehrke, and W Y Kim. k-t PCA: Temporally constrained k-t BLAST reconstruction using principal component analysis. *Magnetic Resonance in Medicine*, 62(3):706–716, 2009.

[80] I Haldar and Z Liang. Spatiotemporal imaging with partially separable functions: a matrix recovery approach. In *IEEE International Symposium on Biomedical Imaging: From Nano to Macro*, pages 716–719, 2010.

[81] S Lingala, Y Hu, E DiBella, and M Jacob. Accelerated dynamic MRI exploiting sparsity and low-rank structure: k-t slr. *IEEE Transactions on Medical Imaging*, 30(5):1042–1054, 2011.

[82] S G Lingala and M Jacob. Blind Compressive Sensing Dynamic MRI. *Medical Imaging, IEEE Transactions on*, 32(6):1132–1145, 2013.

[83] D Kim, H A Dyvorne, R Otazo, L Feng, D K Sodickson, and V S Lee. Accelerated phase-contrast cine MRI using k-t SPARSE-SENSE. *Magnetic Resonance in Medicine*, 67(4):1054–1064, 2012.

[84] L Feng, R Grimm, K T Block, H Chandarana, S Kim, J Xu, L Axel, D K Sodickson, and R Otazo. Golden-angle radial sparse parallel MRI: Combination of compressed sensing, parallel imaging, and golden-angle radial sampling for fast and flexible dynamic volumetric MRI. *Magnetic Resonance in Medicine*, 2013. doi: 10.1002/mrm.24980.

[85] M Usman, D Atkinson, F Odille, C Kolbitsch, G Vaillant, T Schaeffter, P G Batchelor, and C Prieto. Motion corrected compressed sensing for free-breathing dynamic cardiac MRI. *Magnetic Resonance in Medicine*, 70(2):504–516, 2013.

[86] M Doneva, C Stehning, K Nehrke, and P Börnert. Improving Scan Efficiency of Respiratory Gated Imaging Using Compressed Sensing with 3D Cartesian Golden Angle Sampling. In *Proceedings of the 19th Annual Meeting of the ISMRM*, page 624, 2011.

[87] M S Asif, L Hamilton, M Brummer, and J Romberg. Motion-adaptive spatio-temporal regularization for accelerated dynamic MRI. *Magnetic Resonance in Medicine*, 70(3):800–812, 2013.

[88] X Chen, M Salerno, P F Antkowiak, and F H Epstein. Motion-guided temporally-constrained compressed sensing for dynamic MRI. In *Proceedings of the 20th Annual Meeting of the ISMRM*, page 1230, 2012.

[89] X Chen, M Salerno, Y Yang, and F H Epstein. Motion-compensated compressed sensing for dynamic contrast-enhanced MRI using regional spatiotemporal sparsity and region tracking: Block low-rank sparsity with motion-guidance (BLOSM). *Magnetic Resonance in Medicine*, 2013. doi: 10.1002/mrm.25018.

[90] C Prieto, M Usman, J M Wild, S Kozerke, P G Batchelor, and T Schaeffter. Group sparse reconstruction using intensity-based clustering. *Magnetic Resonance in Medicine*, 69(4):1169–1179, 2013.

[91] M Usman, C Prieto, T Schaeffter, and P G Batchelor. k-t group sparse: A method for accelerating dynamic MRI. *Magnetic Resonance in Medicine*, 66(4):1163–1176, 2011.

[92] A Majumdar and RK Ward. Joint reconstruction of multiecho MR images using correlated sparsity. *Magnetic Resonance Imaging*, 29(7):899 – 906, 2011.

[93] G M Bydder and I R Young. MR imaging. Clinical use of the inversion recovery sequence. *Journal of Computer Assisted Tomography*, 9:659–675, 1985.

[94] A Haase, J Frahm, W Haenicke, and D Matthaei. 1H NMR chemical shift selective (CHESS) imaging. *Physics in Medicine and Biology*, 30:341–344, 1985.

[95] W T Dixon. Simple proton spectroscopy imaging. *Radiology*, 153:189–194, 1983.

[96] H Yu, S B Reeder, C A McKenzie, A C S Brau, and A Shimakawa. Single acquisition water-fat separation: feasibility study for dynamic imaging. *Magnetic Resonance in Medicine*, 55:413–422, 2006.

[97] H Eggers, B Brendel, A Duijndam, and G Herigault. Dual-echo Dixon imaging with flexible choice of echo times. *Magnetic Resonance in Medicine*, 65:96–107, 2011.

[98] J Berglund, H Ahlström, L Johansson, and J Kullberg. Two-point dixon method with flexible echo times. *Magnetic Resonance in Medicine*, 65:994–1004, 2011.

[99] G H Glover. Multipoint Dixon technique for water and fat proton and susceptibility imaging. *Journal of Magnetic Resonance Imaging*, 1:521–530, 1991.

[100] Q S Xiang and L An. Water-fat imaging with direct phase encoding. *Journal of Magnetic Resonance Imaging*, 7:1002–1015, 1997.

[101] S B Reeder, Z Wen, H Yu, A R Pineda, G E Gold, M Markl, and N J Pelc. Multicoil Dixon chemical species separation with an iterative least-squares estimation method. *Magnetic Resonance in Medicine*, 51:35–45, 2004.

[102] D Dunbar and G Humphreys. A spatial data structure for fast Poisson-disk sample generation. *Proceedings of SIGGRAPH*, pages 503–508, 2006.

[103] A Lagae and P Dutré. A Comparison of Methods for Generating Poisson Disk Distributions. *Computer graphics*, 27:114–129, 2008.

[104] M Fuderer. The information content of MR images. *IEEE Transactions on Information Theory*, 7:368–380, 1998.

[105] L Axel and L Dougherty. Heart wall motion: improved method of spatial modulation of magnetization for MR imaging. *Radiology*, 172:349–350, 1989.

[106] N Gdaniec, H Eggers, P Börnert, M Doneva, and A Mertins. Robust abdominal imaging with incomplete breath-holds. *Magnetic Resonance in Medicine*, 2013. doi: 10.1002/mrm.24829.

[107] J H Maki, T L Chenevert, and M R Prince. The effects of incomplete breath-holding on 3D MR image quality. *Journal of Magnetic Resonance Imaging*, 7:1132–1139, 1997.

[108] D A Feinberg, N M Rofsky, and G Johnson. Multiple breath-hold averaging (MBA) method for increased SNR in abdominal MRI. *Magnetic Resonance in Medicine*, 34(6):905–909, 1995.

[109] R M Azevedo, R O P Campos, M Ramalho, V Herédia, B M Dale, and R C Semelka. Free-breathing 3D T1-weighted gradient-echo sequence with radial data sampling in abdominal MRI: preliminary observations. *American Journal of Roentgenology*, 197(3):650–657, 2011.

[110] S S Vasanawala, Y Iwadate, D G Church, R J Herfkens, and A C S Brau. Navigated abdominal T1-w MRI permits free-breathing image acquisition with less motion artifacts. *Pediatric Radiology*, 40(3):340–344, 2010.

[111] V M Runge, J A Clanton, C L Partain, and A E James. Respiratory gating in magnetic resonance imaging at 0.5 T. *Radiology*, 151:521–523, 1984.

[112] J Pauly, D Nishimura, and A Macovski. A k-space analysis of small-tip-angle excitation. *Journal of Magnetic Resonance Imaging*, 81:43–56, 1989.

[113] K Nehrke, P Börnert, J Groen, J Smink, and J C Böck. On the performance and accuracy of 2D navigator pulses. *Magnetic Resonance in Medicine*, 178:1173–1181, 1999.

[114] A C S Brau and J H Brittain. Generalized self-navigated motion detection technique: Preliminary investigation in abdominal imaging. *Magnetic Resonance in Medicine*, 55:263–270, 2006.

[115] M S Davenport, B L Viglianti, M M Al-Hawary, E M Caoili, R K Kaza, P S C Liu, K E Chenevert, and H K Hussain. Comparison of Acute Transient Dyspnea after Intravenous Administration of Gadoxetate Disodium and Gedobenate Dimeglumine: Effect on Arterial Phase Image Quality. *Radiology*, 266(2):452–461, 2013.

[116] R Winkelmann, P Börnert, J de Becker, R Hoogeveen, P Mazurkewitz, and O Dössel. Dual-contrast single breath-hold 3D abdominal MR imaging. *Magma*, 19(6):297–304, 2006.

[117] M Henningsson, G Mens, P Koken, J Smink, and R M Botnar. A new framework for interleaved scanning in cardiovascular MR: Application to image-based respiratory motion correction in coronary MR angiography. *Magnetic Resonance in Medicine*, 2014. doi: 10.1002/mrm.25149.

[118] P Peterson and Sven Mansson. Fat Quantification Using Multiecho Sequences with Bipolar Gradients: Investigatin of Accuracy and Noise Performance. *Magnetic Resonance in Medicine*, 71:219–229, 2014.

[119] D Hernando, C D G Hines, H Yu, and S B Reeder. Addressing Phase Errors in Fat-Water Imaging Using a Mixed Magnitude/Complex Fitting Method. *Magnetic Resonance in Medicine*, 67:638–644, 2012.

[120] S D Sharma, H H Hu, and K S Nayak. Accelerated T2*-Compensated Fat Fraction Quantification Using a Joint Parallel Imaging and Compressed Sensing Framework. *Journal of Magnetic Resonance Imaging*, 38:1267–1275, 2013.

[121] K G Hollingsworth, D M Higgins, M McCallum, L Ward, A Coombs, and V Straub. Investigating the Quantitative Fidelity of Prospectively Undersampled Chemical Shift Imaging in Muscular Dystrophy with Compressed Sensing and Parallel Imaging Reconstruction. *Magnetic Resonance in Medicine*, 2013. doi: 10.1002/mrm.25072.

[122] R Otazo, C Bilen, Y Wang, L Axwel, and D K Sodickson. Accelerated Dynamic MRI Using Multicoil Low-Rank Matrix Completion. In *In Proceedings of the 20th Annual meeting of the ISMRM*, page 4248, 2012.

List of publications

Peer-reviewed paper

- **N Gdaniec**, H Eggers, P Börnert, M Doneva, A Mertins. Robust abdominal imaging with incomplete breath-holds. Magnetic Resonance in Medicine, 2013 Jul 1. doi: 10.1002/mrm.24829.

Oral presentations on conferences

- **N Gdaniec**, H Eggers, P Börnert, M Doneva, A Mertins. Novel Sampling Strategy for Abdominal Imaging with Incomplete Breathholds. 20th Meeting of ISMRM, Melbourne, Book of Abstracts 600 (2012). *ISMRM Magna Cum Laude Merit Award*
- **N Gdaniec**, P Börnert, H Eggers, M Doneva, A Mertins. Towards Clinical Robustness in Abdominal Water-Fat Imaging. 29th Annual Scientific Meeting of ESMRMB, Lisbon/PT, Book of Abstracts 194 (2012).
- **N Gdaniec**, H Eggers, P Börnert, M Doneva, A Mertins. MR imaging of the abdomen: How to prevent respiratory motion artifacts. 58. Jahrestagung der Deutschen Gesellschaft für Medizinische Informatik, Biometrie und Epidemiologie e.V. (GMDS), Book of abstracts 157 (2013)
- **N Gdaniec**, A J Wiethoff, Q Yuan, P Börnert, H Eggers, D Pinho, I Pedrosa, A Mertins. Towards Robust Breath-held 3D Abdominal DCE Imaging. 22th Meeting of ISMRM, Milan, Book of Abstracts 329 (2014)

Poster presentations on conferences

- **N Gdaniec**, T Nielsen, P Börnert, H Eggers, M Doneva, A Mertins. Robust Resolution-adapted 3D Abdominal Breath-hold Water-Fat Imaging with Self-termination. ISMRM Data Sampling & Image Reconstruction workshop, Sedona (2013). *1st price Poster award*

- **N Gdaniec**, P Koken, P Börnert, C Stehning, H Eggers, M Doneva, A Mertins. Robust Dual-Contrast 3D Abdominal Imaging Within a Single Breath-Hold. 21th Meeting of ISMRM, Salt Lake City, Book of Abstracts 3714 (2013).

- **N Gdaniec**, T Nielsen, P Börnert, H Eggers, M Doneva, A Mertins. Towards Clinical Robustness in 3D Abdominal Water/Fat Imaging. 21th Meeting of ISMRM, Salt Lake City, Book of Abstracts 4278 (2013).

- **N Gdaniec**, A J Wiethoff, Q Yuan, P Börnert, H Eggers, D Pinho, I Pedrosa, A Mertins. Joint Reconstruction of DCE Abdominal Images. 22th Meeting of ISMRM, Milan, Book of Abstracts 1546 (2014)

Patent fillings

- **N Gdaniec**, H Eggers. Magnetic resonance image reconstruction method with respiratory mot detection during sampling of central and peripheral k- space areas, 2013, WO Patent App. PCT/IB2013/051,449.

- **N Gdaniec**, P Börnert, M Doneva, I Pedrosa. Method of Improved Multiple-Phase Dynamic Contrast-Enhanced Magnetic Resonance Imaging, not available online yet